TUDelft

Delft University of Technology

Shearography non-destructive testing and defect characterisation of thick composite structures

Tao, N.

DOI
10.4233/uuid:4d4a1cfa-836f-415f-a255-84d49a4797a0

Publication date
2023

Document Version
Final published version

Citation (APA)
Tao, N. (2023). *Shearography non-destructive testing and defect characterisation of thick composite structures*. [Dissertation (TU Delft), Delft University of Technology]. https://doi.org/10.4233/uuid:4d4a1cfa-836f-415f-a255-84d49a4797a0

Important note
To cite this publication, please use the final published version (if applicable).
Please check the document version above.

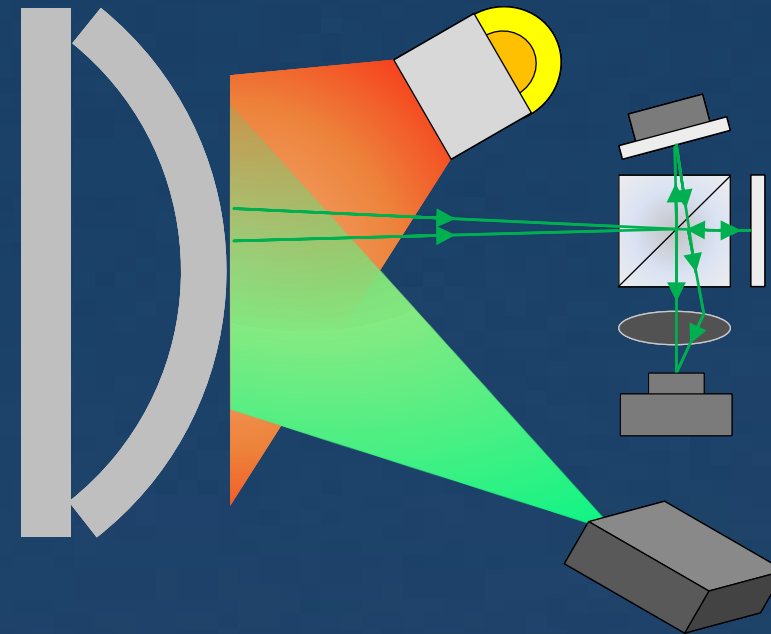# Shearography Non-Destructive Testing and Defect Characterisation of Thick Composite Structures

Nan Tao

TUDelft

Propositions

accompanying the dissertation

SHEAROGRAPHY NON-DESTRUCTIVE TESTING AND DEFECT CHARACTERISATION OF THICK COMPOSITE STRUCTURES

by

Nan TAO

1. A complete and reliable inspection of a real structure involves multiple NDT technologies, where high-resolution and high-sensitivity strain characterisation techniques should play a key role. (thesis)

2. Future inspection for safety-critical structures should require not only a validated NDT technique but also validated digital twins of the inspected structure and the NDT technique itself. (thesis)

3. Noise should not be overlooked in the research. It also implies and transfers valuable information. (thesis)

4. Breakthrough technical innovations for future NDT are more likely to occur when challenging engineering problems meet significant science advances.

5. It is easier to discard a composite structure than to maintain it.

6. While every researcher highlights the novelty and value of their work, most of these studies are meaningless to the society.

7. Nowadays pursuing a career in academia is like the pain of pursuing true love in life.

8. Loneliness is the requisite to achieve greatness in research.

9. Each PhD has their own path. PhDs in the Netherlands have to go through rain and darkness to achieve their success.

10. Just like playing badminton, it is unrealistic (physically impossible) to be everywhere and do everything simultaneously.

These propositions are regarded as opposable and defendable, and have been approved as such by the promotors prof. dr. ir. R. (Rinze) Benedictus and dr. ir. R.M. (Roger) Groves and copromotor dr. ir. A.G. (Andrei) Anisimov.

Stellingen

behorende bij het proefschrift

SHEAROGRAPHY NON-DESTRUCTIVE TESTING AND DEFECT CHARACTERISATION OF THICK COMPOSITE STRUCTURES

door

Nan TAO

1. Een volledige en betrouwbare inspectie van een echte structuur omvat meerdere NDT-technologieën, met hoge resolutie en zeer gevoelige technieken voor rek karakterisatie zouden een sleutelrol moeten spelen. (stelling)

2. Toekomstige inspectie van veiligheidskritische constructies zou niet alleen een gevalideerde NDT-techniek nodig moeten hebben, maar ook gevalideerde digitale tweelingen van de geïnspecteerde constructie en de NDT-techniek zelf. (stelling)

3. Ruis mag niet over het hoofd worden gezien in het onderzoek, het impliceert en bevat ook waardevolle informatie. (stelling)

4. Baanbrekende technische innovaties voor toekomstige NDT komen eerder voor wanneer uitdagende technische problemen gepaard gaan met significante wetenschappelijke vooruitgang.

5. Het is gemakkelijker om een composiet structuur weg te gooien dan om hem te onderhouden.

6. Tegenwoordig is het nastreven van een carrière in de academische wereld als de pijn van het najagen van ware liefde in het leven.

7. Hoewel elke onderzoeker de nieuwheid en waarde van zijn werk benadrukt, zijn de meeste van deze studies zinloos voor de samenleving.

8. Eenzaamheid is de vereiste om grootsheid in onderzoek te bereiken.

9. Elke promovendus heeft zijn eigen pad, promovendi in Nederland moeten door regen en duisternis gaan om hun succes te behalen.

10. Net als bij badminton is het onrealistisch (fysiek onmogelijk) om overal te zijn en alles tegelijk te doen.

Deze stellingen worden opponeerbaar en verdedigbaar geacht en zijn als zodanig goedgekeurd door de promotors prof. dr. ir. R. (Rinze) Benedictus and dr. ir. R.M. (Roger) Groves and copromotor dr. ir. A.G. (Andrei) Anisimov.

SHEAROGRAPHY NON-DESTRUCTIVE TESTING AND DEFECT CHARACTERISATION OF THICK COMPOSITE STRUCTURES

Shearography non-destructive testing and defect characterisation of thick composite structures

Dissertation

for the purpose of obtaining the degree of doctor
at Delft University of Technology,
by the authority of the Rector Magnificus Prof.dr.ir. T.H.J.J. van der Hagen,
chair of the Board for Doctorates,
to be defended publicly on
Wednesday 1 November 2023 at 15.00 o'clock

by

Nan TAO

Master of Science in Solid Mechanics, Southeast University, China
born in Anhui, China

This dissertation has been approved by the promotors.

Composition of the doctoral committee:

Rector Magnificus,	chairperson
Prof. dr. ir. R. Benedictus	Delft University of Technology, promotor
Dr. R.M. Groves	Delft University of Technology, promotor
Dr. A.G. Anisimov	Delft University of Technology, copromotor

Independent members:

Prof. dr. ir. K.M.B. Jansen	Delft University of Technology
Prof. dr. L.X. Yang	Oakland University, United States
Prof. dr. R.P. Tatam	Cranfield University, United Kingdom
Dr. C.L. Walters	Delft University of Technology
Prof. C.A. Dransfeld	Delft University of Technology, reserve member

In memory of my Grandpa
谨以此纪念我的外公

SUMMARY

T HICK composite materials, e.g., thickness of more than 50 mm, are increasingly being used across diverse industry sectors owing to their significant advantages of weight-savings, superior material properties and load-carrying capability. These materials tend to be adopted in safety-critical applications such as large primary or secondary load-bearing structures, where mechanical failures would result in serious consequences. However, various defects and damage may occur in thick composites that endanger structural integrity and safety severely. Hence to improve the maintenance, safety and reliability of these structures, it is crucial to develop inspection methods capable of defect detection and characterisation for composite structures of significant thickness. To date, the non-destructive testing and evaluation (NDT&E) of thick composite structures still remain an urgent challenge due to their material and structural complexity, significant thicknesses, and the presence of various manufacturing and in-service defects.

Shearography is a speckle interferometric optical method that is used to characterise surface strain components (i.e., displacement derivatives) under loading. It can reveal defects in an object by identifying defect-induced strain anomalies. Over the last two decades, shearography has gained considerable industrial acceptance as a powerful NDT technique for aerospace composite materials. However, most of its applications were limited to thin composites and shallow defects. There are still no comprehensive studies on shearography for thick composites and deep defects. This is because of a lack of under-standing of the interactions between loadings, materials, defects and the interpretation of shearograms. Therefore, the objective of this thesis is to develop shearography methods towards quantitative, predictable and safe inspection of thick composite structures, and also towards reliable detection and characterisation of deep defects.

The research presented in this thesis started with the investigation of defect detection capabilities and inspection limitations of shearography NDT for thick composites. Flat bottom holes were manufactured in a thick GFRP laminate to simulate major defects in thick composites. A full-scale, thermal-mechanical model of the test GFRP panel was developed by using equivalent thermal and mechanical properties to assist in the analysis. The established FEM model served as a predictive model to predict the behaviour of the thick composite and also to determine suitable loading parameters for the inspection. The thresholds for the defect-induced phase and deformation were investigated for reliable defect detection. The influence of mechanical boundary conditions on defect-induced deformation maps was studied by FEM. In addition, shearography NDT benchmarking with ultrasonic testing was also discussed for thick composite inspection.

Secondly, the development of shearography for NDT relies on the development of loading methods that can reveal defects. So the focus was placed towards developing novel spatially and temporally modulated thermal loading schemes for shearography to improve the detection and characterisation of deeply-buried defects in thick composites. Numerical and experimental studies have been performed to investigate the influence

of different heating scenarios on defect behaviour and defect detection to improve the understanding of NDT of thick composites. The heat flux distribution on the specimen surface was taken into consideration for thick composite inspection, a factor which is rarely reported in shearography NDT. For the spatially modulated heating (SMH), it was achieved by using a halogen lamp with a Fresnel lens. The shape of SMH was modified by adjusting the illumination setup with the Fresnel lens and heating at an angle. The influence of various reference states on shearography NDT of deep defects was studied. For temporally modulated heating, controlled surface temperature (CST) heating method was developed and realised based on the analytical solution of the constant surface temperature heating case. The proposed CST heating maximises heating energy input with a controlled and stable maximum surface temperature for safe shearography inspection. The results also provided insight for implementing an efficient inspection in terms of the inspection duration and the number of datasets.

Lastly, an experimental study was done for performance validation of shearography NDT on full-scale structures and for realistic defects in the in-service environment, specifically on-site inspection of a large-scale composite ship hull section that had been subjected to multiple impacts. Both thermal and mechanical loadings were evaluated for shearography NDT. A preliminary study of a representative sandwich panel with similar impact damage was also performed, providing valuable guidance regarding suitable experimental parameters including heating time and shearing distance for the on-site inspection, which are important parameters for successful shearography inspection.

In conclusion, this thesis has proposed and developed FEM-assisted shearography with spatially and temporally modulated thermal loading schemes, advancing this shearography method towards a quantitative, predictable and safe inspection technique for composite structures of significant thickness. Numerical and experimental results indicate that defects with a diameter of 60 mm are detectable up to 25 mm in depth and defects with a diameter of 30 mm are detectable up to 20 mm in depth (with the developed shearography method). The presented synergy of modelling and challenging experimental work brings a new understanding to thick composite inspection.

SAMENVATTING

D IKKE composiet onderdelen, bijvoorbeeld met een dikte van meer dan 50 mm, worden in toenemende mate gebruikt in diverse industriële sectoren vanwege hun aanzienlijke voordelen op het gebied van gewichtsbesparing, superieure materiaaleigenschappen en draagvermogen. Deze materialen worden vaak gebruikt in veiligheid kritische toepassingen, zoals grote primaire of secundaire lastdragende constructies, waarbij mechanisch falen ernstige gevolgen kan hebben. Er kunnen echter verschillende defecten en schade optreden in dikke composieten die de structurele integriteit en veiligheid in gevaar brengen. Om het onderhoud, de veiligheid, en de betrouwbaarheid van deze constructies te verbeteren, is het daarom cruciaal om inspectiemethoden te ontwikkelen die defecten te kunnen detecteren en te karakteriseren voor composiet constructies met een deze diktes. Tot op heden blijft het niet-destructief testen en evalueren (NDT&E) van dikke composietconstructies een urgente uitdaging vanwege hun materiële en structurele complexiteit, aanzienlijke diktes, en de aanwezigheid van verschillende fabricage-en in-service defecten.

Shearografie is een spikkel interferentie optische methode die wordt gebruikt om oppervlakte-rek (dwz verplaatsingsderivaten) onder belasting te karakteriseren. Het kan defecten in een object aan het licht brengen door defect-geïnduceerde rekafwijkingen te identificeren. In de afgelopen twee decennia heeft shearografie aanzienlijke industriële acceptatie gekregen als een krachtige NDT-techniek voor composietmaterialen voor de ruimtevaart. De meeste toepassingen waren echter beperkt tot dunne composieten en ondiepe defecten. Er zijn nog steeds geen uitgebreide studies over shearografie voor dikke composieten en diepe defecten. Dit komt door een gebrek aan begrip van de interacties tussen belastingen, materialen, defecten en de interpretatie van shearogrammen. Daarom is het doel van dit proefschrift om shearografie-methoden te ontwikkelen voor kwantitatieve, voorspelbare en veilige inspectie van dikke composietstructuren, en ook voor betrouwbare detectie en karakterisering van diepe defecten.

Het onderzoek gepresenteerd in dit proefschrift is begonnen met het onderzoeken van defectdetectiemogelijkheden en inspectiebeperkingen van shearografie NDT voor dikke composieten. Platte bodemgaten zijn vervaardigd in een dik GFRP-laminaat om grote defecten in dikke composieten te simuleren. Een volledig thermisch-mechanisch model van het GFRP-testpaneel is ontwikkeld door equivalente thermische en mechanische eigenschappen te gebruiken om te helpen bij de analyse. Het gevestigde FEM-model diende als voorspellend model om het gedrag van de dikke composiet te voorspellen en ook om de geschikte belasting voor de inspectie te bepalen. De drempels voor de defect-geïnduceerde fase en vervorming zijn onderzocht voor betrouwbare defectdetectie. De invloed van mechanische randvoorwaarden op defect-geïnduceerde vervormingskaarten is bestudeerd doormiddel van FEM. Daarnaast is ook shearografie NDT-benchmarking met ultrasoon testen besproken voor inspectie van dikke composieten.

Ten tweede is de ontwikkeling van shearografie voor NDT afhankelijk van de ontwikke-

ling van belastings-methoden die defecten kunnen onthullen. Hiervoor is de focus gelegd op het ontwikkelen van nieuwe ruimtelijk en temporeel gemoduleerde verwarmingen voor shearografie om de detectie en karakterisering van diepe defecten in dikke composieten te verbeteren. Numerieke en experimentele studies zijn uitgevoerd om de invloed van verschillende verwarmingsscenario's op defectgedrag en defectdetectie te onderzoeken om het begrip van NDT van dikke composieten te verbeteren. Bij de inspectie van dikke composieten is rekening gehouden met de warmtefluxverdeling op het monsteroppervlak, een factor welke zelden wordt vermeld bij shearografie NDT. Voor de ruimtelijk gemoduleerde verwarming (SMH) is dit bereikt door het gebruik van een halogeenlamp met een Fresnel-lens. De vorm van SMH is gewijzigd door de verlichtingsopstelling aan te passen met de Fresnel-lens om het materiaal onder een hoek te verwarmen. De invloed van verschillende referentietoestanden op shearografie NDT van diepe defecten is bestudeerd. Voor tijdelijk gemoduleerde verwarming is een verwarmingsmethode met gecontroleerde oppervlaktetemperatuur (CST) ontwikkeld en gerealiseerd op basis van de analytische oplossing van het scenario met constante oppervlakte verwarming. De voorgestelde CST-verwarming maximaliseert de invoer van verwarmingsenergie met een gecontroleerde en stabiele maximale oppervlaktetemperatuur voor veilige shearografie-inspectie. De resultaten geven inzicht voor het uitvoeren van een efficiënte inspectie wat betreft de inspectieduur en het aantal datasets.

Ten slotte is een experimenteel onderzoek uitgevoerd voor prestatievalidatie van shearografie NDT op constructies op ware schaal en voor realistische defecten in de in-service-omgeving. Voor specifieke inspectie ter plaatse van een composiet scheeps-rompgedeelte, welke is onderworpen aan meerdere inslagen, zijn zowel thermische als mechanische belastingen geëvalueerd voor shearografie NDT. Er is ook een voorstudie uitgevoerd van een representatief sandwichpaneel met vergelijkbare impactschade, wat waardevolle richtlijnen opleverde met betrekking tot geschikte experimentele parameters, waaronder verwarmingstijd en afschuifafstand voor inspectie ter plaatse, welke belangrijke parameters zijn voor succesvolle shearografie-inspectie.

Concluderend, dit proefschrift heeft FEM-geassisteerde shearografie met ruimtelijk en temporeel gemoduleerde verwarmingen, voorgesteld en ontwikkeld. Deze shearografie-methode is ontwikkeld tot een kwantitatieve, voorspelbare en veilige inspectietechniek voor composietstructuren met een aanzienlijke dikte. Numerieke en experimentele resultaten geven aan dat defecten met een diameter van 60 mm detecteerbaar zijn tot een diepte van 25 mm en defecten met een diameter van 30 mm detecteerbaar zijn tot een diepte van 20 mm (met de ontwikkelde shearografiemethode). De gepresenteerde synergie van modellering en uitdagend experimenteel werk brengt een nieuw inzicht in de inspectie van dikke composieten.

CONTENTS

LIST OF FIGURES

LIST OF TABLES

1

INTRODUCTION

1.1. THICK COMPOSITE MATERIALS

During the last decades, thick composite materials [1–3], represented by fibre reinforced laminates and sandwich structures, have found increasing applications in a diverse range of areas. In the marine sector, glass fibre reinforced composites (GFRP) are finding widespread applications in large-scale structures including ship superstructures, decks, and hulls [1, 4, 5]. Sandwich composites made from glass-fibre laminate skins with polyvinyl chloride (PVC)-foam core are commonly used for the construction of large hull structures. For example in the marine RAMSSES project [6], a real-scale full-composite hull section (6 m in height and 2.5 m in width) was manufactured from fibre reinforced solid laminates and sandwich structures (Figure 1.1(a)). The thickness of the hull varies in the range 50-300 mm. In the aerospace industry, carbon fibre reinforced composites (CFRP) have been applied to wings and fuselages [7–9]. For instance in the Airbus A380 (Figure 1.1(b)), the thickness of the composite components at the wing root joint could be up to 45 mm [10]. In wind energy (Figure 1.1(c)), glass fibre and carbon fibre reinforced composites are used in blades and foundations of offshore wind turbines [8, 11]. A prototype offshore wind turbine blade (100 meters long) made from fibre reinforced composites can have a cross-section up to 76 mm thick [3]. As for civil engineering (Figure 1.1(d)), CFRP and GFRP are commonly applied to reinforcements, load-bearing components, and pultruded profiles [12–15]. The entire bridge structure including support beam and deck can be fabricated using composites, allowing the bridge to be installed quickly and easily.

| Marine | Aerospace | Wind energy | Civil engineering |

Hull section **(a)**   Wing root **(b)**   Blade section **(c)**   Deck section **(d)**
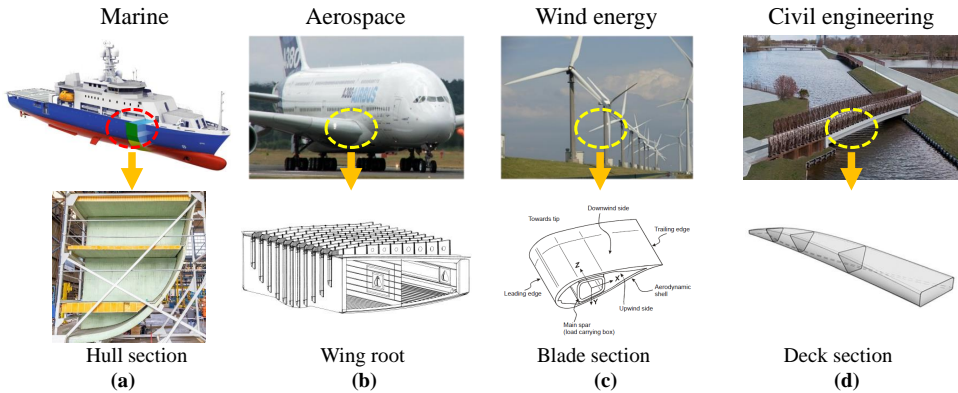
Figure 1.1: Thick composite applications in various industrial sectors [1, 7, 15].

The extensive use of thick composites can be attributed to their superior advantages of weight-savings, high stiffness and strength, corrosion and fatigue resistance and non-magnetic properties [1, 14]. Therefore, they offer a significant contribution to reducing fuel consumption and greenhouse gas emissions. Nevertheless, various defects including delaminations, fibre breakage and impact damage may exist in thick composites due to material complexity [8, 9, 16]. The presence of these defects may degrade the material properties and structural integrity severely [1, 8, 9]. Nowadays thick composite materials tend to be used in safety-critical applications such as large primary or secondary load-bearing structures, where a structural failure may cause catastrophic consequences [2, 8]. Hence the availability of inspection tools for thick composite materials is urgent for

both informing the maintenance and repair processes and for further advancing thick composite structure performance. So far, thick composite inspection remains an urgent challenge in literature and in industrial applications [8, 9], which in fact, is the main focus of this thesis.

1.2. Defects and damage in thick composites

Although successful applications of thick composites are extensive, nevertheless due to material and structural complexity, numerous types of defects and damage can occur in thick composites both during manufacturing and in service. These include delaminations and debonds (Figures 1.2(a) and 1.2(c)), fibre breakage (Figures 1.2(b) and 1.2(d)), core fracture (Figure 1.2(e)), impact damage, matrix cracking, voids and porosity, local resin content variation and fluid ingression [1, 17].

During the manufacturing process, it is often difficult to achieve a uniform cross-sectional curing profile in thick composite structures, resulting in regions of under-curing and over-curing of the polymer matrix [8, 16]. Residual stresses that arise from resin shrinkage and uneven curing can lead to delaminations, fibre-matrix debonding, fibre waviness, and matrix cracking in thick composites, which may cause significant degradation of strength in structural applications [18]. In other cases, air or moisture entrapped during curing and the use of defective or expired raw materials can also result in defects such as voids, porosity, and delaminations [1, 8, 17].

In-service, structures of thick composites are prone to different kinds of loading incidents, such as impact events, cyclic loads and other service loads [5]. These loading incidents can lead to a large number of defects. For example impact events can cause various types of damage such as kissing bonds, delaminations and matrix cracking which may be barely visible from the impact surface [8, 19]. Environmental factors, e.g., ultraviolet radiation, water absorption, erosion and lightning strikes, can also be significant in the formation of defects during service. As an example, epoxies are usually sensitive to ultraviolet light, water ingression and ice formation, and the strength of the resins will degrade severely if exposed to these environments for any significant period of time [1, 4].
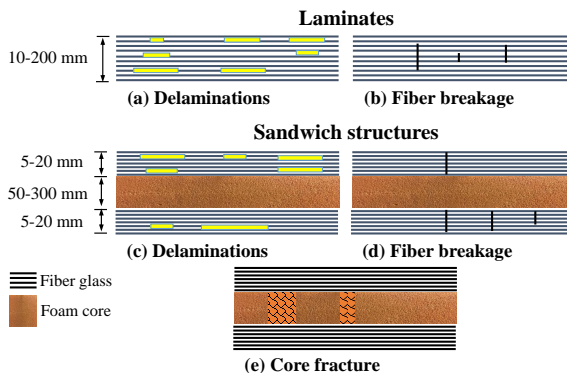
Figure 1.2: Illustration of common defects in thick composites (Source: Damen). (a)-(b): Defects occurring in laminates. (c)-(e): Defects occurring in sandwich structures

1

All these defects and damage types may exist in thick composite structures and can affect the material properties and structural integrity severely. Besides, they may arise at various locations and occur throughout the manufacturing process and the in-service life. Hence, it is important to advance non-destructive testing (NDT) and characterisation towards composite structures of significant thickness for improving structural safety and reliability.

1.3. INSPECTION CHALLENGES AND OPPORTUNITIES

THE increasing use of thick composites in primary and secondary loading-bearing structures across diverse industrial sectors, on the one hand, is of great significance in reducing operating costs and making a reduced impact on the environment [1, 7]. As an example, fibre-reinforced composites have the possibility to reduce weight up to 50% compared to the use of steel, and to decrease 15% fuel consumption and costs [20]. On the other hand, it poses a list of challenges to defect defection and characterisation due to the complexity [1, 2, 9, 16]:

1. These materials often consist of glass fibre and polymer matrix that are highly heterogeneous, anisotropic and non-conductive. Hence they are highly attenuative to some established NDT signals (e.g. ultrasonic signals). In thick structures such as thick fibre-reinforced laminates, deeply buried defects are usually difficult to detect due to high stiffness and attenuation.

2. The test structures (e.g., hulls or decks in the marine sector) are often of large lateral dimensions. Therefore they pose the requirement of high inspection productivity that may make an NDT method impractical or unreliable.

3. During the process of an inspection, the selection of parameters of an inspection system often highly depends on the experience or practice of a specific person, which may affect the accuracy and efficiency of the inspection.

4. The presence of a surface coating of the test structure and/or the existence of moisture and salt ions in the marine environment may affect the results of measurements.

5. There is an increasing need for performance validation of NDT techniques on large-scale engineering structures in the in-service environment (e.g., in a shipyard).

So far, the NDT defect detection capabilities and inspection limitations for thick composites have not been fully characterised. To improve the acceptance of these materials for usage in primary and secondary load-bearing structures and thus to fulfill their full market potential, there is an increasing need for a comprehensive understanding of the NDT of thick composites.

1.4. OPZUID PROJECT

THE research in this study is part of the Operationeel Programma Zuid-Nederland (OPZuid) as part of the Dutch Composite Maintenance Centre (DCMC, https://

`www.composite-maintenance.com/`), supported by the Europees Fonds voor Regionale Ontwikkeling (EFRO) and the North Brabant province of the Netherlands. One of the central objectives of the programme is to detect and monitor relevant damage and defects in large maritime infrastructural thick-composite constructions. Different NDT techniques are being developed to advance thick composite inspection. The project partners include the Aerospace NDT research group of TU Delft, Damen, TiaT, and Dutch Terahertz Inspection Services. This PhD research will focus on optical metrology for in-service inspection, where all materials, geometries, and scales are driven by the actual industrial needs, e.g., specifically by Damen shipyards.

1.5. RESEARCH GOAL AND SCOPE

THE goal of this research is to develop novel optical metrology instrumentation for the inspection of thick composite structures (50-60 mm thick and more) and for pushing reliable detection and characterisation towards deep defects. From the industrial needs point of view, the interest lies in detecting and characterising not only shallow but more importantly deeply buried defects in thick composite structures. This research will also increase the Technology Readiness Level (TRL), e.g., by bringing the developed technique out of the laboratory in the nearest future. Besides, it will advance the acquisition of such knowledge for a comprehensive understanding of the NDT of thick composites that can be crucial for providing confidence for the acceptance of these structures for usage in primary and secondary loading applications.

In literature, there is no agreement on thickness of what can be called a thick composite [21]. Thick or thick-section composites can be defined as ones where the effect of geometry (thickness-to-span ratio), material constituents (matrix/fibre stiffness and strength properties), lamination scheme, processing, and service loading exhibit three-dimensional states of stress [17]. Here the research focus is on the inspection of composites with a thickness of 50-60 mm and more, which are common in the marine sector.

1.6. THESIS OUTLINE

THE thesis consists of eight chapters. Chapter 2 presents an overview of non-destructive testing methods for inspection of large, thick composite structures. The specific NDT methods addressed in this section include optical NDT methods, ultrasonics, vibration analysis, thermography and X-ray, which leads to an assessment for the selection of the NDT method for this study. The principles of shearography including various phase-shifting techniques and loading methods are presented, which serve as the basis of shearography NDT developed in this research.

Chapter 3 defines the main research questions and the sub-research questions. The methodology adopted to investigate these questions is also explored in this chapter.

Chapter 4 addresses the research question of defect detection capabilities and inspection limitations in thick composites with shearography. A numerical-experimental study is conducted with a 51 mm thick GFRP laminate. Flat bottom holes of different diameters and remaining thicknesses are manufactured in the test GFRP panel to reliably simulate major defects in the thick composite. A thermal-mechanical model is estab-

1

lished by computing equivalent thermal and mechanical properties and is evaluated by experiments. The established model can serve as a predictive model to guide and assist shearography inspection. It can be noted that to achieve the objective of defect detection in thick composites, quantitative surface strain characterisation from the buried defects is needed to compare with numerical results and to guide the design of thermal loading schemes for thick composite inspection. The numerical and experimental results of the defect detection capability of shearography in the thick GFRP laminate are presented and discussed. This chapter also opens new possibilities with modulated thermal excitations that will be explored in the following chapters.

Chapters 5 and 6 propose novel spatially and temporally modulated thermal loading schemes for shearography NDT to improve defect detection and characterisation in thick composites. The spatially modulated heating is developed by using a halogen lamp with a Fresnel lens. The temporally modulated heating is developed based on the analytical solution of the constant surface temperature case for the control and selection of the maximum surface temperature of the test object during shearography inspection. Moreover, by combining shearography NDT with the finite element method (FEM), the influence of various heating scenarios on defect behaviour and defect characterisation is investigated to improve the understanding of thick composite inspection with shearography.

To validate the performance of shearography NDT on full-scale structures and for realistic defects and damage, Chapter 7 presents an experimental study about shearography NDT of a large-scale full-composite ship hull section in a shipyard environment. The knowledge and findings gained with the studies from the previous chapters are incorporated. The test structure has been subjected to multiple impact tests in the RAMSSES project before the inspection. Different loading scenarios including thermal loadings as well as a mechanical loading were performed for shearography NDT. A comparison between thermal loading and mechanical loading on thick composite inspection with shearography is presented to evaluate their corresponding efficacies in defect detection.

Chapter 8 presents the main conclusions of this thesis and gives recommendations for future work on thick composite inspection.

REFERENCES

[1] E. Greene, *Inspection techniques for marine composite construction and NDE,* Report No SSC-463, United States Ship Structure Committee, Washington, DC (2012).

[2] W. R. Broughton, *Thick composites,* (Teddington, 2001) pp. 1–31.

[3] Y. Hou, L. Li, and J. H. Koo, *Thick-section epoxy composites,* in *Composite Materials*, edited by M. A. Chowdhury, J. L. R. Armenta, M. M. Rahman, A. Asiri, and Inamuddin (IntechOpen, Rijeka, 2021) Chap. 6, pp. 1–16.

[4] E. Greene, *Marine composites, second edition,* (1999).

[5] P. Tran, A. Ghazlan, T. P. Nguyen, and R. Gravina, *Experimental and theoretical damage assessment in advanced marine composites,* in *Marine Composites: Design and Performance*, Woodhead Publishing Series in Composites Science and Engineering, edited by R. Pemberton, J. Summerscales, and J. Graham-Jones (Woodhead Publishing, 2019) pp. 55–84.

[6] S. Paboeuf, A. de Bruijn, F. Evegren, M. Krause, and M. Elenbaas, *A "fast track to approval" process for innovative maritime solutions,* in *Practical Design of Ships and Other Floating Structures,* edited by T. Okada, K. Suzuki, and Y. Kawamura (Springer Singapore, Singapore, 2021) pp. 51–63.

[7] R. M. Groves, *Inspection and monitoring of composite aircraft structures,* in *Comprehensive Composite Materials II,* edited by P. W. Beaumont and C. H. Zweben (Elsevier, Oxford, 2018) pp. 300–311.

[8] M. Ibrahim, *Nondestructive evaluation of thick-section composites and sandwich structures: A review,* Composites Part A: Applied Science and Manufacturing **64**, 36 (2014).

[9] W. Nsengiyumva, S. Zhong, J. Lin, Q. Zhang, J. Zhong, and Y. Huang, *Advances, limitations and prospects of nondestructive testing and evaluation of thick composites and sandwich structures: A state-of-the-art review,* Composite Structures **256**, 112951 (2021).

[10] P. Jerome, *Composite materials in the airbus A380-from history to future,* in *Beijing: Proceedings 13th International Conference on Composite Materials (ICCM-13)* (2001) pp. 1–10.

[11] P. Zhang, *Offshore wind turbines,* in *Marine Composites: Design and Performance,* Woodhead Publishing Series in Composites Science and Engineering, edited by R. Pemberton, J. Summerscales, and J. Graham-Jones (Woodhead Publishing, 2019) pp. 317–344.

[12] L. Van Den Einde, L. Zhao, and F. Seible, *Use of FRP composites in civil structural applications,* Construction and Building Materials **17**, 389 (2003).

[13] J. R. Correia, Y. Bai, and T. Keller, *A review of the fire behaviour of pultruded GFRP structural profiles for civil engineering applications,* Composite Structures **127**, 267 (2015).

[14] A. Biddah, *Structural reinforcement of bridge decks using pultruded GFRP grating,* Composite Structures **74**, 80 (2006).

[15] R. Blok, J. Smits, R. Gkaidatzis, and P. Teuffel, *Bio-based composite footbridge: Design, production and in situ monitoring,* Structural Engineering International **29**, 453 (2019).

[16] M. Ibrahim, *Nondestructive testing and structural health monitoring of marine composite structures,* in *Marine Applications of Advanced Fibre-Reinforced Composites,* Woodhead Publishing Series in Composites Science and Engineering, edited by J. Graham-Jones and J. Summerscales (Woodhead Publishing, 2016) pp. 147–183.

[17] CMH-17-3G, *Composite Materials Handbook, Volume 3 - Polymer Matrix Composites - Materials Usage, Design, and Analysis* (SAE International, 2012).

1

[18] G. Alleman, *The effects of different cure cycles on the mechanical performance of thick-walled composites,* Delft University of Technology (2018).

[19] C. Maierhofer, R. Krankenhagen, and M. Röllig, *Application of thermographic testing for the characterization of impact damage during and after impact load,* Composites Part B: Engineering **173**, 106899 (2019).

[20] P. A. Ochôa, H. den Ouden, M. Hagenbeek, N. Tao, A. G. Anisimov, and R. M. Groves, *Towards complete diagnosis of structural damage in a real-scale full-composite ship hull section subjected to high-energy impacts by acoustic emission monitoring and laser shearography inspection,* Under review (2023).

[21] A. Djabali, L. Toubal, R. Zitoune, and S. Rechak, *Fatigue damage evolution in thick composite laminates: Combination of x-ray tomography, acoustic emission and digital image correlation,* Composites Science and Technology **183**, 107815 (2019).

2

LITERATURE REVIEW

A general definition of non-destructive testing (NDT) is 'an examination, test, or evaluation performed on any type of test object without changing or altering that object in any way, in order to determine the absence or presence of conditions or discontinuities that may have an effect on the usefulness or serviceability of that object' [1]. Normally, NDT techniques rely on a variety of physical principles. These physical principles [2, 3] include ultrasonic waves, optical interference, acoustic response, thermal emission, electromagnetism and the penetration of high-energy radiation through material structures. Figure 2.1 illustrates a summary of common NDT techniques from the literature. Various kinds of NDT methods such as ultrasonics have been widely used for the inspection of thin composites in the aerospace industry. Nevertheless, for thick composites, which are commonly large structures used as primary or secondary load-bearing structures in the marine sector, the efficacy of the current NDT techniques has not been fully characterised.

This chapter starts with an overview of several NDT techniques that have been applied to thick composite inspection. Then the focus is placed on shearography non-destructive testing in addition to heat transfer, thereby providing the knowledge necessary to understand and reproduce the background of this research.
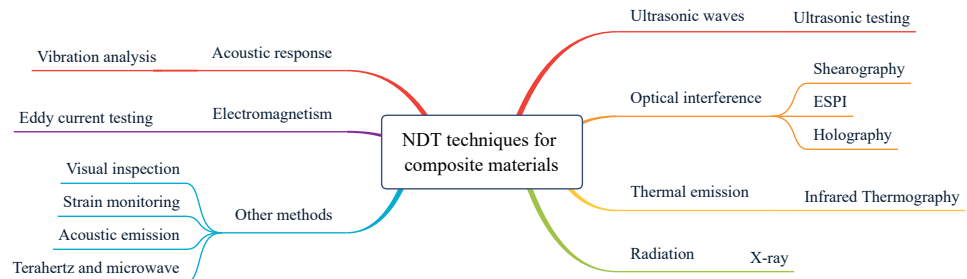
Figure 2.1: Common NDT techniques for composite materials

2.1. OVERVIEW OF NDT TECHNIQUES

THE section discusses several characteristics of five primary NDT techniques with regard to their applicability for thick composite inspection: ultrasonic testing, vibration analysis, thermography, X-ray and optical interferometric techniques. The characteristics of the five NDT techniques are summarized in Table 2.1.

Ultrasonic testing (UT, Figure 2.2(a)) is one of the most well-known NDT methods for composite materials in the aerospace industry [4]. It uses high-frequency ultrasound energy to detect composite structural anomalies such as cracks or delaminations [4, 5]. During the last decades, advanced ultrasonic testing methods including phased array ultrasound testing [5, 6], air-coupled ultrasonics [7–9], and laser-induced ultrasound [4] have been developed for defect detection. Although it has been widely used in industrial inspection for a long time, the attenuation, scattering and multiple reflections of ultrasound signals can become significant issues when inspecting thick composites, especially GFRP with fibre bundles of similar diameters to the wavelength of the ultrasonic waves. Ultrasonics may also have trouble performing an on-site inspection, e.g. in the shipyard environment [10]. For example, practical acoustic coupling issues with high surface

roughness are usually significant in marine composite inspection [11]. Besides, it can take a long time to scan an entire structure (e.g. ship hull) [10]. Therefore it is a challenge to apply it for inspecting thick composites.

Vibration analysis [12–14] and thermography [10, 15–20] have been widely used for the inspection of composite structures. They have their own disadvantages and limitations when inspecting thick composites. Vibration analysis includes low-frequency resonance and mechanical impedance techniques, which can reveal the presence of defects by detecting changes in dynamic properties (e.g. stiffness, natural frequency) of the composites. It suffers from detecting defects in structures with high stiffness, which means thick laminates or defects at significant depths are difficult or impossible to detect [21, 22]. For thermography (Figure 2.2(b)), it is difficult to heat evenly a large structure and to avoid rapid heat dissipation in thick composites. Therefore the ability to detect deeply buried defects in thick composites is limited. The characterisation limit of inspection depth with thermography in polymer-matrix composite laminates appears to be less than 5 mm [21, 22]. X-ray radiography and computed tomography [23–25] is an emerging NDT technique for defect detection in composite materials. One of the major challenges is a lack of ability to characterise damage and defects in the through-thickness direction. The danger associated with X-rays to humans can be a problem as well [21, 22]. Besides, X-ray is unsuitable for inspecting large-scale structures. So it is difficult to perform on-site inspections using X-ray radiography [10].

Among the various NDT methods in the existing literature, the optical interferometric techniques of holography, electronic speckle pattern interferometry (ESPI), and digital shearography [26–29] gain increasing attention for their significant advantages of being non-contact, full-field measurement and high-sensitivity to deformation change. Thus, these optical techniques are finding many applications for non-destructive inspection of composite structures [30–33]. Among the three optical techniques, digital shearography (Figure 2.2(c)) appears to be more practical [33, 34]. It requires a simple optical set-up and is insensitive to small rigid body motions, furthermore, it directly measures derivatives of surface deformation, which are closely related to surface strain components. This allows shearography to detect defects in structures by monitoring the anomalies of the surface strain field, which is usually easier than monitoring the anomalies of the surface displacement field as in holography or ESPI [33, 34]. Nevertheless, shearography, ESPI and holography suffer from a similar loss in detection capability to thermography, in that their effectiveness is normally rapidly reduced as the thickness of inspecting structures increases, making defects at significant depths incapable of being inspected or difficult to interpret [21, 22].

In short, the aforementioned NDT techniques, which were developed for aerospace composite materials, are not viable for large, thick marine composites [4]. Hence, an assessment that facilitates the selection of suitable NDT methods for thick marine composite structures is necessary.

2

Table 2.1: Summary of the characteristics of the various NDT techniques for composite materials, adopted and extended from [4, 21, 22, 35]

	Ultrasonic testing	Vibration analysis	Thermography	X-ray	Shearography
Inspection type	Contact (e.g., using coupling liquid or gel) and non-contact (e.g. air-coupled)	Contact (e.g., PZT sensor) and non-contact (e.g., laser vibrometer)	Non-contact	Non-contact	Non-contact
Physical principles	Ultrasound waves	Vibration response	Thermal emission	Penetration of X-ray radiation	Speckle interferometry
Measurement	Mechanical vibration	The shift in dynamic properties (e.g., modal properties)	Thermal radiation	The scattering or absorption of the radiation by the composite	Strain components
Loading	Acoustic waves	Mechanical vibration	Optically and non-optically heating	X-ray radiation	Thermal, vacuum, pressure, vibration
Experimental data	Amplitude and time of flight of ultrasonic waves	Vibration response - changes of modal parameters (e.g., modal curvatures, and mode shapes)	Sequences and thermal images	X-ray radiation images	Speckle interferograms
Data analysis	Qualitative and quantitative analysis through the ultrasonic amplitude – size and depth characterisation of defects	Qualitative analysis (quantitative analysis may be obtained with known reference state of the composite)	Qualitative and quantitative analysis through temperature distribution	Qualitative and quantitative analysis - size and depth characterisation of defects	Qualitative and quantitative analysis of phase (fringe) maps
Main parameters influencing measurements	• Material attenuation coefficient of the acoustic waves • Difference in acoustic impedance for multi-layered structures	• Structural stiffness and mass • Size of the composite • The depth of the flaw within the composites	• Material surface and bulk thermal properties (e.g., emissivity and conductivity)	• The scattering or absorption of the radiation by the composite under test	• Material properties, e.g., structural stiffness and conductivity • Surface roughness • Shearing direction and amount

Table 2.1 continued: Summary of the characteristics of the various NDT techniques for composite materials, adopted and extended from [4, 21, 22, 35]

	Ultrasonic testing	Vibration analysis	Thermography	X-ray	Shearography
Main advantages	• Precise measurement and determination of flaw depth • No harm to the environment or humans • Practical and easy to carry equipment	• A large area of the test object can be inspected • The defects or damage location and size can be identified by using advanced signal processing methods such as wavelet transforms	• Fast thermal control • Good estimation of damage dimension • Control adapted to all the geometries types	• Internal and surface flaws can be detected • Minimum surface preparation • Applicable to many types of materials	• Fast time of control • Control adapted to composites of all types of geometries
Main disadvantages	• Probes are changed for various measurements • Surface accessibility is generally required	• It generally provides overall structural health • Deeply buried flaws cannot be inspected if changes in vibration response cannot be detected	• The defect depth is not directly determined • The baseline data and signal processing techniques are required to determine the size and orientation of the damage	• Radiation is harmful to the human body • Data processing is difficult, and equipment is difficult to use by the general NDT practitioners • Slow process, and material must be accessible from both sides	• Practical difficulties in reproducible heating • Defect depth not directly evaluated unless advanced signal processing is applied • Long inspection time to detect deep defects
Limitations	• The geometry of the material and its ability to conduct sound waves are important • The coupling may be required • Superimposed flaws may be difficult to find (i.e., shadowing effect)	• It cannot establish the size of the damage if the reference state is unknown or advanced signal processing methods are not used • Heavy and large structures are difficult to inspect	• The thickness and thermal conductivity of the composite must be considered • The thermal gradient between the flaw and the composite is necessary	• Access to both sides of the composite is required • Images of composites may suffer from poor phase contrast and long acquisition times	• Large rigid-body movements and significant vibrations could cause speckles de-correlation • Coupling between laser power and field of view • Ambient lights and air flows

2

(a)   **(b)**   **(c)**
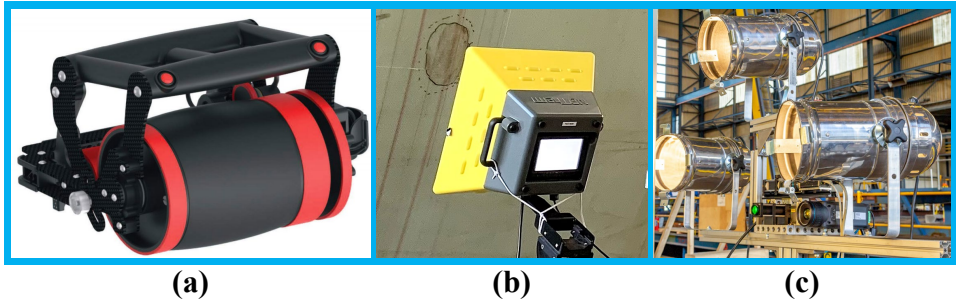
Figure 2.2: Instruments of common NDT techniques: (a) ultrasonic testing, (b) thermography and (c) shearography.

2.2. Assessment of NDT techniques for large, thick composite structures

Although main characteristics of the various NDT techniques have been summarised in Table 2.1, nevertheless, it may be difficult to draw conclusions about the selection of appropriate NDT techniques from it. For this reason, Table 2.2 has been made to clarify the differences between the five primary NDT techniques, so that a clear comparison can be made. The assessment of the five primary NDT techniques for large, thick marine composite structures can be from the following aspects [4, 21, 22, 35]:

- Robustness against environmental influences: e.g., vibrations, air flows

- Inspection type: non-contact or contact inspection

- Applicability in the marine environment: e.g., in a shipyard

- Inspection productivity

- The ability to detect critical defects: e.g., delaminations, fibre breakage and impact damage

- The ability to detect deep defects, e.g., 15-25 mm depth and more

- Safety: e.g., laser and radiation issues

- Configurations: inspection access from one side, two sides or all sides

- Surface requirements: e.g., ultrasonics usually require a relatively smooth surface for good surface coupling

- Portability

- Potential for automation (for large, thick composite inspection)

- Cost: varied depending on instruments

- The test structure may have surface coatings which may affect the selection of NDT methods

- Technology Readiness Level (TRL) of the technique

The comparison of the five techniques based on the above factors is summarised in Table 2.2. This part was also benefiting from the discussions with the experts from the Aerospace Structures and Materials (ASM) Department of the Faculty of Aerospace Engineering at TU Delft.

Robustness is one of the most important evaluation indexes of an NDT technique for practical industrial applications. It should be acknowledged that the comparison of robustness between different NDT techniques is difficult. Given that all five techniques already have commercial instruments available on the market, such as Sonatest Veo and Olympus Omniscan UT systems, FLIR infrared systems and automated shearography systems of Optrion. the robustness of these techniques is considered to be at a medium-high level.

The inspection type of an NDT technique is also an important evaluation index. Non-contact type may be a better choice in many applications. For ultrasonic testing of thick composites, contact using coupling liquid or gel is usually required as high ultrasound energy is needed. For vibration analysis, contact is also usually required. As for thermography, X-ray and shearography, they are non-contact techniques because of the nature of the optical methods [21, 22, 35].

Since the research of this thesis has a special focus on the marine sector where thick composite structures have extensive applications, the applicability of the NDT technique in the marine environment also needs to be taken into consideration (e.g., the availability for on-site inspection in shipyards or other harsh marine environments). Vibration analysis and shearography are considered to be at a medium-high level because of their advantages of simple setup and full-field measurement. Ultrasonics and thermography have trouble inspecting large ship hulls in the shipyards environment (e.g., ultrasonics has difficulties due to scanning and high surface roughness issues and thermography has difficulties in heating large-scale structures uniformly), so their applicability can be assumed at a medium level. X-ray is considered to be at a low level due to the complicated setup and the health risks of X-ray radiation [4, 21, 22, 35].

The inspection productivity is also a noteworthy aspect. The inspection of large marine structures requires high inspection productivity to make the total inspection time reasonable. Ultrasonic testing and X-ray technique need to scan the whole structure, the corresponding inspection productivity is at a low or medium level; while vibration analysis, thermography and shearography are global measurement techniques, their inspection productivity is relatively high [21, 22].

The ability to detect critical defects and deep defects is of great interest to both the industry/end users and the academic community in NDT&E. The comparison and evaluation of different NDT&E techniques for critical defects and deep defects were mainly referred to [4, 21, 22, 35].

Regarding the safety aspect, here it more refers to the safety concerns of humans (for clarification, the study of safe shearography inspection in Chapter 6 is on the safety of the structure). Ultrasonic testing, vibration analysis and thermography are considered to be

2

at a low-risk level as they are commonly used in labs. Shearography uses scattered laser light to illuminate the test object which is safe for operators due to the low intensity of the scattered laser light, it is with limited risk. While X-ray technique is considered to be at a high-risk level due to radiation issues [21, 22].

As for configuration, in common inspections in an in-service environment, access to both sides of a test structure is usually not available. Hence single-sided inspection seems to be preferred. In ultrasonic testing, depending on the use of pulse-echo or transmission mode, the configuration can be either single side or both sides. Vibration analysis and thermography can also be single side or both sides depending on applications [4, 35]. X-ray technique may require access to both sides or all sides of the part due to a computed tomography scan. As for shearography, it requires access to single side in most applications [4, 35].

The use of the NDT technique may need some surface requirements for inspection. As introduced in Section 2.1, ultrasonic testing usually requires a smooth surface for good surface coupling and it may have inspection problems with high roughness surfaces. For thermography, high emissivity coatings sometimes can be required [3, 11, 21, 22]. As for shearography, optical-rough surface is usually needed to produce reliable speckle inter-ferograms. Spraying removable white paint on the surface of the test object is commonly used to increase the scattered light for the shearography inspection. But it is also feasible to perform the inspection without spray paint depending on surface conditions [11, 36].

The portability and the potential for automation can be of interest when it comes to in-service inspections. The higher the portability and the automation of the NDT technique can be, the more convenient and faster the inspection will be. There are already portable devices for ultrasonic testing, vibration analysis, thermography and shearography on the market, the portability of these techniques is considered to be high. While for X-ray technique, it is at a low to medium level due to the danger associated with X-ray radiation. For automation, the automated scanning of a standing ship hull using ultrasonic testing is difficult due to the need for contact and the high surface roughness and high curvature of the hull. Vibration analysis, thermography and shearography are considered to have higher potential for automation than ultrasonic testing as these techniques can perform full-field measurements. While X-ray technique is supposed to be at a low to medium level due to the radiation issue.

Furthermore, the selected NDT technique needs to be a cost-effective one for thick composite inspection. The cost of each technique was evaluated according to [4, 35].

It can be noted that in some cases, the last two aspects of surface coatings of the test structure and the TRL of the technique in the bulleted list may play a role in the selection of appropriate NDT methods, however, they are considered to be less important for this research. So these two aspects are not included in Table 2.2.

This thesis aims to develop shearography methods for the inspection of thick composite structures for the advantages of non-contact inspection, good applicability in the marine environment, good inspection productivity and excellent ability to detect critical defects. The accomplishment of such an aim will also improve deep defect detection with shearography.

Table 2.2: Comparison of various NDT techniques for large, thick composite inspection

	Ultrasonic testing	Vibration analysis	Thermography	X-ray	Shearography
Robustness	Medium-High	Medium-High	Medium-High	Medium-High	Medium-High
Inspection type	Contact	Contact	Non-contact	Non-contact	Non-contact
Applicability in marine	Medium	Medium-High	Medium	Low	Medium-High
Inspection productivity	Low-Medium	Medium-High	Medium-High	Low-Medium	Medium-High
The ability for critical defects	Medium-High	Medium	Medium	Medium-High	High
The ability for deep defects	Low-Medium	Low-Medium	Low-Medium	Medium	Low-Medium
Safety	Low risk	Low risk	Low risk	High risk	Low-Medium risk
Configuration	Access to single side (pulse-echo) and both sides (transmission)	Access to single side and both sides	Access to single side (reflection) and both sides (transmission)	Requires access to both sides or all sides of the part	Single-sided inspection
Surface requirement for inspection	Requires smooth surface for good surface coupling	Not Required	Sometimes requires high emissivity coatings	Not required	Optical-rough surface (sometimes sprayed with white painting)
Portability	High	High	High	Low-Medium	High
Potential for automation	Medium	Medium-High	Medium-High	Low-Medium	Medium-High
Cost	Low-Medium $50k - $250k$	Low $\sim \$1.5k$	Low-Medium $10k - $250k$	High $\sim \$1000k$	Medium $\sim \$100k$

To have a clear idea about the required inspection productivity for large marine composite structures, a calculation was done to estimate the inspection time for real-scale marine ship (40 m long and 6 m tall). As shown in Table 2.3, the total inspection area (two sides of the ship) is about 408 m^2. In order to inspect the whole ship in 24-48 hours, the required inspection productivity needs to be 8.5-17 m^2/h. The productivity with our in-house built inspection system is 4-16 m^2/h depending on the field of view (FOV) of the shearography camera sensor. Moreover, for large shearography production systems, the inspection productivity can easily achieve 27-65 m^2/h (as a comparison, the typical productivity with ultrasonic C-scan is about 0.5-1.5 m^2/h) [37]. So shearography is well suited to the inspection of large marine composite structures.

Table 2.3: Required inspection productivity for large marine composite structures

Total inspection area		408 m^2	
Required inspection hours		24 h	48 h
Required inspection productivity		17 m^2/h	8.5 m^2/h
DS productivity		27-65 m^2/h	
UT productivity		0.5-1.5 m^2/h	
DS productivity	FOV - 1 × 1 m^2	4 m^2/h	
in our study	FOV - 2 × 2 m^2	16 m^2/h	

Note: the productivities with shearography (DS) and ultrasonic testing (UT) are listed for comparison.

2.3. DIGITAL SHEAROGRAPHY

DIGITAL shearography (DS) is an advanced speckle interferometric NDT method that can be used to characterise surface strain components under loading. This technique has been used for the qualitative inspection of delaminations, debonding, fibre breakage, impact damage and many other defects in thin composite materials (e.g., thickness of less than 10 mm) [32, 37–46]. It reveals defects in an object by looking for defect-induced deformation anomalies in the surface strain field. The surface strain field is obtained by comparing two deformation states of the test object. The key point of the shearography technique is to introduce image shearing, which can be achieved by using various shearing devices such as Michelson shearing interferometer, Wollaston prism, spatial light modulator, and diffractive optical elements [47–50]. Developments of digital shearography experimental system for NDT include quantitative multi-component shearography [47, 51, 52] and lock-in shearography [53–55]. More recently, 3D shape shearography has been developed that enables the characterisation of in- and out-of-plane surface strain components of curved and free-form objects [36, 56].

2.3.1. FUNDAMENTALS OF DIGITAL SHEAROGRAPHY

The Michelson shearing interferometer is the most common shearing device due to its simple set-up and easy adjustment of the shearing amount and shearing direction [47]. This section discusses the theory of shearography with the Michelson shearing interferometer as the shearing device [33, 47].

A schematic of a representative shearography system is shown in Figure 2.3. During

the shearography inspection, a laser beam is expanded with a beam expander to illuminate an optically rough surface (Figure 2.3(a)), creating a speckle pattern. By tilting the shearing mirror by a small angle, two images (identical but sheared) are generated (Figure 2.3(b)). In this way, the scattered light from two neighbouring positions on the surface of the object can be brought to meet in the image plane of a CCD camera, interfering with each other to form a speckle interferogram. The shearing device can control the direction and the amount of the shearing (e.g., δx in the x-direction in Figure 2.3(b)), thus enabling phase-shifting for obtaining the optical phase (ϕ) of the recorded speckle interferograms.

$$I = I_0 \left(1 + \gamma cos\phi\right) \tag{2.1}$$

where I_0 represents the background intensity, γ represents a term that indicates the fringe modulation, and ϕ represents a random relative phase between the two neighbouring points, separated by δx.

Defect detection by shearography relies on comparing two deformation states of the object. Two sets of phase-shifted interferograms (reference and signal sets of images in Figure 2.3(c)) are captured during measurement. The reference images can be captured before loading, during loading, or after loading, and the signal images are usually captured after loading. Computing the difference of the phases between the two states (ϕ' and ϕ) of deformation yields the phase difference ($\delta\phi$), which is also known as fringe pattern:

$$\delta\phi = \phi' - \phi \tag{2.2}$$

it can be noted that $\delta\phi$ represents the optical phase difference introduced by loading, which is proportional to the displacement gradient in the shearing direction. If the shearing direction is parallel to the x-direction and the shearing amount (δx) is small enough, the relative phase change is approximately represented by:

$$\delta\phi = \frac{2\pi}{\lambda} \left(l_x \frac{\partial u}{\partial x} + l_y \frac{\partial v}{\partial x} + l_z \frac{\partial w}{\partial x} \right) \delta x \tag{2.3}$$

Where λ is the laser wavelength, $l = \left(l_x, l_y, l_z\right)$ is the sensitivity vector which is defined as the bisector of the observation and illumination vectors, u, v, w represent the components of the displacement vector in the x, y, and z directions respectively.

If the observing and illuminating directions are arbitrary, then Eq. 2.3 contains contributions from all these three displacement derivative terms. Therefore three observation directions or three illumination directions are required to obtain all three displacement derivatives [47].

By making the observing and illuminating directions normal to the object surface, l_x and l_y in Eq. 2.3 are brought close to zero and the optical phase difference can be approximately represented by a strain component or an out-of-plane displacement derivative [33, 47, 57]:

$$\delta\phi_x = \frac{4\pi}{\lambda} \frac{\partial w}{\partial x} \delta x \tag{2.4}$$

Eq. 2.3 and Eq. 2.4 show that when considering an image rather than a single point, shearography can detect flaws by finding strain anomalies from the surface strain field.
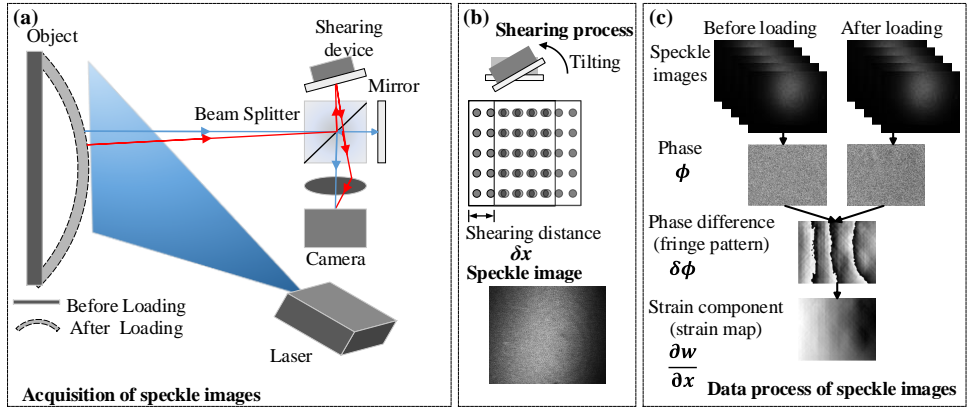
Figure 2.3: Diagram of shearography system for the out-of-plane displacement gradient (shearing along x-direction).

When the shearing direction is along the y-axis, the surface strain components in the y direction (e.g., $\partial w/\partial y$) can be obtained by replacing x with y in Eq. 2.3 and Eq. 2.4.

2.3.2. PHASE-SHIFTING METHODS FOR SHEAROGRAPHY

From the NDT point of view, a fringe pattern for defect detection can be simply produced by a direct subtraction method of reference and signal images, nevertheless, the obtained fringe pattern with this method has a relatively low phase measurement sensitivity (2π), which is not suitable for practical applications. To overcome this problem, phase-shifting methods were introduced [38]. Typically, the measurement sensitivity of digital shearography can be enhanced to at least $2\pi/10$ by employing the phase-shifting methods [38]. Phase-shifting digital shearography can be divided into two categories: temporal and spatial phase-shifting digital shearography [47, 58].

Temporal phase-shifting uses different phase-shifting amounts in a time series to obtain phase information [38]. The phase shifting can be induced by moving a mirror, a diffraction grating, or a polarization component [59]. For example in the shearography system based on the Michelson interferometer, the piezoelectric transducer (PZT) is often used for moving the mirror to introduce phase shifting because it is simple and straightforward. There are three phase-shifting algorithms commonly used: the three-step algorithm, the four-step algorithm and the five-step algorithm. Among these, the three-step algorithm is the fastest since only three images are required, while the four-step algorithm is the simplest and the five-step algorithm can compensate for errors introduced by miscalibration of the phase shifting [47, 60].

Spatial phase-shifting can determine the phase distribution from a single recording, thus it can realize dynamic or transient measurements. Spatial phase-shifting digital shearography can be mainly divided into spatial multichannel techniques and spatial carrier techniques [38, 58]. In spatial carrier techniques, Mach-Zehnder based, Michelson based, and double-aperture based systems are commonly used [38, 47]. The carrier frequency is introduced into the recorded intensity image. A Fourier transform then can be used to help isolate and calculate the phase distribution [38, 47].

2

The phase maps obtained using these phase-shifting methods are normally subjected to significant high-frequency noise and they are wrapped with a phase modulo 2π (known as wrapped phase maps or phase fringe patterns). Therefore phase filtering and phase unwrapping are needed to denoise and to obtain a continuous phase measurement [47]. The use of these phase-shifting methods in combination with proper phase filtering and phase unwrapping as well as shear distance calibration [36, 47] allows the quantitative characterisation of the defects (e.g., defect size and defect deformation) in the inspection.

In general, temporal phase-shifting digital shearography has high phase map quality and is suitable for static and quasi-static measurements, while spatial phase-shifting digital shearography is faster and more suitable for dynamic measurements with a decreased quality of phase map. Considering that the composite panels under investigation are thick ($\geq$ 50 mm) and the corresponding deformation is slow, temporal phase-shifting is selected for this research.

2.3.3. Loading methods for shearography

As mentioned in Section 2.3.1, shearography reveals defects in an object by comparing the phase difference of two deformation states, some form of loading or stressing is therefore required to be applied to the object being inspected. By applying a certain load to the composite materials, the defect region will deform along with the overall structural deformation. Due to the difference in mechanical and/or thermal properties between the defect region and the adjacent healthy region, surface deformation anomalies may appear which can be detected by shearography. In fact, it is vital to choose an appropriate means of loading to enable the success of shearography in defect detection. If the load is wisely applied, the anomalies in the test object may easily render themselves visible by a change in the surface strain field [26, 61].

Table 2.4 provides an overview of common loading methods for shearography NDT. They have been applied successfully in various types of thin composite structures (e.g., 2-5 mm in thickness). Nevertheless, common loading methods may have difficulties in shearography NDT of thick composites [26, 61]. For vacuum loading, a vacuum test chamber is required; the total enclosure is usually not practical for large structures. Pressure loading is suitable for pipes, pressure vessels and honeycomb structures, but it is not suitable for solid laminates. As for mechanical loading, it suffers from intolerable rigid body motion during loading, which is critical for shearography measurements. Moreover, it is challenging to apply mechanical loads to thick structures. Apart from these issues, the three loadings mentioned above appear to be difficult to use to reveal the presence of deep defects since strain anomalies caused by the deep defects may be too small to be covered up by the whole body deformation or other background noise signals.

Among the different loading methods, thermal loading has the advantages of being non-contact, versatile, cost-effective and convenient for on-site inspection. It should be noted that this loading has the same issue as other loadings do when detecting deep defects (Figure 2.4(a)), but this issue can be potentially reduced by considering that the applied heat can propagate through a thick structure (Figure 2.4(b)). Given that the applied heat can reach the defect region and interact with the defect (Figure 2.4(c)), it is promising to highlight the presence of internal defects at significant depth when the absorbed heating energy is up to a level (Figures 2.4(d)-2.4(e)).

In this research, thermal loading is developed for thick composite inspection with shearography.

Table 2.4: Common loading methods for shearography

Loading method	Description	Applicability in thick composites
Vacuum	Vacuum test chamber is required. Suitable for testing of tires, composite laminates and honeycomb	For large objects, the total enclosure is not practical
Pressure	Suitable for pressure vessels, pipes, honeycomb structures	Not suitable for solid laminates
Mechanical	A loading machine such as a tensile testing machine is usually needed	Generally occur with intolerable rigid body motion, special interferometric grade loading fixtures are needed
Thermal	Heating sources such as halogen lamps are easy to obtain and thermal loading is easy to perform	Versatility, cost-effectiveness, and convenience for on-site inspection.

2.3.4. SHEAROGRAPHY NDT OF COMPOSITE MATERIALS

Shearography with thermal loading has been applied successfully to structures of solid laminates and composite sandwich panels for qualitative inspections [37, 47, 62–64]. Many of these applications use single channel shearography systems because of the simple optical set-up and convenience for industrial applications. Thermal loading can be performed by using a halogen or IR lamp [37, 47] where the measurement surface is being illuminated by light to transfer heat and to propagate inside the test object (containing a wavelength range from the visible and infrared spectrum). Common heating methods including pulse, long pulse and step-heating excitations have been used for shearography. However, the problems of rapid heat dissipation and non-uniform heating may exist in the thermal excitations [21, 22]. Benefiting from the improvement of heating sources and modulation techniques, lock-in or periodical thermal excitations have been adopted for shearography NDT, and the mono- or multi-frequent periodical loading can be applied by modulated optical heating or inductive heating [53–55, 65]. The combination of the lock-in method and Fourier transformation improved the signal-to-noise ratio in defect detection with shearography, in addition, defects located in different depths can be distinguished by changing the modulation frequency [54, 55]. Later multi-flash or a series of flash pulse excitation has been used for shearography [66]. This method yields results of a similar quality to that of lock-in measurements while allowing a much shorter measurement time. More recently, frequency-modulated photothermal excitation has been utilized in shearography and depth-tomographic profiles of subsurface structure can be generated [67]. To sum up, the aforementioned studies have made significant contributions to developing shearography inspection, increasing its readiness level, and allowing efficient inspection of composite materials. However, these studies were limited to thin materials (less than 10 mm thickness) and shallow defects.
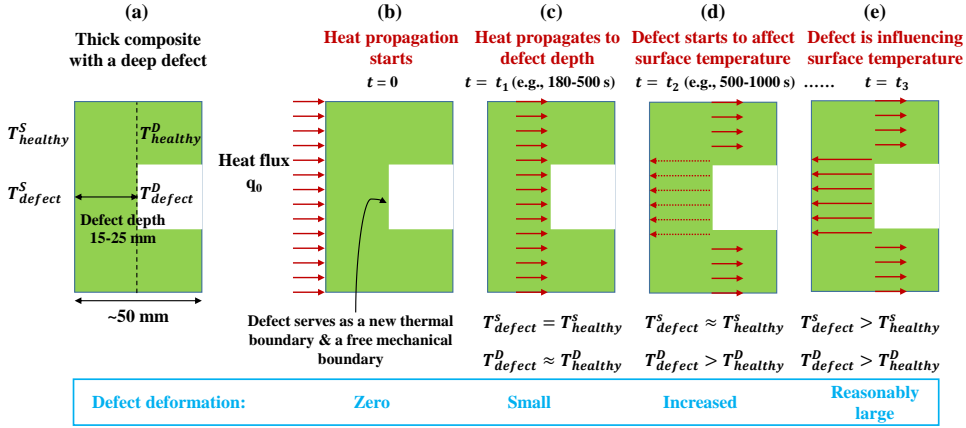
Figure 2.4: Thermal loading interacts with a deep defect (e.g., 15-25 mm depth) in a thick composite. (a) Schematic of the thick composite with the deep defect, T^S_{defect} and $T^S_{healthy}$ represent the surface temperature from defective and healthy regions, respectively; T^D_{defect} and $T^D_{healthy}$ represent the temperature at the defect depth from defective and healthy regions, respectively. (b) At time 0 s, heat propagation starts. (c) At time t_1, heat propagates to defect depth. (c) Heat propagation continues. At time t_2, the presence of the defect starts to affect surface temperature. (d) At time t_3, the defect is influencing surface temperature apparently.

Practical industrial inspection is usually complicated because experiments have problems such as whole body or global deformation, non-uniform heating and vibrations. Therefore reliable finite element method (FEM) guidance is needed. Studies on combining FEM with digital shearography have already been reported in literature [64, 68, 69]. Akbari et al. [70] studied the thermal loading parameters in a shearography test by using a numerical-experimental approach. More recently, Yang et al. [71] simulated defect detection of thin materials under various loading scenarios and evaluated the ability of detection with shearography. Buchta et al. [72] combined finite element analysis with shearography testing to monitor artwork. The above-mentioned studies were focused on thin composite materials and shallow defects. The number of major defects studied was also limited (1-2 artificial defects).

While applications of shearography NDT for thin composite materials and shallow defects were well discussed in literature, the research for thick composite inspection was sparse. In the very limited references to shearography NDT of thick composites, only experimental research had been conducted by few researchers [73, 74]. Hence, there is a need for shearography research towards quantitative, predictable and safe inspection of thick composites, and also towards reliable detection and characterisation of deep defects.

2.4. HEAT TRANSFER IN SOLIDS

As heat propagation plays an important role in this research (Figure 2.4), this section introduces some basics on heat transfer. Heat transfer is thermal energy in transit due

to a spatial temperature difference. It is characterised by the mechanisms of conduction, convection and radiation [75, 76].

Conduction may be viewed as the energy transfer from the more energetic to the less energetic particles of a substance due to interactions between the particles. In a solid, the modern view of conduction is to ascribe the energy transfer to lattice waves induced by atomic motion. Convection refers to the heat transfer that occurs between a surface and a moving fluid when they are at different temperatures. Radiation is energy emitted by matter that is at a nonzero temperature. The energy of the radiation field is transferred by electromagnetic waves. It is noted that the transfer of energy by radiation does not require the presence of a material medium, and radiation transfer occurs most efficiently in a vacuum [76].

2.5. SUMMARY

THIS chapter contained the literature review that provides the background necessary to understand the conducted research. The NDT of thick composites is challenging considering the complexity of materials and structures, the significant thickness and the high stiffness of the thick composites. Since its first demonstration, shearography or speckle pattern shearing interferometry has emerged as a powerful measurement technique for NDT and for surface strain measurement. This thesis aims to develop shearography methods with thermal loadings to composites with thicknesses of 50-60 mm and more that are common in the marine, wind energy and aerospace sectors.

REFERENCES

[1] C. Hellier, *Handbook of Nondestructive Evaluation* (McGraw-Hill Education, 2003).

[2] M. Omar, *Nondestructive testing methods and new applications* (IntechOpen, Rijeka, 2012).

[3] M. Ibrahim, *Nondestructive testing and structural health monitoring of marine composite structures,* in *Marine Applications of Advanced Fibre-Reinforced Composites*, Woodhead Publishing Series in Composites Science and Engineering, edited by J. Graham-Jones and J. Summerscales (Woodhead Publishing, 2016) pp. 147–183.

[4] E. Greene, *Inspection techniques for marine composite construction and NDE,* Report No SSC-463, United States Ship Structure Committee, Washington, DC (2012).

[5] R. M. Groves, *Inspection and monitoring of composite aircraft structures,* in *Comprehensive Composite Materials II*, edited by P. W. Beaumont and C. H. Zweben (Elsevier, Oxford, 2018) pp. 300–311.

[6] H. Taheri and A. A. Hassen, *Nondestructive ultrasonic inspection of composite materials: A comparative advantage of phased array ultrasonic,* Applied Sciences **9** (2019).

[7] G. M. Revel, G. Pandarese, and A. Cavuto, *Advanced ultrasonic non-destructive testing for damage detection on thick and curved composite elements for constructions,* Journal of Sandwich Structures & Materials **15**, 5 (2013).

[8] D. Chimenti, *Review of air-coupled ultrasonic materials characterization,* Ultrasonics **54**, 1804 (2014).

[9] E. Blomme, D. Bulcaen, and F. Declercq, *Air-coupled ultrasonic NDE: experiments in the frequency range 750 kHz–2 MHz,* NDT & E International **35**, 417 (2002).

[10] R. Montanini and F. Freni, *Non-destructive evaluation of thick glass fiber-reinforced composites by means of optically excited lock-in thermography,* Composites Part A: Applied Science and Manufacturing **43**, 2075 (2012).

[11] N. Tao, A. G. Anisimov, M. Elenbaas, and R. M. Groves, *Shearography non-destructive testing of a composite ship hull section subjected to multiple impacts,* in *Proceedings of the 20th European Conference on Composite Materials: Composites Meet Sustainability,* edited by A. Vassilopoulos and V. Michaud (2022) pp. 469–474.

[12] L. Sinha, D. Das, A. N. Nayak, and S. K. Sahu, *Experimental and numerical study on free vibration characteristics of laminated composite plate with/without cut-out,* Composite Structures **256**, 113051 (2021).

[13] S. Sahu and P. Das, *Experimental and numerical studies on vibration of laminated composite beam with transverse multiple cracks,* Mechanical Systems and Signal Processing **135**, 106398 (2020).

[14] H. S. Panda, S. K. Sahu, P. K. Parhi, and A. V. Asha, *Vibration of woven fiber composite doubly curved panels with strip delamination in thermal field,* Journal of Vibration and Control **21**, 3072 (2015).

[15] Y. Hung, Y. Chen, S. Ng, L. Liu, Y. Huang, B. Luk, R. Ip, C. Wu, and P. Chung, *Review and comparison of shearography and active thermography for nondestructive evaluation,* Materials Science and Engineering: R: Reports **64**, 73 (2009).

[16] R. Yang and Y. He, *Optically and non-optically excited thermography for composites: A review,* Infrared Physics & Technology **75**, 26 (2016).

[17] M. Moradi and M. S. Safizadeh, *Experimental and numerical study of the effect of using polyurethane instead of teflon strip to simulate debonding defect in composite patch repairs aluminum plate under thermography inspection,* Composites Part B: Engineering **175**, 107176 (2019).

[18] M. Moradi and M. S. Safizadeh, *Edge disbond detection of carbon/epoxy repair patch on aluminum using thermography,* Composites Science and Technology **179**, 41 (2019).

[19] V. P. Vavilov and D. D. Burleigh, *Review of pulsed thermal NDT: Physical principles, theory and data processing,* NDT & E International **73**, 28 (2015).

[20] A. A. Badghaish and D. C. Fleming, *Non-destructive inspection of composites using step heating thermography,* Journal of Composite Materials **42**, 1337 (2008).

[21] M. Ibrahim, *Nondestructive evaluation of thick-section composites and sandwich structures: A review,* Composites Part A: Applied Science and Manufacturing **64**, 36 (2014).

[22] W. Nsengiyumva, S. Zhong, J. Lin, Q. Zhang, J. Zhong, and Y. Huang, *Advances, limitations and prospects of nondestructive testing and evaluation of thick composites and sandwich structures: A state-of-the-art review,* Composite Structures **256**, 112951 (2021).

[23] P. Lambrineas, J. Davis, B. Suendermann, P. Wells, K. Thomson, R. Woodward, G. Egglestone, and K. Challis, *X-ray computed tomography examination of inshore minehunter hull composite material,* NDT & E International **24**, 207 (1991).

[24] K. Tan, N. Watanabe, and Y. Iwahori, *X-ray radiography and micro-computed tomography examination of damage characteristics in stitched composites subjected to impact loading,* Composites Part B: Engineering **42**, 874 (2011).

[25] M. Mehdikhani, I. Straumit, L. Gorbatikh, and S. V. Lomov, *Detailed characterization of voids in multidirectional carbon fiber/epoxy composite laminates using x-ray micro-computed tomography,* Composites Part A: Applied Science and Manufacturing **125**, 105532 (2019).

[26] Y. Hung, *Shearography for non-destructive evaluation of composite structures,* Optics and Lasers in Engineering **24**, 161 (1996).

[27] L. Yang and J. Li, *Shearography,* in *Handbook of Advanced Non-Destructive Evaluation,* edited by N. Ida and N. Meyendorf (Springer International Publishing, Cham, 2018) pp. 1–37.

[28] T. Kreis, *Speckle metrology,* in *Handbook of Holographic Interferometry* (John Wiley & Sons, Ltd, 2004) Chap. 7, pp. 399–408.

[29] R. Sirohi, *Shearography and its applications – a chronological review,* Light: Advanced Manufacturing **3**, 35 (2022).

[30] Y.-K. Zhu, G.-Y. Tian, R.-S. Lu, and H. Zhang, *A review of optical NDT technologies,* Sensors **11**, 7773 (2011).

[31] W. Osten and G. Pedrini, *55 years of holographic non-destructive testing and experimental stress analysis: Is there still progress to be expected?* Light: Advanced Manufacturing **3**, 121 (2022).

[32] Y. Hung, *Applications of digital shearography for testing of composite structures,* Composites Part B: Engineering **30**, 765 (1999).

[33] W. Steinchen, L. Yang, G. Kupfer, and P. Mäckel, *Non-destructive testing of aerospace composite materials using digital shearography,* Proceedings of the Institution of Mechanical Engineers, Part G: Journal of Aerospace Engineering **212**, 21 (1998).

[34] Y. Hung, *Digital shearography versus TV-holography for non-destructive evaluation,* Optics and Lasers in Engineering **26**, 421 (1997).

[35] P. A. Howell, *Nondestructive evaluation (NDE) methods and capabilities handbook,* Tech. Rep. (2020).

[36] A. G. Anisimov, M. G. Serikova, and R. M. Groves, *3D shape shearography technique for surface strain measurement of free-form objects,* Applied Optics **58**, 498 (2019).

[37] J. W. Newman, *Shearography nondestructive testing of composites,* in *Comprehensive Composite Materials II*, edited by P. W. Beaumont and C. H. Zweben (Elsevier, Oxford, 2018) pp. 270–290.

[38] Q. Zhao, X. Dan, F. Sun, Y. Wang, S. Wu, and L. Yang, *Digital shearography for NDT: Phase measurement technique and recent developments,* Applied Sciences **8** (2018), 10.3390/app8122662.

[39] Y. Hung and H. Ho, *Shearography: An optical measurement technique and applications,* Materials Science and Engineering: R: Reports **49**, 61 (2005).

[40] Y. Hung, W. Luo, L. Lin, and H. Shang, *Evaluating the soundness of bonding using shearography,* Composite Structures **50**, 353 (2000).

[41] Z. Liu, J. Gao, H. Xie, and P. Wallace, *NDT capability of digital shearography for different materials,* Optics and Lasers in Engineering **49**, 1462 (2011).

[42] H. Shang, C. Soh, and F. Chau, *The use of carrier fringes in shearography for locating and sizing debonds in GRP plates,* Composites Engineering **1**, 157 (1991).

[43] R. Růžek, R. Lohonka, and J. Jironč, *Ultrasonic C-scan and shearography NDI techniques evaluation of impact defects identification,* NDT & E International **39**, 132 (2006).

[44] A. G. Anisimov and R. M. Groves, *Extreme shearography: Development of a high-speed shearography instrument for quantitative surface strain measurements during an impact event,* Optics and Lasers in Engineering **140**, 106502 (2021).

[45] B. C. de Oliveira, P. Nienheysen, C. R. Baldo, A. A. Gonçalves, and R. H. Schmitt, *Improved impact damage characterisation in CFRP samples using the fusion of optical lock-in thermography and optical square-pulse shearography images,* NDT & E International **111**, 102215 (2020).

[46] C. Garnier, M.-L. Pastor, F. Eyma, and B. Lorrain, *The detection of aeronautical defects in situ on composite structures using non destructive testing,* Composite Structures **93**, 1328 (2011).

[47] D. Francis, R. P. Tatam, and R. M. Groves, *Shearography technology and applications: a review,* Measurement Science and Technology **21**, 102001 (2010).

[48] Y. Hung, L. Yang, and Y. Huang, *Non-destructive evaluation (NDE) of composites: digital shearography,* in *Non-Destructive Evaluation (NDE) of Polymer Matrix Composites*, Woodhead Publishing Series in Composites Science and Engineering, edited by V. M. Karbhari (Woodhead Publishing, 2013) pp. 84–115.

[49] F. Sun, Y. Wang, P. Yan, Q. Zhao, and L. Yang, *The application of SLM in shearography detecting system,* Optics and Lasers in Engineering **114**, 90 (2019).

[50] F. A. A. da Silva, D. P. Willemann, A. V. Fantin, M. E. Benedet, and A. A. Gonçalves, *Evaluation of a novel compact shearography system with DOE configuration,* Optics and Lasers in Engineering **104**, 90 (2018).

[51] R. M. Groves, *Development of shearography for surface strain measurement of non-planar objects,* Cranfield University (2001).

[52] R. M. Groves, S. W. James, and R. P. Tatam, *Multi component shearography employing four measurements channels,* in *Speckle Metrology 2003*, Vol. 4933, edited by K. Gastinger, O. J. Lokberg, and S. Winther, International Society for Optics and Photonics (SPIE, 2003) pp. 135 – 140.

[53] H. Gerhard and G. Busse, *Lockin-ESPI interferometric imaging for remote non-destructive testing,* NDT & E International **39**, 627 (2006).

[54] P. Menner, H. Gerhard, and G. Busse, *Lockin-speckle-interferometry for non-destructive testing,* in *Interferometry XIV: Techniques and Analysis*, Vol. 7063, edited by J. Schmit, K. Creath, and C. E. Towers, International Society for Optics and Photonics (SPIE, 2008) p. 70630C.

[55] M. Rahammer, P. Menner, and G. Busse, *Thermal waves for NDE of aircraft: comparison of lockin thermography and lockin interferometry,* Quantitative InfraRed Thermography Journal **10**, 42 (2013).

[56] A. G. Anisimov, B. Müller, J. Sinke, and R. M. Groves, *Analysis of thermal strains and stresses in heated fibre metal laminates,* Strain **54**, e12260 (2018).

[57] Y. Y. Hung and C. Y. Liang, *Image-shearing camera for direct measurement of surface strains,* Appl. Opt. **18**, 1046 (1979).

[58] L. Yang and X. Xie, *Digital shearography: new developments and applications* (SPIE press, 2016).

[59] K. Creath, *Phase-measurement interferometry techniques,* (Elsevier, 1988) pp. 349–393.

[60] J. Novak, *Five-step phase-shifting algorithms with unknown values of phase shift,* Optik **114**, 63 (2003).

[61] Y. Hung, *Shearography: A novel and practical approach for nondestructive inspection,* Journal of Nondestructive Evaluation **8**, 55 (1989).

[62] P. Ochôa, V. Infante, J. M. Silva, and R. M. Groves, *Detection of multiple low-energy impact damage in composite plates using lamb wave techniques,* Composites Part B: Engineering **80**, 291 (2015).

[63] D. T. Goto, M. I. Faraz, C. D. Rans, and R. M. Groves, *Low energy impact damage detection using shearography,* Proc. Photomechanics (2011).

[64] J.-F. Vandenrijt, H. Xiong, C. Lequesne, P. Blain, and M. Georges, *Shearography inspection of monolithic CFRP composites: finite element modeling approach for assessing an adequate strategy of artificial defects representing delamination,* in *Optical Measurement Systems for Industrial Inspection XI,* Vol. 11056, edited by P. Lehmann, W. Osten, and A. A. G. Jr., International Society for Optics and Photonics (SPIE, 2019) p. 110560I.

[65] P. Pfeffer, L. Wachter, D. Hoffmann, C. Kolb, G. Schober, and M. Bastian, *A study of multifrequent shearographic lock-in measurements of CFRP,* in *International Symposium on Structural Health Monitoring and Nondestructive Testing 4-5 Oct 2018, Saarbrücken, Germany.*

[66] P. Pfeffer, L. Wachter, D. Hoffmann, M. Bastian, and G. Schober, *Multiple-flash shearography–a new NDT method for reducing thermal stresses during the inspection process,* in *10th International Symposium on NDT in Aerospace, Oct 2018, Dresden, Germany.*

[67] L. Liu, C. Guo, Y. Xiang, Y. Tu, L. Wang, and F.-Z. Xuan, *Photothermal radar shearography: A novel transient-based speckle pattern interferometry for depth-tomographic inspection,* IEEE Transactions on Industrial Informatics **18**, 4352 (2022).

[68] E. C. Krutul and R. M. Groves, *Opto-mechanical modelling and experimental approach to the measurement of aerospace materials using shearography and thermal loading,* in *Modeling Aspects in Optical Metrology III,* Vol. 8083, edited by B. Bodermann, International Society for Optics and Photonics (SPIE, 2011) p. 80831C.

[69] G. De Angelis, M. Meo, D. Almond, S. Pickering, and S. Angioni, *A new technique to detect defect size and depth in composite structures using digital shearography and unconstrained optimization,* NDT & E International **45**, 91 (2012).

[70] D. Akbari, N. Soltani, and M. Farahani, *Numerical and experimental investigation of defect detection in polymer materials by means of digital shearography with thermal loading,* Proceedings of the Institution of Mechanical Engineers, Part B: Journal of Engineering Manufacture **227**, 430 (2013).

[71] F. Yang, X. Ye, Z. Qiu, B. Zhang, P. Zhong, Z. Liang, Z. Sun, and S. Zhu, *The effect of loading methods and parameters on defect detection in digital shearography,* Results in Physics **7**, 3744 (2017).

[72] D. Buchta, C. Heinemann, G. Pedrini, C. Krekel, and W. Osten, *Combination of FEM simulations and shearography for defect detection on artwork,* Strain **54**, e12269 (2018).

2

[73] W. J. Murri, B. W. Sermon, R. N. Andersen, L. A. Martinez, E. J. Van der Heiden, and C. A. Garner, *Defects in thick composites and some methods to locate them,* in *Review of Progress in Quantitative Nondestructive Evaluation*, edited by D. O. Thompson and D. E. Chimenti (Springer US, Boston, MA, 1991) pp. 1583–1590.

[74] F. L. di Scalea, J. B. Spicer, and R. E. G. Jr., *Electronic shearography with thermal loading for detecting debonds in thick polyurethane/steel panels for marine applications,* Research in Nondestructive Evaluation **12**, 43 (2000).

[75] L. Shi, *Heat transfer in the thick thermoset composites,* Delft University of Technology (2016).

[76] T. L. Bergman, F. P. Incropera, D. P. Dewitt, and A. S. Lavine, *Fundamentals of heat and mass transfer* (John Wiley & Sons, 2017).

3

METHODOLOGY

For clarity, the motivation and main objectives of this research, which have been elaborated in previous chapters, are summarized below:

In this thesis, the research goal is to develop an inspection method (i.e., shearography method with thermal excitations) to inspect composites with a thickness of 50-60 mm and more, which are common in the marine sector.

Nowadays thick composite materials tend to be used in safety-critical applications such as large primary or secondary load-bearing structures, where a structural failure may cause catastrophic consequences. Hence, it is important to advance NDT towards the inspection of composite structures of significant thickness for improving the safety, reliability and maintenance of these structures. Nevertheless, due to the complexity in materials and structures, the significant thickness and the high stiffness of the thick composites, the non-destructive testing and inspection of these materials remain an urgent challenge (especially in the detection of deeply buried defects) [1, 2]. Among the various NDT techniques, digital shearography is an optical interferometric method with the advantages of non-contact inspection, good applicability in the in-service environment, good inspection productivity and the excellent ability for detecting critical defects [3, 4]. Therefore it has been chosen as the main NDT technique for the research.

3.1. RESEARCH QUESTIONS

To realize the research goal, the following main research question addressed in this thesis is:

How to develop a novel shearography method with modulated thermal excitations for the inspection of thick composite structures that enables the detection and characterisation of deep defects?

Furthermore, in order to answer the main research question, the following sub-research questions (RQ) have been formulated:

   RQ1 *What are the defect detection capabilities, inspection limitations and new possibilities of shearography NDT for thick composites?*

   RQ2 *How can spatially modulated heating be developed for improving thick composite inspection with shearography?*

   RQ3 *How can temporally modulated heating be developed for improving thick composite inspection with shearography?*

   RQ4 *What is the efficacy of the shearography inspection system for full-scale structures (e.g., composite ship hull section) in the in-service environment?*

As elaborated in Section 1.3, the NDT defect detection capabilities and inspection limitations for thick composites have not been fully characterised. So the first step is to investigate the defect detection capabilities of shearography for inspecting thick composites (RQ1, Figure 3.1(a)). This will be studied on a thick glass fibre-reinforced polymer (GFRP) laminate by combining FEM simulations and shearography experiments. RQ1 will be addressed in Chapter 4.

The principle of shearography relies on deformation changes of the test object surface. Therefore developing shearography for NDT eventually becomes developing a suitable

method of loading to deform the object that can reveal defects [5–7]. The core idea here is to apply modulated heating for shearography NDT. RQ2 and RQ3 deal with developing shearography methods with spatially and temporally modulated thermal loading schemes to improve defect detection and characterisation (Figures 3.1(b-c)). Both experiments and finite element modelling will be used in this research (Figures 3.1(d-e)) to investigate the influence of different thermal excitations on defect detection and defect behaviour characterisation in thick composites. These two RQs will be addressed in Chapters 5 and 6.

There is an increasing need for performance validation of NDT techniques on large-scale engineering structures in the in-service environment [3]. RQ4 deals with the application of the shearography inspection system on a demonstrator of a large-scale composite ship hull section at a shipyard. Both thermal and mechanical loadings will be performed to evaluate the corresponding efficacies in defect detection. RQ4 will be addressed in Chapter 7.
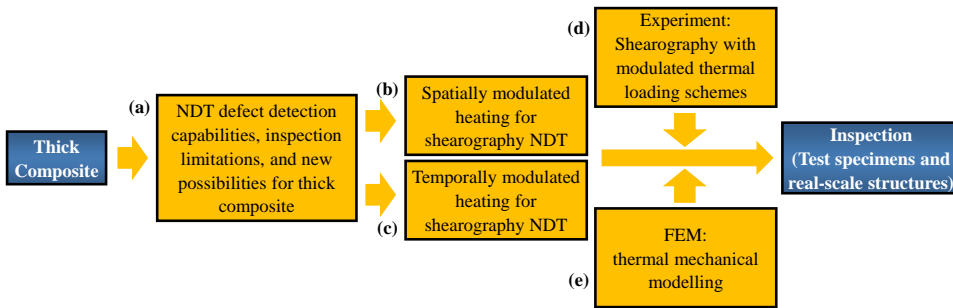
Figure 3.1: Research workflow

3.2. SPECIMEN DESCRIPTION AND MATERIAL PROPERTIES

A large GFRP composite laminate panel (about 1600 mm × 590 mm in size) representative of composite ship construction was manufactured by Damen Shipyards. The layup of the GFRP laminate is $[0/45/90/-45]_{60}$ and the thickness is about 51 mm. This laminate panel is made from E-glass fibre and vinyl ester resin which have found widespread applications in the marine sector. The specimens for this study (Figure 3.2(a)) are cut from this large laminate panel. The size of the specimens is 600 mm × 450 mm (Chapters 4 and 6) or 300 mm × 300 mm (Chapter 5). To reliably simulate major defects in thick composites, the specimens were machined to form various flat bottom holes of different diameters and of different remaining thicknesses, following a common practice in research papers [8–10] and industrial applications [11, 12]. Here the selection of layup, thickness of the material, defect depth and size are representative for marine composites [3, 13].

Table 3.1 shows the experimentally measured material properties of the specimen. To obtain these material properties, 87 small samples (4 layers of fibre) were designed and manufactured to measure Young's modulus, shear modulus and Poisons ratio in different directions (data obtained from colleagues) according to ASTM Standards D3039/D3039M-

14 [14], D3410/D410M-03 [15], and D7078/D7078M-12 [16], respectively. 15 tests were performed for determining each one of the in-plane material properties and 6 tests were performed for determining each one of the out-of-plane shear properties. The tensile tests were performed by using the Electromechanic Universal Test Machine, and the compressive tests were performed by using a Zwick Materials Testing Machine. A Material Test 810 System was used for the shear tests. Besides, the density and the fibre volume ratio were determined by using a Mettler Toledo (AB204-S) balance and a Nabertherm oven (30-3000 °C), respectively. The thermal expansion coefficients of the laminate were measured with thermomechanical analysis (TMA) on a Perkin Elmer Diamond TMA, and the specific heat of the laminate was measured with modulated differential scanning calorimetry (MDSC) on a Perkin Elmer DSC 8000.

Table 3.1: Material properties for E-glass fibre/vinyl ester resin laminate

Property	Unit	Value	Description	Reference
E_{11}	GPa	37.9	Elastic modulus of a ply	[14]
E_{22}	GPa	12.0		[14]
E_{33}	GPa	12.0		$E_{33} = E_{22}$ assumed
G_{12}	GPa	5.0	Shear modulus of a ply	[16]
G_{23}	GPa	4.1		[16]
G_{13}	GPa	3.7		[16]
ν_{12}	[-]	0.3	Poisson's ratios of a ply	[14]
ν_{13}	[-]	0.3		$\nu_{13} = \nu_{12}$ assumed
ν_{23}	[-]	0.4		[17]
α_x	$10^{-6}/°C$	19.18	Coefficients of thermal	TMA
α_y	$10^{-6}/°C$	20.81	expansion of the laminate	TMA
α_z	$10^{-6}/°C$	46.80		TMA
c_p	$J/(kg·°C)$	803	Specific heat at 20 °C	TMA
ρ	kg/m^3	1971	Density	Mettler Toledo
V_f	%	57	fibre volume ratio	Nabertherm
k_1	$W/(m·°C)$	0.81	Thermal conductivity along fibre direction	[18]
k_2	$W/(m·°C)$	0.36	Thermal conductivity along fibre direction	[18]
k_3	$W/(m·°C)$	0.36	Thermal conductivity along fibre direction	[18]

Note: Young's modulus, shear modulus and Poisons ratio in different directions were obtained from colleagues.

It should be noted that the out-of-plane elastic modulus, the out-of-plane Poisson's ratios, and the thermal conductivities of the ply are unknown. For a single ply, it was assumed that $E_{33} = E_{22}$ and $\nu_{13} = \nu_{12}$. Out-of-plane Poisson's ratio ν_{23} was calculated based on the self-consistent field model [17]. In order to calculate thermal conductivities

in Table 3.1, first the material properties of the resin and glass-fibre were obtained from the material manufacturer and previous projects [19]. Then the micro-mechanical relations (the Halpin-Tsai equations) were applied to calculate thermal conductivities along and transverse to the fibre directions [18].

To understand the material and structural complexity of the studied GFRP specimen, Micro-CT scans (Figure 3.2(b)) were performed for the inspection of small samples (about 25 mm × 20 mm × 51 mm) cut from the same GFRP laminate panel. A few manufacturing defects, e.g., voids, were found in the material. As these manufacturing defects are small (0-2 mm) compared with the artificial defects (30-120 mm), they can be neglected in this study. Nevertheless, it should be acknowledged that the presence of manufacturing defects and imperfections might affect local mechanical and thermal properties, e.g., local stiffness.

The GFRP specimens
(a)

3D reconstructed CT scan

CT cross-sectional view showing internal stitched structure
(b)
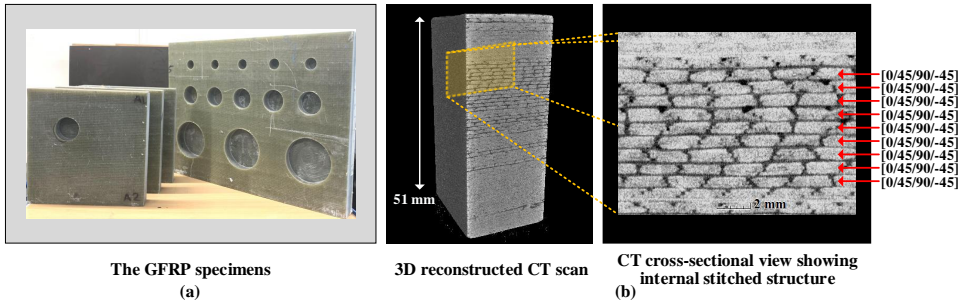
Figure 3.2: (a) The 51 mm thick GFRP specimens studied in the research, specimens are 300-600 mm in lateral. (b) Micro-CT scan of a small GFRP sample (25 mm × 20 mm × 51 mm). The specimens and the sample were cut from the same larger GFRP panel.

3.3. Experimental methods

3.3.1. Shearogaphy system enabling continuous strain measurement

The in-house built experimental shearography system for thick composite inspection is shown in Figure 3.3. The experimental system was built upon a previously developed 3D shape shearography instrument [20, 21]. The 3D shearography instrument contained three shearing cameras that were spatially distributed in a "T" configuration using an Alufix modular fixture system (Figure 3.3(a)). The shearing cameras included Basler Pilot piA2400 cameras (2456×2058 pixels) with Linos MeVis-C 1.6/25 imaging lenses (Figures 3.3(a) and 3.3(b)). Each camera had a Michelson shearing interferometer with temporal phase-shifting realised by a piezo-electric actuator PSH 4z (Piezosystem Jena). A Torus 532 CW laser (Laser Quantum, wavelength of 532 nm, operating at 200 mW optical power) was used to illuminate the surface of a specimen, whose front surface was sprayed with removable white paint in matt finish to increase the scattered light for the shearography inspection. The choice of cameras, lenses and laser source was due to the cost of optics suitable for 532 nm, camera sensitivity for this wavelength and commercial availability in the market. The 3D shearography instrument details and its application for material

characterisation can be found in [20, 21].

The 3D shearography instrument was upgraded for this research. The specifics of modifications are given here. A fourth shearing camera (Figure 3.3(b), Basler Pilot piA2400 camera and Linos MeVis-C 1.6/25 imaging lens with Michelson shearing interferometer) was added to the instrument close to parallel to the laser beam to provide pure out-of-plane surface strain measurement. In this thesis, the choice of focusing on the out-of-plane deformation was made as the corresponding deformation is expected to be predominant for flat-bottom holes and delaminations. The field of view (FOV) of the fourth shearography camera was about 300×300 mm^2 for the specimen at a distance of 1.0 m from the instrument (Figure 3.3(a)). Halogen lamps of 0.2 m in diameter and 0.4 m in length (Figure 3.3(c), SUPER PAR CP62) were used to apply thermal loading to the test object. The distance between the lamps and the specimen was in the range of 0.8-1.0 m. The nominal electrical power of the lamps was 1000 W (for each lamp). The actual power was controlled remotely by specific hardware. The surface temperature of the specimen was monitored with K-type thermocouples (TCs) and/or a FLIR A655 infrared camera (640×480 pixels) that detects temperature differences down to <30 mK.
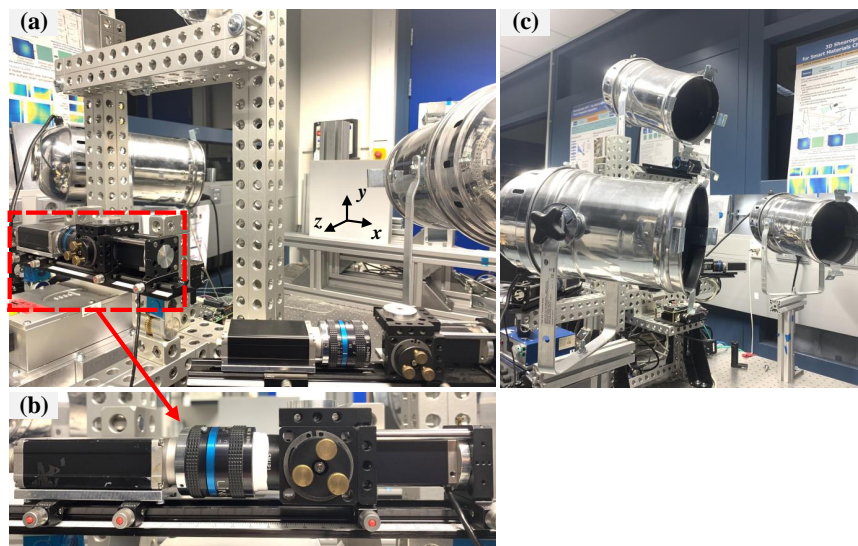
Figure 3.3: (a) Experimental shearography system with thermal loading (1.1 m tall, 1.1 m wide) developed for thick composite inspection, the working distance was approx. 1.0 m. (b) The fourth shearing camera with the main focus on the out-of-plane deformation. (c) Halogen lamps as heating sources.

Traditional shearography methods suffer from a lack of awareness of the full process of transient deformation [22] and the applied load is usually not fully characterised [5, 6]. In this research, the whole surface thermal deformation of the specimen during the inspection can be continuously measured and analysed, thus enabling a comprehensive understanding of thick composite inspection.

The shearographic data processing procedure is as follows (Figure 3.4). First, the opti-

cal phases ϕ_m of the recorded sets of phase-shifted speckle interferograms were computed by using temporal phase-shifting methods (e.g., five-step or three-step phase-shifting). Then the phase difference sequence of neighboring sets $\delta\phi_{m-1,\,m}$ can be generated:

$$\delta\phi_{m-1,\,m} = \phi_m - \phi_{m-1} \tag{3.1}$$

By summing up the phase difference sequence, a stack of phase maps $\Phi_{0,\,m}$ corresponding to the reference state right after heating (t_0) was built up, representing the evolution of thermal deformation in the out-of-plane direction during the inspection:

$$\Phi_{0,\,m} = \sum_{i=1}^{m} \delta\phi_{i-1,i} \tag{3.2}$$

As the efficacy of thick composite inspection with shearography may vary with different reference states [23], the change of reference state from t_0 to t_m can be achieved by the equation below:

$$\Phi_{m,\,i} = \Phi_{0,\,i} - \Phi_{0,\,m} \tag{3.3}$$

Once the phase maps are obtained, the strain maps can be further calculated. For example, for x-shearing direction the strain map ($\partial w / \partial x$) with reference state at t_0 is:

$$\frac{\partial w}{\partial x} = \frac{\lambda}{4\pi\delta x}\Phi_{0,\,m} \tag{3.4}$$

Eq. 3.4 also shows that shear distance calibration (δx) is important for shearography towards quantitative inspection and defect behaviour characterisation.
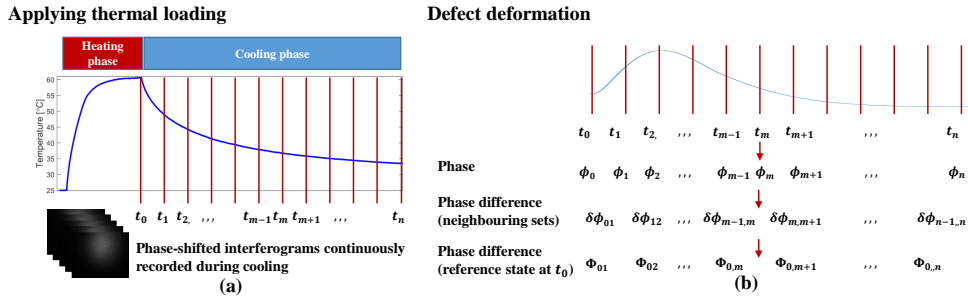
Figure 3.4: Shearography with thermal heating: (a) continuous measurement during cooling. (b) Sequential shearographic data processing

It should be addressed that during heating shearography measurements are usually not available as the light from the lamps will saturate the shearography camera sensor (e.g., under continuous heating). In these cases, the measurements are taken only during cooling (Chapters 4 and 6). In other cases where cyclic heating is used (Chapter 5), the shearography measurements can be performed during heating. This is attributed to the gaps in the heating that allow intermediate speckle interferograms to be captured.

3.3.2. Thermocouple and IR camera sensors for temperature measurement

During the experiments, halogen lamps were applied to heat the test specimen. The transient temperature on the specimen surface was monitored during inspection with the thermocouples and/or the IR camera. The measured transient temperature was further used for characterising the actual heat flux on the surface during experiments, serving as an input for simulating thermal loading in Abaqus. The details on experimentally determining the heat flux on the specimen surface will be reported later in Sections 4.3.2 and 5.3.2.

3.3.3. Signal processing

As introduced in Section 2.3.2, after applying temporal phase-shifting methods, phase filtering and phase unwrapping are required to denoise and to remove phase fringe discontinuities. In this research, the phase fringe maps were sin/cos filtered with iterative circular averaging and median filters with a radius of 6 pixels and an aperture of 5×5 pixels respectively, further unwrapped with the branch-cut method [24].

It is reported [21, 25] that in a shearography setup, the shearing amount across the whole field of view (FOV) of the shearography camera may be not the same due to aberrations and wavefront errors of the optical elements. Hence, the shear distance δx over the FOV was calibrated according to [21, 25] to take into account the errors due to aberrations and misalignment of components of the shearing interferometer and of the imaging lens, including the aberrations and manufacturing errors of the beamsplitter, non-flatness of the mirrors, lens aberrations (incl. distortion). During the shear calibration, a predefined checkerboard was adhered onto the specimen surface. A reference image and a sheared image were captured by blocking the shutters in the shearing arm and the reference arm of the interferometer (one at a time). The corner coordinates of the checkboard from the reference and sheared images were identified and compared to calibrate the shear distance over the FOV. The calibrated shear was important to obtain quantitative surface strains from the buried defects (Chapter 4) and to correct simulated phase maps (Chapters 5 and 6).

The original phase map or strain map with shearography contains defect-induced deformation that represents the defect signal as well as overall or global deformation that represents the background signal. To extract defect-induced deformation for defect detection and characterisation, a phase compensation process was performed. First a fitting surface was created by using polynomial fitting to represent overall deformation, and the subtraction between the original phase map and the fitting surface gives the defect-induced phase (DIP) map, which is related to defect-induced deformation (DID). In the research, a third-degree or fourth-degree polynomial function over the phase map was used for phase compensation.
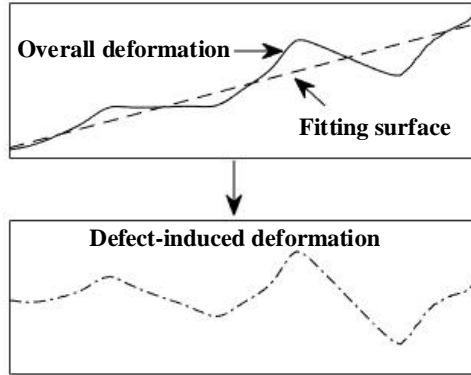
Figure 3.5: Sketch of phase compensation for deriving defect-induced deformation, a 3rd or 4th degree polynomial over the phase map was used for phase compensation.

The fitting plane created by the polynomial fitting works well for conventional global heating cases, nevertheless, it may not be useful for complicated heating cases, e.g., spatially modulated heating in Chapter 5. To overcome this problem, a reference panel (defect-free) is necessary to compare with a defective one for deriving defect-induced deformation. The related results will be reported in Section 5.4.2.

3.4. FINITE ELEMENT MODELLING

THIS research utilises FEM to achieve a comprehensive understanding of thick composite inspection with shearography. Note that because the composite laminate ([0/+45/90/-45]$_{60}$) studied in this research consists of large numbers of a repeating sublaminate, effective mechanical and thermal properties have been calculated for the laminate for use in the modelling in order to save memory and computational time.

3.4.1. EFFECTIVE MECHANICAL AND THERMAL PROPERTIES FOR THICK COMPOSITE MODELLING

Several mathematical methods have been reported to determine the equivalent elastic properties of laminates in literature [26–29]. Among them, Sun and Li [29] derived expressions of effective elastic constants for thick laminates by employing a longwave concept. Hoorn et al. [30] derived expressions for equivalent laminate mechanical properties with the equal strain assumption. Both of the methods can obtain three-dimensional elastic properties and the results from the methods derived in [29] and [30] are compared in this section.

As shown in Table 3.2, the equivalent elastic modulus for composite laminate with substructure [0/45/90/-45] are computed according to [29] and [30], respectively. Results calculated from the two methods agree with each other well. Since the differences between the equivalent mechanical properties derived from the two methods are small (less than 1%), either method is feasible. In this study, the method in Ref. [30] was used for further modelling due to its ease of application.

Table 3.2: Comparison of effective modulus predictions for GFRP laminates

| | Unit | [0/45/90/-45] | | Differences | |
		Ref. [29]	Ref. [30]	Absolute	Relative
E_x	GPa	20.667	20.703	0.036	0.17%
E_y	GPa	20.667	20.703	0.036	0.17%
E_z	GPa	13.275	13.275	0	0
G_{xy}	GPa	8.094	8.117	0.023	0.28%
G_{yz}	GPa	3.897	3.909	0.012	0.30%
G_{xz}	GPa	3.897	3.909	0.012	0.30%
ν_{xy}	[-]	0.277	0.275	0.002	0.72%
ν_{yz}	[-]	0.309	0.309	0	0
ν_{xz}	[-]	0.309	0.309	0	0

Equivalent thermal conductivities of the laminate are also needed for modelling. The expressions derived in [31] are applied to determine the global conductivities of three directions for the thick laminate. For the GFRP laminate used in this research, the effective thermal conductivities k_x, k_y, k_z (W/m·°C) in the x, y, and z directions are 0.585, 0.585, and 0.36, respectively. Since the equivalent properties of the thick composite laminate can be derived, the laminate was modelled by using its equivalent properties.

3.4.2. THERMAL-MECHANICAL MODEL

A 3D thermal-mechanical model was developed in ABAQUS/Standard (implicit solver, coupled temp-displacement) to simulate the thermal and mechanical responses of the thick composite laminate during shearography inspection. Both thermal and mechanical boundary conditions were taken into consideration in the model. The developed model will be used to assist shearography NDT in determining loading parameters and the behaviour of the test object, which can advance shearography towards a quantitative and predictable inspection tool for thick composites.

It is important to note that an ideal mechanical boundary condition such as fully clamped is rather difficult to achieve in experiments as the thickness of the specimen is significant (~ 51 mm). Therefore the test panel was freestanding on the optical table during the shearography test, and to simulate this actual mechanical boundary condition, the displacement along the y-axis on the bottom surface is fixed Figure (3.3(a)). The experimentally determined heat flux distribution on the specimen surface was applied as an input of thermal loading in Abaqus. To compensate for heat loss from the composite to the environment, a heat transfer coefficient needs to be applied to the model. In literature, the free convection heat transfer coefficient of gas [32] is 2-25 W/(m^2·K), and considering that the air flow in the lab is relatively small, therefore a small value (2-12 W/(m^2·K)) was selected for the model. For the model mesh, there are 60 elements in the through-thickness direction (one element per equivalent layer). In the area with the defect, the mesh size is around 2×2 mm^2, while in the healthy region, the mesh size is around 4×4 or 5×5 mm^2 to make the computational time with the high-performance computing (HPC) cluster reasonable. The eight-node coupled temperature-displacement

element (C3D8T or C3D8RT) was selected for the FEM model because of its capabilities in coupled temperature-displacement analysis and its advantages of saving computational time.

The outputs from the model include temperature and displacement. To validate the model, the simulated temperature will be compared with the transient temperature measured with thermocouples at representative locations as well as the IR camera. It can be mentioned that the out-of-plane displacement cannot be compared with shearography results (e.g., phase and strain maps) directly, therefore a MATLAB code has been developed to calculate simulated phase and/or strain maps from the FEM displacement data. For example for simulated phase maps, it can be realised by calculating the out-of-plane displacement derivative from the out-of-plane displacement data and then transferring the obtained displacement derivative data into Eq. 2.4 in Section 2.3.1. The experimentally-determined calibrated shear distance over the specimen surface was implemented to obtain more accurate simulated phase maps.

3.5. GENERAL ENVIRONMENTAL AND EXPERIMENTAL PARAMETERS

S EVERAL environmental and experimental parameters including room temperature, shear distance, and thermal loading scheme varied in different experiments in Chapters 4-6.

First, room temperatures during experiments in these chapters varied in the range of 20-25 °C and the chosen heat transfer coefficients for the model in these chapters also had slight differences. These are practical variations considering the timespan of the PhD research.

Second, the calibrated shear distances in these chapters (in the range 5-8 mm) also had small differences because of the FOV of the camera and the distances between the specimen and the shearography setup. In this thesis, the shear distance was chosen by around 80% maximum output voltage of the piezo actuating system. This was experimentally determined to obtain good number of fringes for phase unwrapping and sufficient sensitivity for defect detection.

It should be addressed that these variations including room temperatures and shear distances do not affect the overall results and the conclusions.

Last, different thermal loading schemes were applied for shearography NDT of thick composites. The variables included duration of heating and cooling, heat flux, spatially and temporally modulated thermal loading schemes. The efficacy of defect detection using shearography depends on thermal loading schemes, namely how and when loading is applied. This is studied in detail in the following chapters.

REFERENCES

[1] M. Ibrahim, *Nondestructive evaluation of thick-section composites and sandwich structures: A review,* Composites Part A: Applied Science and Manufacturing **64**, 36 (2014).

[2] W. Nsengiyumva, S. Zhong, J. Lin, Q. Zhang, J. Zhong, and Y. Huang, *Advances,*

limitations and prospects of nondestructive testing and evaluation of thick composites and sandwich structures: A state-of-the-art review, Composite Structures **256,** 112951 (2021).

[3] E. Greene, *Inspection techniques for marine composite construction and NDE,* Report No SSC-463, United States Ship Structure Committee, Washington, DC (2012).

[4] J. W. Newman, *Shearography nondestructive testing of composites,* in *Comprehensive Composite Materials II*, edited by P. W. Beaumont and C. H. Zweben (Elsevier, Oxford, 2018) pp. 270–290.

[5] Y. Hung, *Shearography for non-destructive evaluation of composite structures,* Optics and Lasers in Engineering **24,** 161 (1996).

[6] Y. Hung, *Applications of digital shearography for testing of composite structures,* Composites Part B: Engineering **30,** 765 (1999).

[7] Y. Hung, L. Yang, and Y. Huang, *Non-destructive evaluation (NDE) of composites: digital shearography,* in *Non-Destructive Evaluation (NDE) of Polymer Matrix Composites*, Woodhead Publishing Series in Composites Science and Engineering, edited by V. M. Karbhari (Woodhead Publishing, 2013) pp. 84–115.

[8] Z. Liu, J. Gao, H. Xie, and P. Wallace, *NDT capability of digital shearography for different materials,* Optics and Lasers in Engineering **49,** 1462 (2011).

[9] G. De Angelis, M. Meo, D. Almond, S. Pickering, and S. Angioni, *A new technique to detect defect size and depth in composite structures using digital shearography and unconstrained optimization,* NDT & E International **45,** 91 (2012).

[10] D. Akbari, N. Soltani, and M. Farahani, *Numerical and experimental investigation of defect detection in polymer materials by means of digital shearography with thermal loading,* Proceedings of the Institution of Mechanical Engineers, Part B: Journal of Engineering Manufacture **227,** 430 (2013).

[11] P. A. Howell, *Nondestructive evaluation (NDE) methods and capabilities handbook*, Tech. Rep. (2020).

[12] ASTM E2581-07, *Standard practice for shearography of polymer matrix composites, sandwich core materials and filament-wound pressure vessels in aerospace applications,* (2011).

[13] S. Paboeuf, A. de Bruijn, F. Evegren, M. Krause, and M. Elenbaas, *A "fast track to approval" process for innovative maritime solutions,* in *Practical Design of Ships and Other Floating Structures*, edited by T. Okada, K. Suzuki, and Y. Kawamura (Springer Singapore, Singapore, 2021) pp. 51–63.

[14] D3039/D3039M-14, *Standard test method for tensile properties of polymer matrix composite materials* (ASTM international, 2014).

[15] DD3410/D410M-03, *Standard test method for compressive properties of polymer matrix composite materials with unsupported gage section by shear loading,* (2003).

[16] D7078/D7078M-12, *Standard test method for shear properties of composite materials by the V-notched beam method,* (2012).

[17] I. M. Daniel, O. Ishai, I. M. Daniel, and I. Daniel, *Engineering mechanics of composite materials*, Vol. 1994 (Oxford University Press New York, 2006).

[18] R. Rolfes and U. Hammerschmidt, *Transverse thermal conductivity of CFRP laminates: A numerical and experimental validation of approximation formulae,* Composites Science and Technology **54**, 45 (1995).

[19] L. Shi, *Heat transfer in the thick thermoset composites,* Delft University of Technology (2016).

[20] A. G. Anisimov, B. Müller, J. Sinke, and R. M. Groves, *Analysis of thermal strains and stresses in heated fibre metal laminates,* Strain **54**, e12260 (2018).

[21] A. G. Anisimov, M. G. Serikova, and R. M. Groves, *3D shape shearography technique for surface strain measurement of free-form objects,* Applied Optics **58**, 498 (2019).

[22] L. Liu, C. Guo, Y. Xiang, Y. Tu, L. Wang, and F.-Z. Xuan, *Photothermal radar shearography: A novel transient-based speckle pattern interferometry for depth-tomographic inspection,* IEEE Transactions on Industrial Informatics **18**, 4352 (2022).

[23] N. Tao, A. G. Anisimov, and R. M. Groves, *FEM-assisted shearography with spatially modulated heating for non-destructive testing of thick composites with deep defects,* Composite Structures **297**, 115980 (2022).

[24] D. C. Ghiglia and M. D. Pritt, *Two-dimensional phase unwrapping: theory, algorithms, and software,* Wiley New York (1998).

[25] D. T. Goto and R. M. Groves, *Error analysis of 3D shearography using finite-element modelling,* in *Optical Micro- and Nanometrology III*, Vol. 7718, edited by C. Gorecki, A. K. Asundi, and W. Osten, International Society for Optics and Photonics (SPIE, 2010) p. 771816.

[26] R. Enie and R. Rizzo, *Three-dimensional laminate moduli,* Journal of Composite Materials **4**, 150 (1970).

[27] N. J. Pagano, *Exact moduli of anisotropic laminates,* in *Mechanics of Composite Materials: Selected Works of Nicholas J. Pagano*, edited by J. N. Reddy (Springer Netherlands, Dordrecht, 1994) pp. 210–231.

[28] W. Chan, C. Lin, Y. Liang, and C. Hwu, *Equivalent thermal expansion coefficients of lumped layer in laminated composites,* Composites Science and Technology **66**, 2402 (2006), special Issue in Honour of Professor C.T. Sun.

[29] C. Sun and S. Li, *Three-dimensional effective elastic constants for thick laminates,* Journal of Composite Materials **22**, 629 (1988).

3

[30] N. van Hoorn, C. Kassapoglou, and W. van den Brink, *Impact response prediction and sensitivity analysis of thick laminated composite plates*, techreport NLR-TP-2019-529, NLR - Royal Netherlands Aerospace Centre (2019).

[31] M. Kulkarni and R. Brady, *A model of global thermal conductivity in laminated carbon/carbon composites*, Composites Science and Technology **57**, 277 (1997).

[32] T. L. Bergman, F. P. Incropera, D. P. Dewitt, and A. S. Lavine, *Fundamentals of heat and mass transfer* (John Wiley & Sons, 2017).

3

4

FEM-ASSISTED SHEAROGRAPHY FOR THICK COMPOSITES: NDT CAPABILITIES

This chapter aims to study the NDT defect detection capabilities and inspection limitations in thick composite materials, which addresses RQ 1 - 'What are the defect detection capabilities, inspection limitations and new possibilities of shearography NDT for thick composites'. The study combines finite element methods (FEM) and experiment tests to investigate the defect detection capabilities of shearography for glass fibre reinforced polymer (GFRP) laminates of more than 50 mm thickness. In order to reliably simulate major defects in thick composites, flat bottom holes of different diameters and remaining thicknesses are manufactured in the test GFRP specimen. A thermal-mechanical model is established by computing equivalent thermal and mechanical properties. The established model is evaluated by experiments (surface strain by shearography, temperature by thermocouples). Both simulations and experiments show that shearography is a promising technique for thick composite inspection. In this chapter, the thresholds for defect-induced phase change and the corresponding defect-induced deformation are determined. The effect of mechanical boundary conditions on defect-induced deformation is studied by FEM. In addition, shearography NDT is benchmarked with ultrasonic testing for thick composite inspection.

45

4.1. INTRODUCTION

IN order to develop the novel shearography method with thermal excitations for thick composite inspection, the first step is to characterise the defect detection capabilities and inspection limitations of shearography for NDT of thick composites. So far, the efficacy of shearography for the inspection of composite structures of more than 50 mm thickness has not been fully characterised. Besides, in shearography NDT of thick composites, the influence of loading methods such as thermal loading, loading parameters of loading time and loading intensity and boundary conditions on defect behaviour and defect detection is not fully understood.

This chapter uses a numerical-experimental approach to investigate the defect detection capabilities of shearography for inspecting thick glass fibre reinforced polymer (GFRP) laminates. A thermal-mechanical model was established by computing equivalent thermal and mechanical properties and the model was evaluated by experiments. To reliably simulate major defects in thick composites, flat bottom holes were made following a common practice to represent a single delamination [2–4]. The specimen for this study is introduced in Section 4.2. Section 4.3 details the thermal-mechanical model of the thick GFRP laminate. This section also presents a method to characterise the heat flux from heating lamps with a thermocouple sensor. In Section 4.4, first the comparison of FEM and experimental results is conducted for model validation in Section 4.4.1. Based on the confined FEM models and shearography results, defect-induced deformation in the thick composite during cooling is studied in Section 4.4.2. Afterwards, the effect of mechanical boundary conditions on defect-induced deformation of the thick composite is analysed by FEM in Section 4.4.3. In addition, shearography NDT benchmark with ultrasonic testing for thick composite inspection is discussed in Section 4.4.4.

4.2. SPECIMEN FOR THIS STUDY

IN this study, one GFRP panel as shown in Figure 4.1 was used for characterising the defect detection capabilities of shearography for thick composite inspection. The size of the specimen is $600 \times 450 \times 51$ mm^3. The specimen surface (front) was sprayed with removable white matt paint for shearography inspection. This panel was milled with 13 flat bottom holes with three different diameters (D = 30, 60, 120 mm). These artificial defects are at different depths (Z) ranging from 5 to 40 mm. As mentioned in Section 3.2, the selection of layup, thickness of the material, defect size and depth are representative for marine composites. Here the depth of an artificial defect is defined as the remaining thickness of the material after drilling. Each defect is named by an alphanumerical code. For example, "D60-Z15" represents a defect that is 60 mm in diameter and 15 mm in depth. The material properties in different directions (e.g. Young's modulus, shear modulus, Poison's ratios, and thermal conductivities) can be found in Section 3.2.

4.3. NUMERICAL MODELLING

4.3.1. THERMAL–MECHANICAL MODEL FOR NDT CAPABILITY ANALYSIS

Figure 4.2 shows the thermal-mechanical model developed in ABAQUS to simulate the transient temperature and thermal deformation of the thick GFRP laminate with flat

bottom holes. For mechanical boundary condition in the FEM model, the displacement of the bottom surface along y-direction is constrained (UY=0 for bottom surface) as the specimen was freestanding on an optical table during measurement. As a thermal boundary condition, a small value of heat transfer coefficient (5 W/(m$^2 \cdot$K)) was adopted considering that the air flow in the lab is relatively small. The eight-node coupled temperature-displacement element (C3D8T) was selected for the finite element analysis since it is a 3D element and has thermo-mechanical capabilities. This C3D8T element measures displacements (e.g. displacements in x, y, z-axis, U1, U2, U3), strains (e.g. E11, E22), as well as the temperature of the whole model. The created finite element model consisted of about 700,000 elements and the total computational time was about 30 hours using a high performance computing cluster.
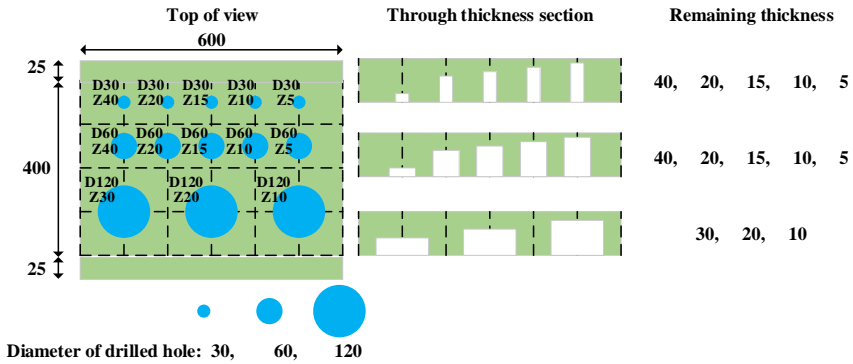
Figure 4.1: Diagram of the specimen with flat bottom holes. All dimentions are in mm.

In this research, the thermal deformation of the whole specimen during 180 s heating and 320 s cooling was simulated to assist in the shearography NDT investigation. It can be noted that the D60-Z15 is a defect that is of special interest for this study, so the heating and cooling times are selected mainly based on the efficacy of defect detection of D60-Z15, which is empirically determined from experiments (As seen later in Chapter 6, the selection of these heating and cooling times is actually reasonable considering the effect of thermal penetration depth).

(a) Front   (b) Back   (c) Mesh
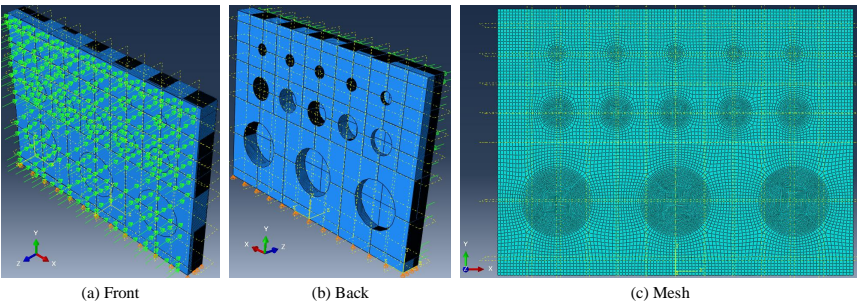
Figure 4.2: The 3D FEM model developed in Abaqus

4.3.2. CHARACTERISATION OF HEAT FLUX FROM HEATING LAMPS WITH A THERMOCOUPLE SENSOR

To simulate the transient temperature and thermal deformation of the test specimen, surface heat flux is needed as an Abaqus input of thermal loading. During the inspection, the specimen was heated from the front side by two halogen lamps. The front represents the specimen surface where the flat bottom holes are not visible. Due to limited direct measurement options, an indirect reconstruction of the surface heat flux was performed by solving an inverse problem from the thermal response (transient temperature) which was measured by a surface-mounted thermocouple (TC) sensor. Further in the model, an assumption of uniform heat distribution was made to simplify this problem.

For the transient temperature on the surface. Considering that the specimen is relatively thick (51 mm) and the thermal conductivity is relatively small(~ 0.36 W/(m·°C)), the surface temperature of the specimen (during the first couple of minutes of heating) can be represented by using the analytical solution of the semi-infinite solid with constant surface heat flux [5]:

$$T(t) = T_i + 2q_0 \left(\frac{t}{\pi \rho c_p k_z} \right)^{\frac{1}{2}} \tag{4.1}$$

where T_i is the initial temperature of the plate (around 20 °C, representing room temperature in the lab), q_0 is the heat flux at the front surface by the halogen lamps, and t is the time during heating. Since the transient temperature in time can be measured with the TC, and the material properties including density ρ, the specific heat c_p, and the thermal conductivity through thickness direction k_z are already known in Section 3.2, so the only unknown parameter is the heat flux q_0, which is assumed to be a constant due to the assumption of the uniform heat. The characterisation of the unknown value of heat flux q_0 is solved through a curve-fitting process. It is good to note that if an IR camera is used to replace thermocouples, the heat flux distribution over the specimen can be obtained by following the same procedure (this will be reported in Chapter 5).

The experimentally determined heat flux on the specimen surface is about 285 W/m^2. Figure 4.3(a) shows the transient temperature at the front surface of the central hole (D60-Z15) during heating. The experimentally measured temperature is the black solid line and the prediction by the analytic solution is the black dotted line. Their temperature difference is shown in Figure 4.3(b). As shown in Figure 4.3(b), the maximum difference in temperature is around 0.4 °C, which occurs at the beginning of the heating. Their temperature difference narrows down to 0.1 °C as the heating time increases from 30 s to 180 s. This indicates that the estimated heat flux matches the experimental data well.

It should be noted that in the experiment the thermal condition of uniform heating is satisfied approximately for the region near D60-Z15, while for the region far from D60-Z15 (e.g. the edge of the specimen), the actual surface heat flux may differ slightly from the estimated heat flux 285 W/m^2. Therefore, it is expected that the difference between experiments and simulations can increase from the region near to the central hole to the region close to the edge. For this study, the uniform heating condition is acceptable since the field of view (FOV) for shearography NDT is about 3/10 of the whole specimen, so the edge area is outside of the FOV, and from the perspective of validation of modelling, first the focus is more on the region near D60-Z15, which is done in the following section.
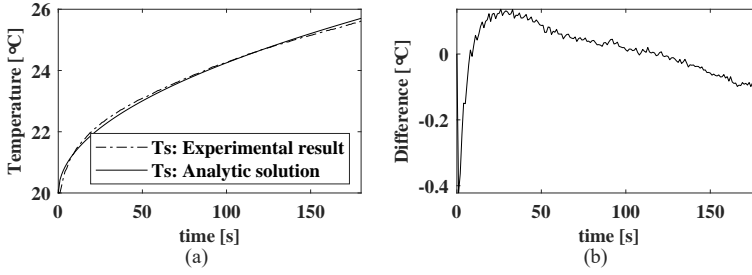
Figure 4.3: (a) Transient temperature measured with a TC and predicted by theory at the front surface of the central hole (D60-Z15). (b) The temperature difference between the experimental result and the analytical solution

4.4. Results and discussion

Now the full-scale, thermal-mechanical model has been established, it can be used to predict the deformation of the GFRP panel during heating and cooling, thus assisting in the analysis of defect detection capabilities in thick composites. In this section, first the FEM model was evaluated by comparing numerical results to experimental ones for transient temperature (T) and surface strain components ($\partial w/\partial x$). Then the defect-induced deformation (DID) during cooling was investigated by shearography and FEM. Afterwards, the influence of the mechanical boundary conditions on defect detection and DID was analysed by FEM. In addition, shearography NDT benchmark with ultrasonic testing is also discussed here.

4.4.1. Comparison between FEM and experiments

For model validation in temperature. Figure 4.4(a) shows the positions of four TCs which were glued to the specimen. Two of them were attached to points A1 and A2, measuring the temperature of the front and rear surfaces of D60-Z15, the other two were attached to points B1 and B2, measuring the temperature of the front and rear surfaces of the intact part. More TCs could give more information on the distribution of the temperature and heat flux, however, they may also affect the measurement of shearography. Therefore, the number of TCs is minimized to not interfere with shearography measurement.

For model validation in surface strain. Figure 4.4(b) shows the measurement area for the shearography tests. As a result of working conditions and instruments, a measurement of the full area of the specimen was not feasible. The FOV of the shearography camera is about 320×280 mm^2 of the specimen (area marked in red). As the shearing amount across the whole FOV may not be the same [6, 7], a calibration process [7, 8] for the shear amount δx was implemented to take into account the errors resulted from the shear variation across the specimen surface. The amount of shear was 5.58 mm (mean value). As introduced in Section 3.5, it was chosen by around 80% maximum output voltage of the piezo actuating system, which was a rational combination of the phase and the signals to be detected. The experimental description of the calibration process is available in Section 3.3.3. The calibrated area for shearography for strain analysis is about 250×185 mm^2 of the FOV (area marked in dotted black). In addition, the influence of the reference status (before or after heating) on shearography NDT was also studied here.
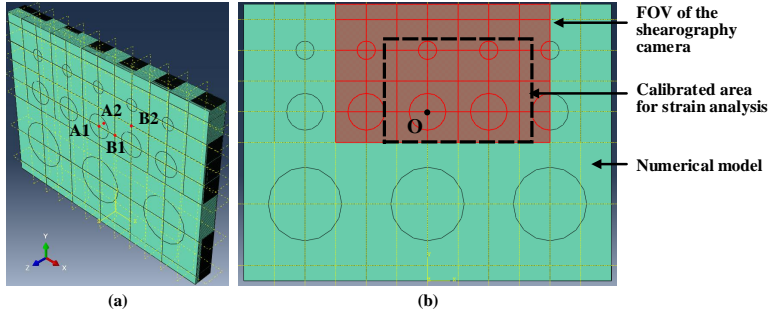
Figure 4.4: (a) Positions of thermocouples (TCs). (b) The measurement area for shearography tests

4

Figure 4.5(a) shows a comparison of transient temperature between experiments and simulations at points A1 and A2, respectively. The lamps were on from time 0 to 180 s and off from time 180 to 500 s. After turning the lamps off, the temperature of the front side decreased immediately while the temperature of the rear side still increased during cooling. Similar phenomenon can be found in Figure 4.5(b). The temperature increment at B2 (~ 0.1 °C) is much lower than that at A2 (~ 1.5 °C). This is because the thermal conductivity is relatively small and the thickness of the intact part (51 mm) is much larger than that of the central hole (15 mm), so it takes much more time for heat to reach B2. The transient temperatures between experimental measurements and FEM results agree with each other well. The differences in temperature between simulations and experiments at four positions are shown in Figures 4.5(c) and 4.5(d). A disturbance in temperature difference occurs in the initial stage of cooling. This is because in the experiment, it takes 2 s for the lamps to turn off completely. In this 2 s transition period, the heat flux from the lamps decreases rapidly to 0, while in the modelling, the heat flux is assumed to be zero right after heating, so a short pulse-like disturbance was induced in temperature difference.

Figure 4.6 shows strain maps at t = 180 s (right after heating) and t = 500 s (cooling for 320 s), respectively. The reference speckle images were captured before heating. The out-of-plane displacement derivative maps at 180 s and 500 s derived from FEM and shearography (DS), and their corresponding differences are given in Figures 4.6(a)-4.6(c) and 4.6(d)-4.6(f), respectively. As the modelling is a full-scale simulation while the calibrated area for shearography is 250×185 mm^2 of the simulated object, therefore only the displacement derivatives within the calibrated area were compared for shearography and FEM. The coordinate origin is at point O as shown in Figure 4.4(b), which is the central point of D60-Z15. For determining the accuracy of the thick composite model, the displacement gradients along axis a-a for simulations and experiments are compared, as shown in Figure 4.6(g). The difference of surface strain component along axis a-a by shearography and by modelling is shown in Figure 4.6(h). The modelling results agree well with the shearography results within the range from -30 mm to 130 mm (with a maximum difference of~ 20 $\mu\varepsilon$). The difference between shearography and FEM increases out of this range, mainly because it is difficult to achieve uniform heating over the whole surface of the specimen. The heat flux to the edge region can be smaller than the estimated value in the experiment.
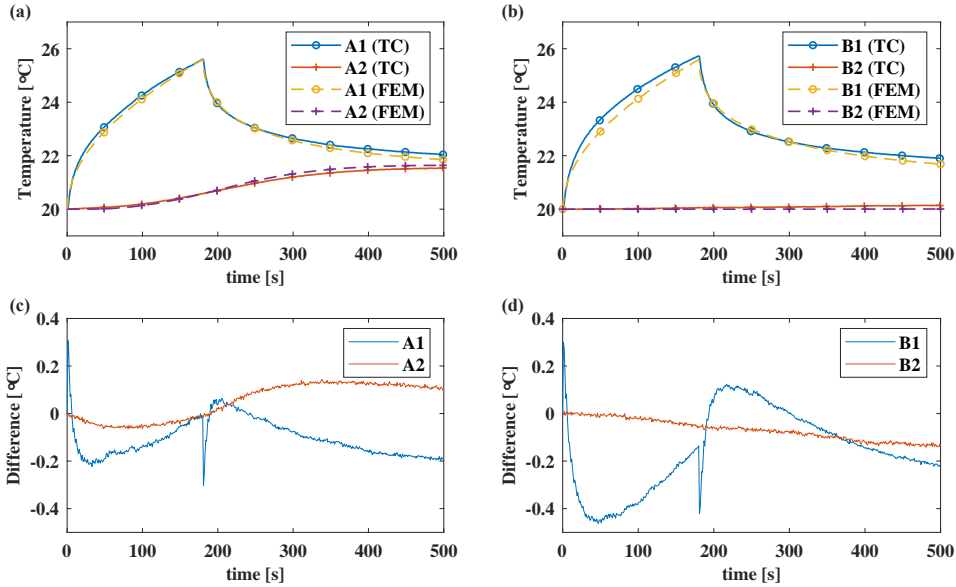
Figure 4.5: Comparison of transient temperature between experiments and simulations. (a) At the central hole (D60-Z15). (b) On a healthy part. (c) - (d): Differences in temperature between experiments and simulations at A1, A2, B1, B2, respectively.
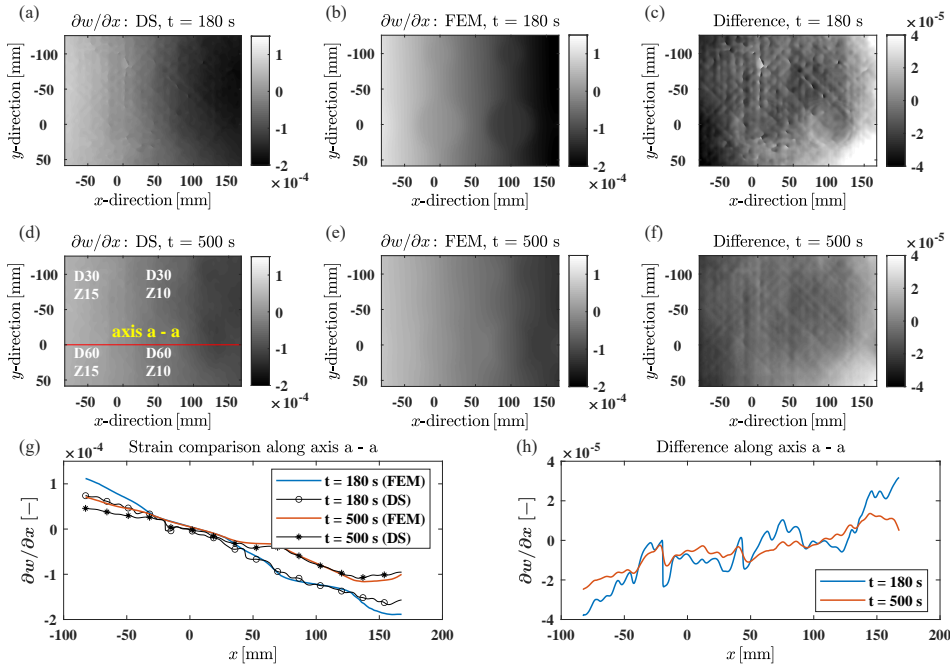
Figure 4.6: Comparison of surface strain components ($\partial w/\partial x$) by shearography (DS) and by FEM at 180 s and 500 s (reference status: before heating). (a) - (c) Shearography result, FEM prediction, and corresponding difference at 180 s. (d) - (f) Shearography result, FEM prediction, and corresponding difference at 500 s. (g) Strain comparison along axis a - a for the simulations and experiments. (h) Difference in strain along axis a – a for the simulations and experiments.

Figure 4.7 shows the out-of-plane displacement derivative maps at two cooling times by shearography (Figures 4.7(a) and 4.7(d)), by FEM (Figures 4.7(b) and 4.7(e)) and the corresponding difference ((Figures 4.7(c) and 4.7(f))). The reference speckle images were captured right after heating and the signal speckle images were captured after 69 and 320 s cooling, respectively. The cooling times were chosen from when defects become visually detectable. After 69 s cooling, two circular regions along axis $x = 100$ mm are shown in Figures 4.7(a) and 4.7(b). These two regions represent defects D30-Z10 and D60-Z10 at 10 mm depth. After 320 s cooling, two more defects (D30-Z15 and D60-Z15) at 15 mm depth are visible in Figures 4.7(d) and 4.7(e). The displacement derivative maps shown in Figure 4.7 represent overall deformation of the specimen, which contains defect-induced deformation.
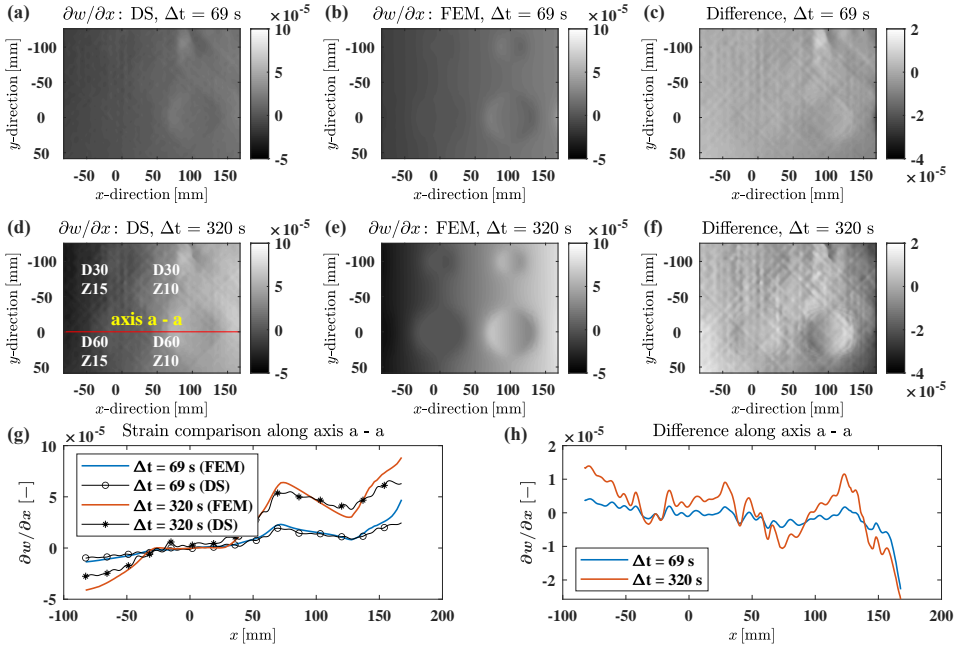
Figure 4.7: Comparison of surface strain components ($\partial w / \partial x$) at two cooling times by shearography and by FEM (reference status: after heating): (a) - (c) Shearography result, FEM prediction, and corresponding difference after 69 s cooling. (d) - (f) Shearography result, FEM prediction, and corresponding difference after 320 s cooling. (g) Strain comparison along axis a - a for the simulations and experiments. (h) Difference in strain along axis a – a for the simulations and experiments.

Figure 4.7(g) shows the comparison of the displacement derivative along axis a-a between experiments and simulations at the two cooling times. In general, the displacement derivative increases from $x = 50$ to $x = 150$ mm, and a fluctuation in displacement derivative happens when encountering a defect. In FEM, the fibre and the resin were homogenised per layer, and therefore the simulated thermal deformation (lines in blue and orange in Figure 4.7(g)) is smooth. While in experiments, it is shown that the displacement derivative curves measured with shearography (lines in black in Figure 4.7(g))

are with local variations. The variations are mainly due to the local fibre deformation, which can be considered as background noise.

Figure 4.7(h) shows the difference in the displacement derivative between experiments and simulations at two cooling times. The difference after 69s cooling is shown as the blue line, and the difference after 320s is shown as the orange line. There is a significant variation at some points (e.g. at the hole edge of D60-Z10). This is mainly due to the fibre-deformation related noise. As the simulated thermal deformation is ideal while the experimental result is with local variations, therefore the difference between FEM and experiment as shown in Figure 4.7(h) has variations from position to position. Besides, the manufacturing error when drilling holes in the thick composite can also contribute to the significant variations in Figure 4.7(h). It can be noted that the actual depth of the artificial defects (D60-Z10 and D60-Z15) is larger than the design values. Local variations in depth up to 1.5 mm were found which are not directly modelled. Therefore the defect signal measured by experiment is expected to be smaller than that predicted by FEM. Moreover, the mismatch in temperature between experiments and simulations can also be an issue. This mismatch is from the unknown heat transfer coefficient in experiments and the overestimated heat flux in FEM for the region far from the D60-Z15. The temperature difference between experiments and simulations increases with the cooling time (Figures 4.5(c) and 4.5(d)), which may explain why the difference in displacement derivative between experiment and FEM increases as cooling time increases from 69 to 320 s (Figures 4.7(g) and 4.7(h)).

Defects are more visible in Figure 4.7 than in Figure 4.6, which indicates that using a reference state after heating has a better performance in defect detection compared with a reference state before heating. This is because the background signal (overall deformation) in Figure 4.7 ($\sim 10^{-5}$) is much less than that in Figure 4.6 ($\sim 10^{-4}$). Therefore, in the following sections, reference states after heating are used for shearography NDT.

4.4.2. Defect-induced deformation

The key to a successful shearographic inspection lies in highlighting the contribution of defect-induced deformation (DID, representing defect signal) in the overall deformation (OD, representing background signal). Defect detection is expected to succeed as long as the defect signal is large enough for shearography to detect (e.g. the ratio of defect signal to background signal is greater than two). Moreover, it is possible to remove or reduce the background signal for detailed inspection by using phase compensation, i.e., subtracting a fitting surface that indicates overall deformation (Section 3.3.3).

Figure 4.8 shows the DID by experiment and by FEM, and the corresponding difference at two different cooling times (69 and 320 s, respectively). The two cooling times are the same as in Figure 4.7. Comparisons of DID along axis a-a at these two cooling times are shown in Figures 4.8(g) and 4.8(h). Two fluctuations are clear to see at $x = 0$ mm and $x = 100$ mm for both the experimental and the FEM results in Figure 4.8(h). These depict the DID of defects D60-Z15 and D60-Z10, respectively. The difference between experiments and simulations along axis a-a is given in Figure 4.8(i). The dotted line represents the difference between experiment and FEM after 69 s cooling, and the solid line represents the difference between experiment and FEM after 320 s cooling.

Lines at $\pm 45°$ and $90°$ are clearly shown in Figures 4.8(a) and 4.8(d) by experiment.
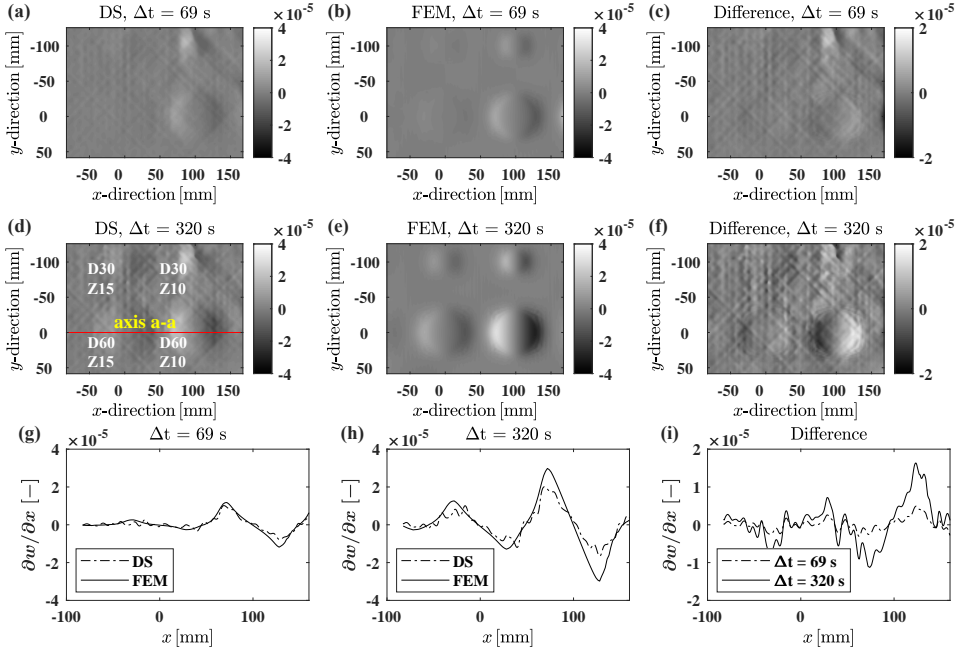
Figure 4.8: Comparison of DID by experiment and by FEM at two cooling times: (a) - (c) Shearography result, FEM prediction, and corresponding difference after 69 s cooling. (d) - (f) Shearography result, FEM prediction, and corresponding difference after 320 s cooling. (g) – (i) DID comparison and corresponding difference along axis a - a for the simulations and experiments.

Those lines represent fibre-related deformation, which are absent in Figures 4.8(b) and 4.8(e) by FEM since the effect of composite material composition on strain was not considered separately. Similar to Figures 4.7(g) and 4.7(h), there is a significant variation at some points (the edge of the D60-Z10), and the difference in displacement derivative between experiment and FEM increases as cooling time increases from 69s to 320s (Figures 4.8(g)-4.8(i)). The possible reasons include the fibre-deformation related noise (~ 23% error in strain) in experiments, the local variations in defect depth (~ 19% error in strain) due to the manufacturing error, and the mismatch in temperature (~ 10% error in temperature) from the unknown heat transfer coefficient and the overestimated heat flux, which have been discussed in detail in Section 4.4.1. Besides, the fitting process during phase compensation (Figure 3.5 in Section 3.3.3) may also introduce extra error that contributes to the significant variations, which is difficult to assess accurately. However, it is expected to be a minor issue.

The simulated phase maps and the corresponding simulated strain maps by FEM are ideal without considering fibre-related noise and errors from the shearography system (speckle decorrelation, phase error, intensity error, etc.). Therefore, the background signal in a healthy region by FEM is much less than that by shearography. For our experiments, the standard deviation (STD) of the background phase signals in the healthy region by simulation and by experiment is approximately 0.02 rad and 0.2 rad, respectively.

Practically in the shearography experiments, a phase measurement sensitivity of $\frac{2\pi}{10}$ rad [9] is possible to achieve, which is about three times the STD of the background phase signals in the healthy region in the experiment. Therefore in this chapter, the thresholds for defect-induced phase (DIP) change are set to be $\pm\frac{2\pi}{10}$ and $\pm\frac{2\pi}{5}$:

$\delta\phi_{DIP} \in \left[\infty, -\frac{2\pi}{5}\right] \cup \left[\frac{2\pi}{5}, \infty\right]$, the defect detection is most likely to succeed.

$\delta\phi_{DIP} \in \left(-\frac{2\pi}{5}, -\frac{2\pi}{10}\right) \cup \left(\frac{2\pi}{10}, \frac{2\pi}{5}\right)$, the defect detection may succeed.

$\delta\phi_{DIP} \in \left[-\frac{2\pi}{10}, \frac{2\pi}{10}\right]$, the defect detection most likely will not to succeed.

Combining with Eq. 3.4 in Section 3.3.1, the corresponding thresholds for DID can therefore be derived and the required cooling time can be estimated for reliable defect detection. As the laser wavelength is 532 nm (green laser), and the mean value of the shear amount δx over the calibration area is about 5.58 mm, the corresponding thresholds for defect-induced deformation $\frac{\partial w}{\partial x}_{DID}$ are ± 4.8 and ± 9.5 $\mu\varepsilon$.

The DID during cooling along the axis a-a of the full model is shown in Figure 4.9. For the heating scenario (heating from $t = 0$ to 180 s, cooling from $t = 180$ to 500 s) in this chapter, the detectable depth is 15 mm, and the estimated cooling time for detecting the defect at 15 mm depth is around 250 s. Deeper defects may require more heating flux and/or more cooling time to be detected. The follow-up experimental results show that the defect at 20 mm depth (D60-Z20) can be detected successfully with a heat flux of more than 1000 W/m^2. However, the detection of defects at 40 mm depth has not succeeded yet after testing various combinations of heat fluxes and heating times.
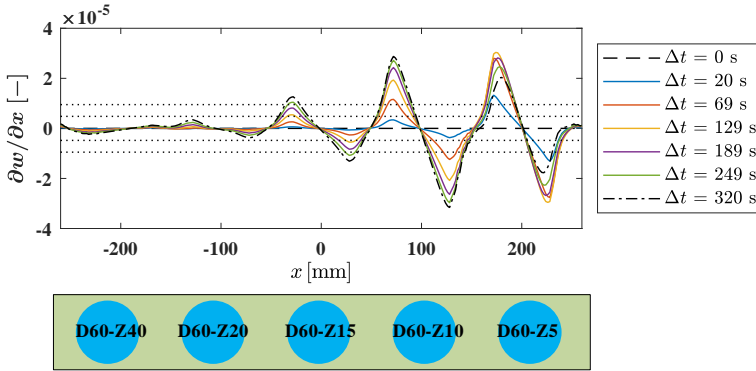
Figure 4.9: DID along axis a-a during cooling by FEM, the thresholds for DID marked in dotted lines.

4.4.3. EFFECT OF MECHANICAL BOUNDARY CONDITIONS

Although it is possible to experimentally study the effects of various mechanical boundary conditions on thick composite inspection, nevertheless, for the GFRP panel under investigation in this chapter, an ideal mechanical boundary condition (physically in the laboratory) such as fully clamped (CCCC) or simply supported-horizontal (UZ=0) would be difficult to achieve. This is because of the relatively large panel size (600×450 mm^2) and its significant thickness (~50 mm). Therefore an experimental study of the effects of mechanical boundary conditions for this GFRP panel is challenging. With the numerical

and experimental results reported in Sections 4.4.1 and 4.4.2, it is safe to say that the FEM model is reliable (the maximum strain difference between simulations and experiments over the calibrated area during cooling is around 20 $\mu\varepsilon$). Since the simulations showed reasonable accuracy compared with shearography experiments, it was possible to study the effect of mechanical boundary conditions on DID by FEM. For this purpose, three mechanical boundary conditions are studied in this section, which are the freestanding case (UY = 0 for bottom surface, previously studied in Section 4.4.1), the fully clamped case (CCCC), and the simply supported-horizontal case (UZ = 0 for back surface), as shown in Figure 4.10. The specimen is heated and inspected from the front surface, which is the defect-free side. The surface heat flux, the heating and the cooling times are set the same as in Section 4.4.1. The heat loss from the composite to the environment is also the same (as in Section 4.4.1). Hence, the temperature distributions in the composite for all three cases are the same, and the mechanical boundary condition is the only variable.

(a)   (b)   (c)
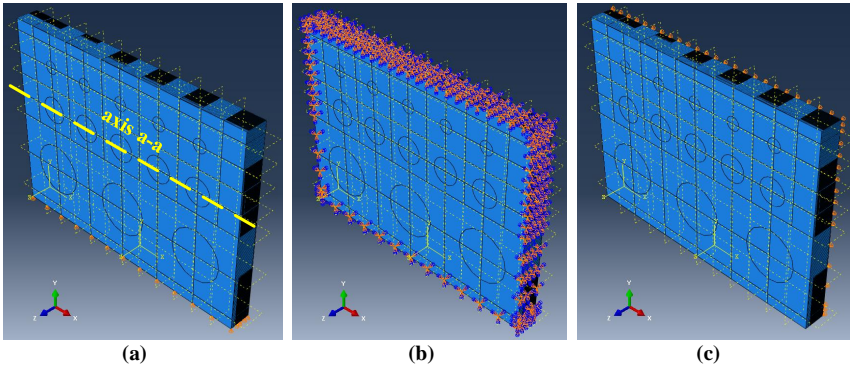
Figure 4.10: Three mechanical boundary conditions for modelling. (a) Freestanding (UY = 0). (b) Fully clamped (CCCC). (c) Simply supported-horizontal (UZ = 0).

Figure 4.11 shows the comparison of the three mechanical boundary conditions on DID after cooling for 320 s. The reference images were captured after 180 s heating. As shown in Figures 4.11(a)–4.11(c), shearographic fringes were simulated for a direct comparison of the three boundary conditions with the same shear distance of 5.58 mm. It shows that the simulated fringes highly depend on boundary conditions. For the freestanding case, the influence of whole body bending on the fringes is dominant, while for the fully clamped case and the simply supported-horizontal case, the magnitude of the body bending is much smaller compared with the freestanding case. Therefore, the defect-induced anomalies are more visible from the fringe patterns for the fully clamped case and the simply supported-horizontal case than for the freestanding case. The DID maps for the three boundary conditions are shown in Figures 4.11(d) – 4.11(f) and the comparison along axis a-a is given in Figure 4.11(g). It shows that during cooling, the effect of boundary conditions on the DID at a large depth (more than 10 mm) is limited. The relative DID values of the three boundary conditions are close to each other. While for defects at 5 and 10 mm depth, there is a relatively big difference in DID among the three boundary conditions, which could be the effect of local stiffness.

Figure 4.12 shows the DID of defects with the diameter of 60 mm at 5, 10, 15, 20

mm depth for three boundary conditions during cooling, the selected points are around the edge of the defect. When the depth of the defect is increased from 5 to 20 mm, the difference in the defect-induced strain among the three boundary conditions decreases from 11.9 to 1.7 $\mu\varepsilon$, which indicates that as defect depth increases, the influence of mechanical boundary conditions on DID decreases.
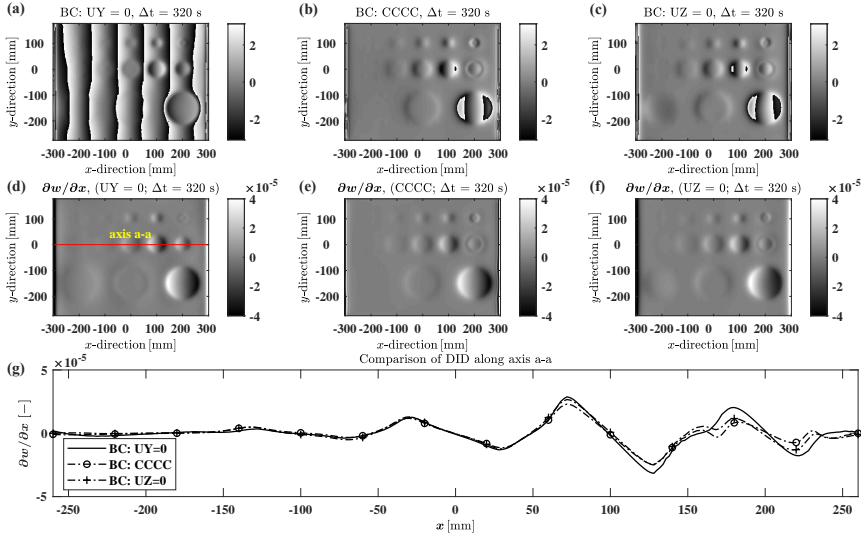
Figure 4.11: Comparison of boundary conditions on DID after 320 s cooling by FEM. (a) - (c) Simulated fringes for freestanding (UY=0), full-clamped (CCCC), and simply supported-horizontal (UZ=0), respectively. (d) - (f) DID for freestanding (UY=0), full-clamped (CCCC), and simply supported horizontal (UZ=0), respectively. (g) Comparison of DID along axis a-a.
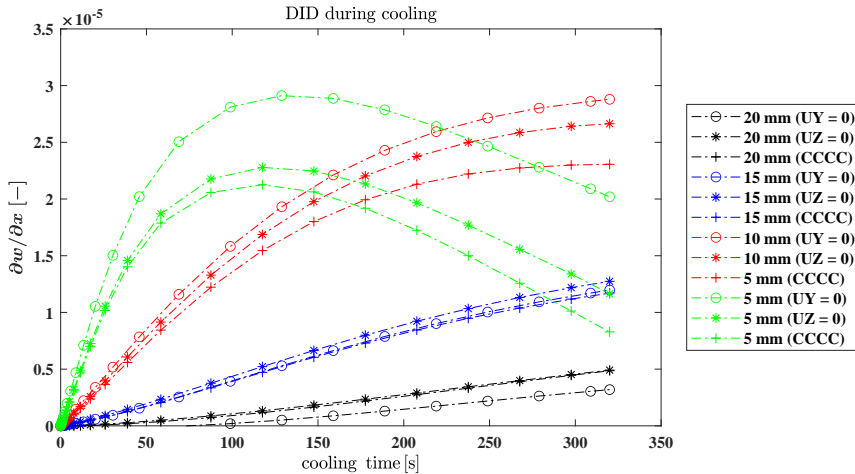
Figure 4.12: DID of defects with the diameter of 60 mm at 5, 10, 15, 20 mm depth during cooling by FEM.

4.4.4. SHEAROGRAPHY NDT BENCHMARK WITH ULTRASONIC TESTING

Figure 4.13 shows shearography inspection results compared with phased-array ultrasonic testing ones. For shearography with current heating sources, defects at 40 mm depth are not detectable as seen from Figures 4.13(a) and 4.13(b); while phased-array UT with a 0.5 MHz probe has superior performance, it can detect all the defects in the GFRP panel including the ones at 40 mm depth. In these conditions, a smooth surface is required for good surface coupling. Still, shearography offers non-contact and full-field measurements; while for UT, contact scanning is needed and adequate surface roughness is preferable. In the marine sector, the surface roughness of the test structure is usually worse for UT, thus affecting its performance significantly (Chapter 7).
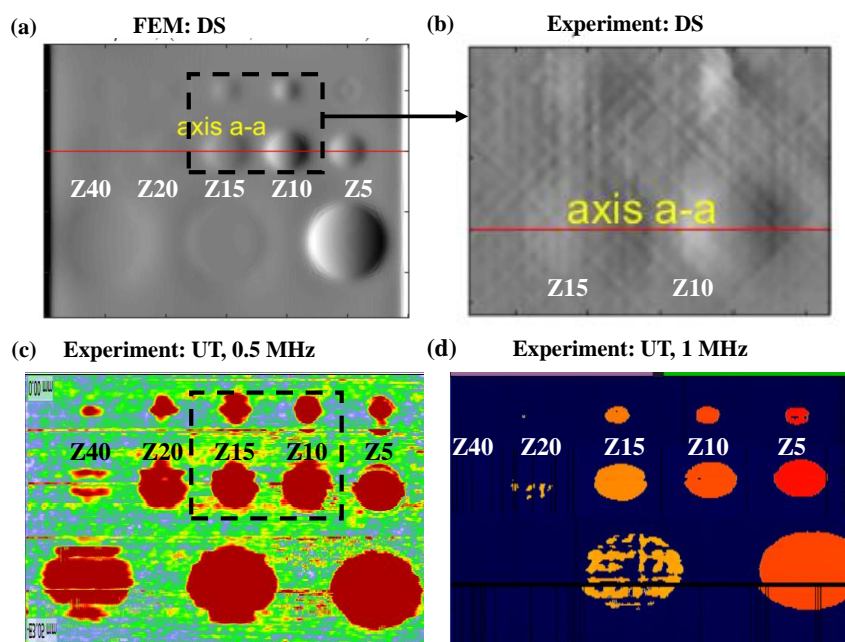
Figure 4.13: Shearography results (DS) compared with ultrasonic testing (UT): (a) DS result for the full panel from FEM. (b) DS result for the dotted black area from experiment. (c) Phased-Array UT result using 0.5 MHz probe. (d) Phased-Array UT result using 1.0 MHz probe

4.5. CONCLUSIONS

IN this chapter, RQ1 is fully answered. A numerical-experimental study has been conducted to investigate the defect detection capabilities of shearography NDT for a 51 mm thick GFRP laminate with flat bottom holes. First a thermal-mechanical model for detecting defects in the thick composite was developed using equivalent mechanical and thermal properties. The model was then evaluated by TCs and shearography tests. It shows a good agreement in transient temperature and in strain maps between simulations and experiments. Based on the FEM and experimental results, the detectable

depth of shearography for this thick GFRP laminate can be up to 20 mm with the current heating sources. The thresholds for the defect-induced phase and the corresponding defect-induced deformation were determined for shearography testing. It can be noted that the maximum detectable depth of shearography in fibre-reinforced composite laminates that can be found in literature is less than 10 mm [2, 10, 11]. Moreover, to the best of our knowledge, the defect detection capability of shearography in thick fibre-reinforced composite laminates (with the thickness of more than 50 mm) has not been reported yet.

The effect of mechanical boundary conditions on DID was also studied. Current modelling results indicate that mechanical boundary conditions have a significant influence on shearography fringe patterns. As for defect-induced deformation during cooling, the influence of boundary conditions for deep defects is limited, which may indicate that for thick composite inspection, the influence of mechanical boundary conditions on defect detection capabilities of shearography is limited in the case that the overall deformation can be removed properly. A shearography NDT benchmarking with ultrasonic testing is also discussed in this chapter, providing insight for future inspection of large-scale ship structures in the marine environment (e.g., in a shipyard).

REFERENCES

[1] N. Tao, A. G. Anisimov, and R. M. Groves, *Shearography non-destructive testing of thick GFRP laminates: Numerical and experimental study on defect detection with thermal loading,* Composite Structures **282**, 115008 (2022).

[2] G. De Angelis, M. Meo, D. Almond, S. Pickering, and S. Angioni, *A new technique to detect defect size and depth in composite structures using digital shearography and unconstrained optimization,* NDT & E International **45**, 91 (2012).

[3] Z. Liu, J. Gao, H. Xie, and P. Wallace, *NDT capability of digital shearography for different materials,* Optics and Lasers in Engineering **49**, 1462 (2011).

[4] D. Akbari, N. Soltani, and M. Farahani, *Numerical and experimental investigation of defect detection in polymer materials by means of digital shearography with thermal loading,* Proceedings of the Institution of Mechanical Engineers, Part B: Journal of Engineering Manufacture **227**, 430 (2013).

[5] T. L. Bergman, F. P. Incropera, D. P. Dewitt, and A. S. Lavine, *Fundamentals of heat and mass transfer* (John Wiley & Sons, 2017).

[6] D. T. Goto and R. M. Groves, *Error analysis of 3D shearography using finite-element modelling,* in *Optical Micro- and Nanometrology III*, Vol. 7718, edited by C. Gorecki, A. K. Asundi, and W. Osten, International Society for Optics and Photonics (SPIE, 2010) p. 771816.

[7] A. G. Anisimov, M. G. Serikova, and R. M. Groves, *3D shape shearography technique for surface strain measurement of free-form objects,* Applied Optics **58**, 498 (2019).

[8] A. G. Anisimov, B. Müller, J. Sinke, and R. M. Groves, *Analysis of thermal strains and stresses in heated fibre metal laminates,* Strain **54**, e12260 (2018).

[9] L. Yang and X. Xie, *Digital shearography: new developments and applications* (SPIE press, 2016).

[10] E. Greene, *Inspection techniques for marine composite construction and NDE,* Report No SSC-463, United States Ship Structure Committee, Washington, DC (2012).

[11] H. Shang, F. Chau, C. Tay, and S. Toh, *Estimating the depth and width of arbitrarily-oriented disbonds in laminates using shearography,* Journal of Nondestructive Evaluation **9**, 19 (1990).

4

5

SPATIALLY MODULATED HEATING FOR SHEAROGRAPHY NDT

This chapter aims at improving the detection of deep defects in thick composites with shearography. Instead of using conventional global heating (GH), the core idea is to apply novel spatially modulated heating (SMH) for shearography NDT, which addresses RQ2 - 'How can spatially modulated heating be developed for improving thick composite inspection with shearography'. In this chapter, the finite element method (FEM) has been used to advance shearography towards a quantitative inspection technique for thick composites. Both GH and SMH have been performed experimentally and modelled in Abaqus to evaluate the corresponding efficacy in the detection of deep defects. SMH is achieved by using a halogen lamp with a Fresnel lens. The heat flux distribution on the specimen surface is taken into consideration for defect detection, a factor which is rarely reported in shearography inspection. Besides, the influence of different reference states on shearography NDT of deep defects is studied by looking into the defect-induced phase maps from shearography. The results indicate that the proposed SMH can improve deep defect detection with shearography in thick composites by 2 to 3 times that of GH. It should be addressed that a similar and defect-free reference sample is currently necessary to compare with the sample under test.

5.1. INTRODUCTION

IT is already evident from the previous sections, namely Sections 2.3.3 and 3.1, that the loading method plays a critical role in enabling the success of shearography in defect detection. The development of shearography methods for NDT has therefore essentially become the development of loading methods that can reveal defects [2–4].

In most of the studies of shearography NDT with thermal loading, global heating is applied to deform the object [5–7]. The distribution of heat flux over the surface of the test object is rarely taken into consideration during the shearography inspection. In literature, the finite element method (FEM) was used to assist in shearography NDT of thin materials, which enabled the prediction of thermal deformation during the inspection. In some cases, thermal loading was simulated by applying a temperature in the model for the NDT of isotropic materials [6, 7]. More recently, constant heat flux was used as an input of thermal loading for the inspection of an anisotropic wooden panel [8] as well as a CFRP plate [9], where heating was assumed to be uniform or locally uniform. However, in reality, the heat flux on the specimen surface can vary with location, which may affect defect detection. Moreover, for shearography NDT of thick composites, especially when detecting deeply buried defects (e.g. defect depth of 15-25 mm and more), the performance of conventional global heating may be less desirable. This is because of the limitations of rapid heat dissipation with increased thickness and the difficulties of heating large-scale structures uniformly. Therefore, a modulated heating process can be necessary in order to improve deep defect detection.

The study presented in Chapter 4 has broadened the application of shearography with thermal loading to composites with thicknesses up to 50-60 mm [10], where the artificial defects of 5 to 20 mm in depth can be detected in a 51 mm thick marine GFRP laminate. Nevertheless, the detection of deep defects (e.g., at 25 mm depth) was not studied in detail and the heat flux was assumed to be uniform in the modelling.

This chapter aims at improving the detection of deeply buried defects in thick composite laminates. For that, FEM-assisted shearography with spatially modulated heating (SMH) and global heating (GH) have been conducted and investigated. A flat-bottom hole is used, following a common practice [6, 11, 12], to indicate the major defect in a 51 mm thick GFRP laminate. Section 5.2 introduces the test GFRP panel and the experimental shearography system for this study. Section 5.3 presents the FEM model for predicting the thermal-mechanical response of the thick GFRP laminate during the inspection. Results and discussion are presented in Section 5.4. First in Section 5.4.1, the model is validated by comparing experimental and numerical results of the test GFRP panel subjected to GH and SMH, respectively. Afterward in Section 5.4.2, defect-induced responses subjected to these thermal excitations are presented. The selection of the reference status on shearography NDT of the deep defect is analysed in Section 5.4.3. The discussions on the developed SMH are given in Section 5.4.4.

5.2. SPECIMEN DESCRIPTION AND SHEAROGRAPHY SYSTEM

5.2.1. SPECIMEN FOR DEEP DEFECT DETECTION

As shown in Figure 5.1, a 300 × 300 mm^2 GFRP specimen was made of the same laminate as in Chapter 4 with a flat bottom hole was made for the purpose of deep defect detection.

The front surface of the specimen (Figure 5.1(a)) was sprayed with removable white matt paint. The flat-bottom hole was made from the back surface of the specimen (Figure 5.1(b)) to simulate the major defect in the thick composite. The diameter and the remaining thickness of the hole are 60 and 25 mm, respectively, indicating that the artificial defect is 60 mm in size (D) and at 25 mm depth (Z). It should be noted that the defect size and depth are representative for deeply buried defects in marine composites. The material properties in different directions (e.g. Young's modulus, shear modulus, Poison's ratios, and thermal conductivities) can be found in Section 3.2.
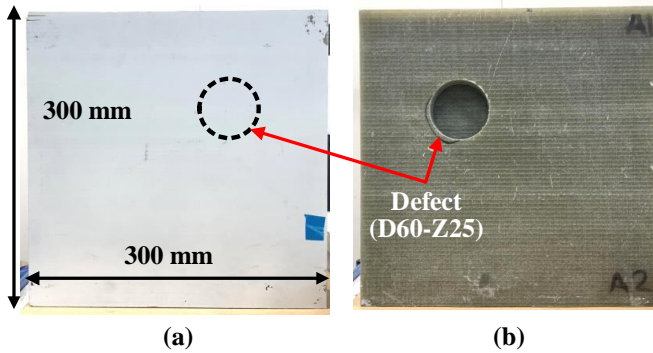
Figure 5.1: The test GFRP specimen for deep defect detection: (a) Front view. (b) Back view.

5.2.2. EXPERIMENTAL SHEAROGRAPHY SYSTEM INCORPORATED WITH IR CAMERA

The out-of-plane (i.e., $\partial w/\partial x$) shearography system with built-in FLIR A655 infrared (IR) camera is shown in Figure 5.2. The specimen was placed at a distance of about 1 m from the shearography instrument. Three halogen lamps operating at 500 W of electrical power each were used to apply thermal loading to the specimen. For the GH mode, two symmetrically placed lamps (lamps 1 and 2, Figure 5.2(a)) were at a distance of about 1 m from the test piece to heat it globally. The distance between the two lamps was about 0.8 m. For the SMH mode, only the third lamp (lamp 3, Figure 5.2(b)) with a Fresnel lens (#32 − 685 by Edmund Optics) was used to modulate the distribution profile of the heating on the object surface. The dimensions of the Fresnel lens are 170×170 mm^2 and its effective focal length is 254 mm. The operating temperature of the Fresnel lens is up to 80 °C with a transmission of 92% (from 400-1100 nm). This Fresnel lens was used because of its lightweight and good performance of light gathering. The distance between lamp 3 and the specimen was about 0.6 m. It can be noted that by adjusting the angles of the lamps and the position of the Fresnel lens, the uniformity of heat distribution was controlled, and then monitored by the IR camera (640×480 pixels, thermal resolution down to <30 mK at temperatures measured as introduced in Section 3.3.1). In this study, due to the illumination setup with the Fresnel lens and heating at an angle, the shape of the SMH was elliptical (Figure 5.4(d)). The measured transient temperature with the IR camera was further used for estimating the heat flux distribution on the specimen surface as an input for simulating thermal loading in Abaqus. The related results will be discussed

later in Section 3.3.1.

The five-step phase-shifting algorithm was selected due to its resulting accuracy [13]. The shear distance δx was calibrated over the field of view (FOV) according to [14, 15] and was found to be 7.8 ± 0.5 mm (mean ± std). The shear distance was experimentally determined due to phase fringe density and sensitivity for defect detection.
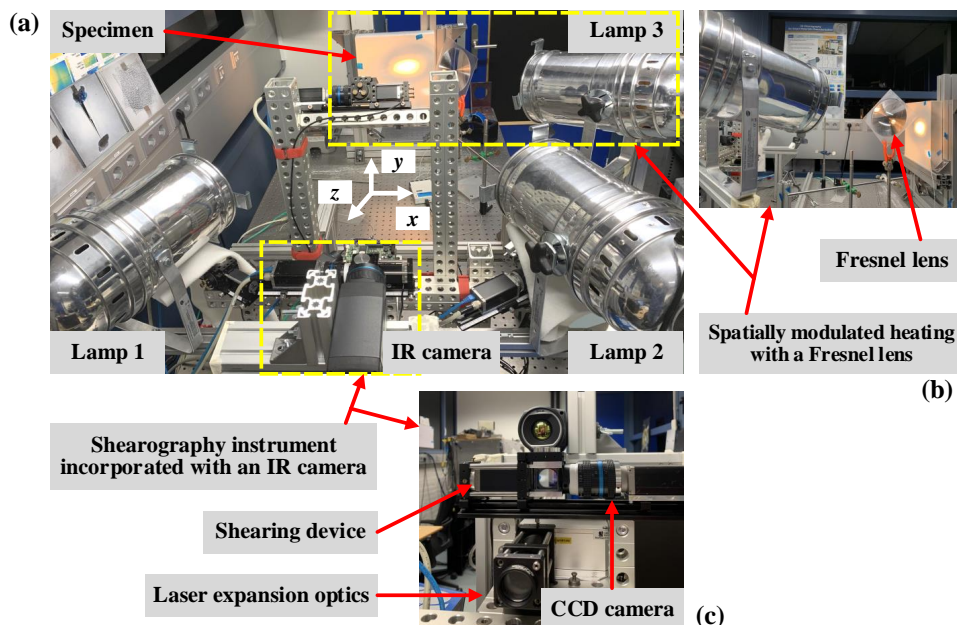
Figure 5.2: Experimental out-of-plane shearography system for thick composite inspection: (a) an overview of the shearography instrument with conventional global heating (lamps 1, 2) and spatially modulated heating (lamp 3), (b) spatially modulated heating with a Fresnel lens, (c) shearography instrument incorporated with the IR camera.

5.3. NUMERICAL MODELLING

FEM has been used to model both global heating and spatially modulated heating as the inputs of thermal loading with Abaqus. The equivalent thermal and mechanical properties of the test GFRP laminate for modelling can be found in Section 3.2. In this section, the thick composite laminate model and the characterisation of heat flux distributions of global heating and spatially modulated heating with the IR camera are reported.

5.3.1. THERMAL-MECHANICAL MODEL

The front and the back views of the 3D model geometry are shown in Figures 5.3(a) and 5.3(b), respectively. As the test specimen was freestanding on an optical table during measurements for both global heating and spatially modulated heating, the displacement along the y-axis on the bottom surface was fixed to simulate the freestanding boundary

condition (Figure 5.3(a)). As the airflow in the lab is relatively slow, a small value of heat transfer coefficient (2 W/(m$^2 \cdot$K)) was selected for the model to simulate thermal boundary conditions between the thick composite and the environment. The C3D8RT element [16, 17] was selected for the FEM model because of its advantages of saving computational time and its capabilities in coupled temperature-displacement analysis. The outputs include temperature and displacement. The MATLAB code that was developed in Chapter 4 was adopted to calculate simulated phase maps for comparison. The experimentally-determined shear distance over the specimen surface was calibrated and implemented to obtain more accurate simulated phase maps. In this chapter, the phase is chosen as a unit for comparison because it is the primary output from the shearography experiments.
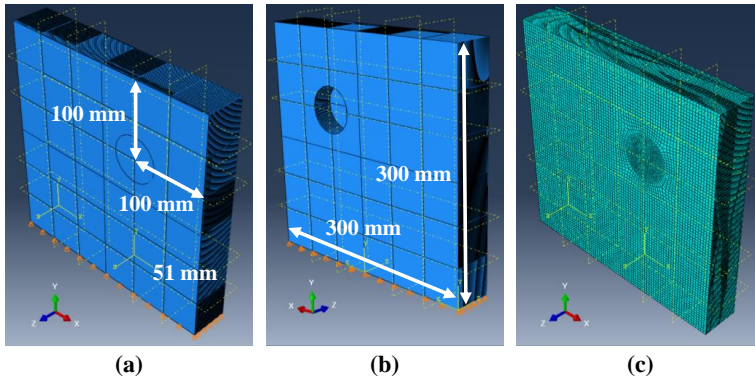
Figure 5.3: The established 3D FEM model in Abaqus: (a) front view, (b) back view, (c) mesh.

5.3.2. CHARACTERISATION OF HEAT FLUX DISTRIBUTIONS OF GH AND SMH WITH IR CAMERA

The specifics of thermal loadings are given here. The test panel was heated from the front (defect-free side) by the halogen lamp(s). The heating scenario (Figure 5.4(a)) was chosen as 10 cycles of 60 s heating and 7 s cooling, followed by a cooling duration of 900 s, as preliminary analysis showed this gave a thermal penetration depth of about 25 mm (defect depth). The heating cycle was experimentally determined to get resolvable phase maps taken between the cycles. The transient temperature at the back of the hole center was measured with a thermocouple (TC) and the temperature rise was found to be several degrees Celsius. The related results will be reported later in Section 5.4.1.

In this chapter, cyclic heating was selected over continuous heating to prevent overheating of the lamps. These gaps in the heating also allowed intermediate speckle interferograms to be captured without overexposing the camera with the light of the lamps. These intermediate measurements were used later to evaluate various reference states (Figure 5.4(a)) on defect detection in Section 5.4.2. Global heating and spatially modulated heating (Figure 5.4(b)) were simulated in Abaqus as well as were applied to the specimen in experiments for analysis and comparison. The transient temperature on the specimen surface that was measured with the IR camera was further used to characterise
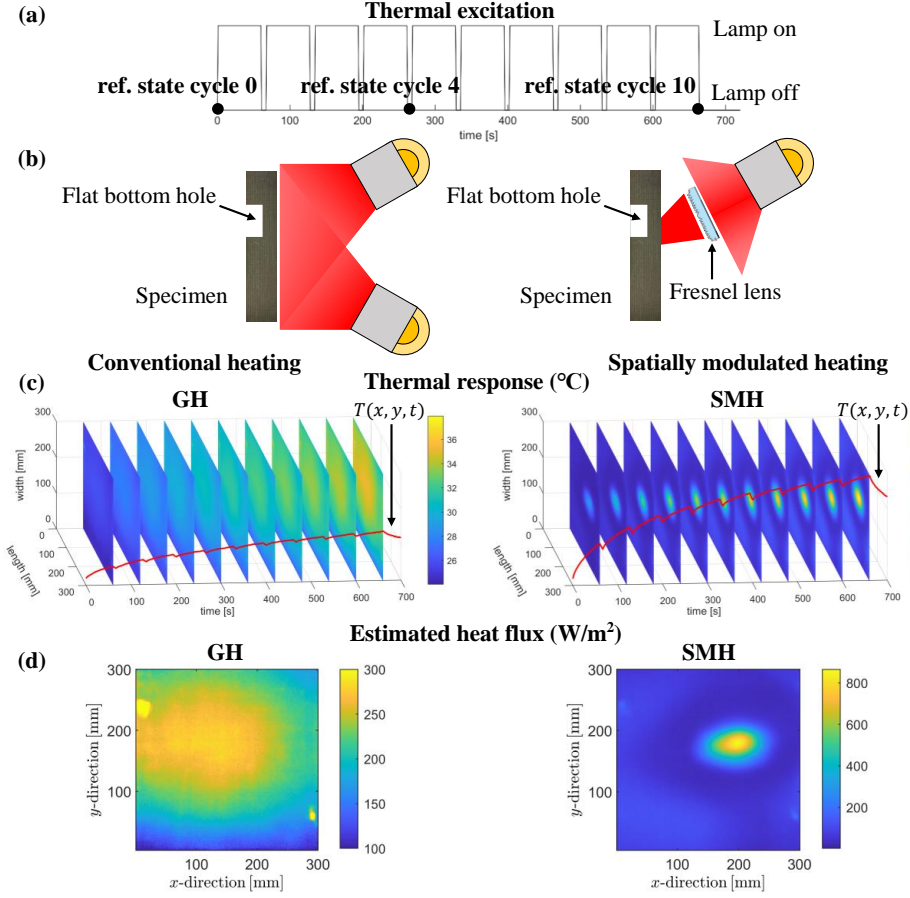
Figure 5.4: Diagram of conventional global heating and spatially modulated heating as the Abaqus inputs of thermal loading: (a) thermal excitation, (b) diagram of conventional global heating and spatially modulated heating, (c) thermal response measured with the IR camera, (d) experimentally-determined heat flux for global heating and spatially modulated heating.

full-field heat flux distribution as the input of thermal loading in Abaqus.

It is assumed that the heat flux of each heating cycle is the same as the positions and angles of the lamps are fixed. So the transient temperature of the first heating cycle (Figure 5.4(c)) was used for estimating the heat flux distribution on the specimen surface. For heat conduction in a thick composite laminate, the transient temperature $T_1(x, y, t)$ (for a short period) at each pixel (x, y) in the IR camera can be represented by the analytical solution of the semi-infinite solid with surface heat flux [18]:

$$T_1(x, y, t) = T_i + 2q(x, y)\left(\frac{t}{\pi \rho c_p k_z}\right)^{\frac{1}{2}} \tag{5.1}$$

where T_i is the initial temperature of the plate (20 °C, representing room temperature in

the lab), $q(x, y)$ is the heat flux at a point on the surface which corresponds to pixel (x, y) by the halogen lamp(s), t is the heating time of the first cycle, ρ is the density of the plate, c_p is the specific heat and k_z is the thermal conductivity in the through-thickness direction. The heat flux $q(x, y)$ can therefore be estimated by a curve-fitting process as shown in Section 4.3.2. With a loop to characterise heat flux pixel-by-pixel, the heat flux distribution over the specimen can be obtained. The estimated heat flux distributions by global heating and by spatially modulated heating are shown in Figure 5.4(d). It can be seen that global heating was characterised as uniform heating with the variation of heat flux from 285 W/m^2 at the center to around 123 W/m^2 at the corner. The calculated uniformity of global heating is about 60%. Besides, as shown in Figure 5.4(d), the heat is more concentrated for spatially modulated heating than for global heating. The maximum heat flux from spatially modulated heating is 3 to 4 times as large as that from global heating, while the average heat flux is about 40% of that from global heating. Because of this, it is expected that higher local deformations can be detected with spatially modulated heating. When the heating location of the region where energy is concentrated is close to the defect edge, it is expected that a strong defect signal will be obtained, which can therefore improve defect detection. It should be addressed that Eq. 5.1 is a simplified solution without considering 3D heat transfer within the thick composite and heat transfer between the composite and environment, resulting in undervalued heat flux. In order to overcome this issue, a magnitude factor was introduced to modify the calculated heat flux distribution and the factor was estimated to be about 1.35 for this study.

5.4. RESULTS AND DISCUSSION

IN this section, experimental and numerical results for shearography NDT of the deep defect are presented. First, a comparison between the experimental results and the numerical ones of the test GFRP panel (Figures 5.1 and 5.3) for transient temperature and phase maps are reported in Section 5.4.1. Then the defect-induced responses subjected to GH and SMH are presented in Section 5.4.2. The impact of the reference status on shearography NDT of thick composites is discussed in Section 5.4.3. In experiments, it can be noted that the sets of phase-shifted speckle interferograms were recorded continuously with the shearography instrument. All these sets were processed and built up, generating the phase map that reveals the development of the out-of-plane displacement gradient (i.e., $\partial w / \partial x$) over the inspection time. The phase unit is radian, and in this instrument-specimen geometry (Figure 5.2), 1 rad corresponds to about 5.4 $\mu\varepsilon$.

5.4.1. COMPARISON IN TEMPERATURE AND PHASE BETWEEN EXPERIMENTS AND SIMULATIONS

This section first describes the model validation for temperature changes using experimental results. Figures 5.5(a) and 5.5(b) are 2D plots of transient temperature for GH (right after the 10th cycle of heating) measured with the IR camera and predicted by FEM, respectively. The corresponding difference is shown in Figure 5.5(c). Figures 5.5(d)-5.5(f) are 2D plots of transient temperature for SMH measured with the IR camera, predicted by FEM, and the corresponding difference, respectively, the time instant is right after the 10th cycle of heating as well. It can be noted that the initial temperature of the specimen

before heating was around 20 °C, which has been subtracted from the data in the figure. The maximum temperature increase by SMH (~ 30 °C) is about 2.5 times as large as that by GH (~ 12 °C). The difference between experiments and simulations is ±1.0 °C for GH and ±1.5 °C for SMH, respectively. This comparison shows a good agreement in transient temperature between the experimental results and the FEM ones. For GH, the temperature is about 10.2±1.9 °C (mean±std), while for SMH, the temperature is more focused due to the more concentrated heat flux. Figures 5.5(g) and 5.5(h) show the transient temperature at the front and the back of the hole center over time for GH and SMH, respectively. The solid lines indicate transient temperatures from experiments, and the dotted lines indicate those from simulations.
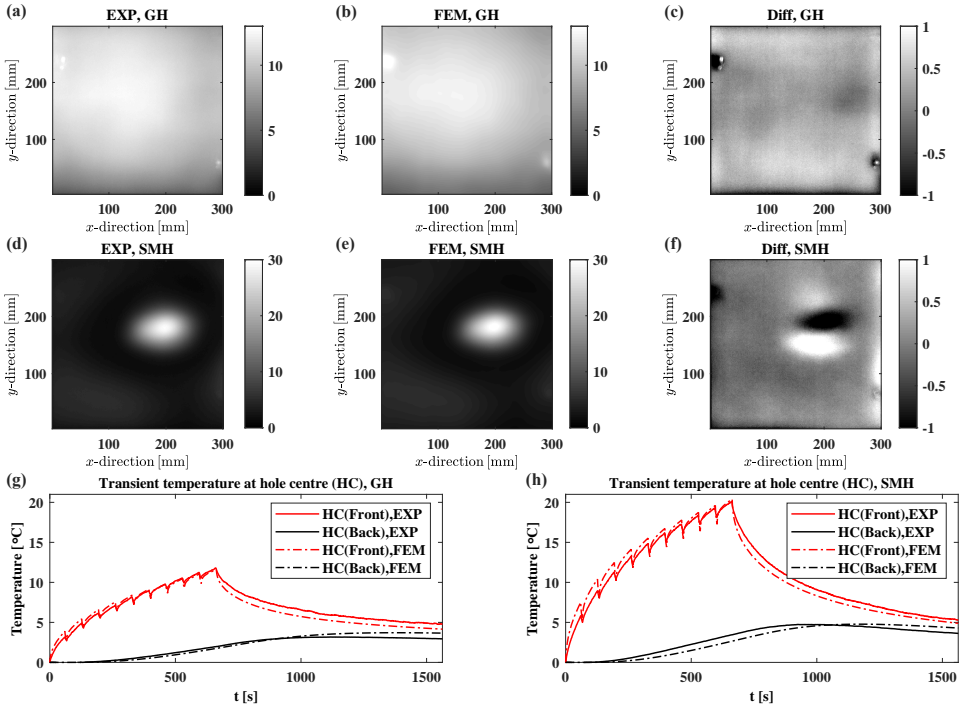
Figure 5.5: Comparison of transient temperature between experiments (EXP) and simulations (FEM): (a)-(c) transient temperature for GH right after the 10th cycle of heating, measured by experiments, predicted by FEM, and the corresponding difference. (d)-(f) transient temperature for SMH right after the 10th cycle of heating, measured by experiments, predicted by FEM, and the corresponding difference. (g)-(h) transient temperature at the front and the back of the hole center over time for GH and SMH, respectively (Front measured with the IR camera, back measured with the TC). [Temperature unit in °C]

The model comparison of simulated phase maps with measured ones is given here. The initial status before heating and the final status right after the 10th cycle of heating were utilised to build up total phase maps for comparison with experiments. Figures 5.6(a) and 5.6(b) are total phase maps (for GH) measured with shearography and simulated by FEM, respectively. The maximum phase values from the experiment and simulation are

both close to 60 rad, which indicates a good agreement between the experimental results and the FEM ones for GH. The corresponding difference is shown in Figure 5.6(c). The difference between experiment and simulation is around 6 rad at the center and ±16 rad near the edge for the total phase range -100 to +60 rad. Figures 5.6(d) and 5.6(e) are total phase maps (for SMH) measured with shearography and predicted by FEM, respectively. The maximum phase values by experiment and by simulation for SMH are also close to each other (~60 rad). The corresponding difference is shown in Figure 5.6(f), where the difference between experiment and simulation is around -10 to +20 rad near the modulated heating area and -16 to -10 rad near the right edge for the total phase range -80 to +60 rad. For both GH and SMH, it is shown that the difference between experiments and simulations near the edge area is a bit large. This may be because it is close to the edge of the FOV where the shear calibration is less reliable. Besides, factors such as non-ideal boundary conditions in the experimental set-up and lower signal-to-noise ratio at the corners due to the non-uniform distribution of the illuminating laser light may also contribute to this error. Shearography measurement uncertainty right at the boundary at the scale of shear distance (~7.8 mm) might contribute, which is expected to be small with reference to specimen size (~300 mm). For the analysis, only the effective area of inspection was taken in order to exclude shear uncertainty.
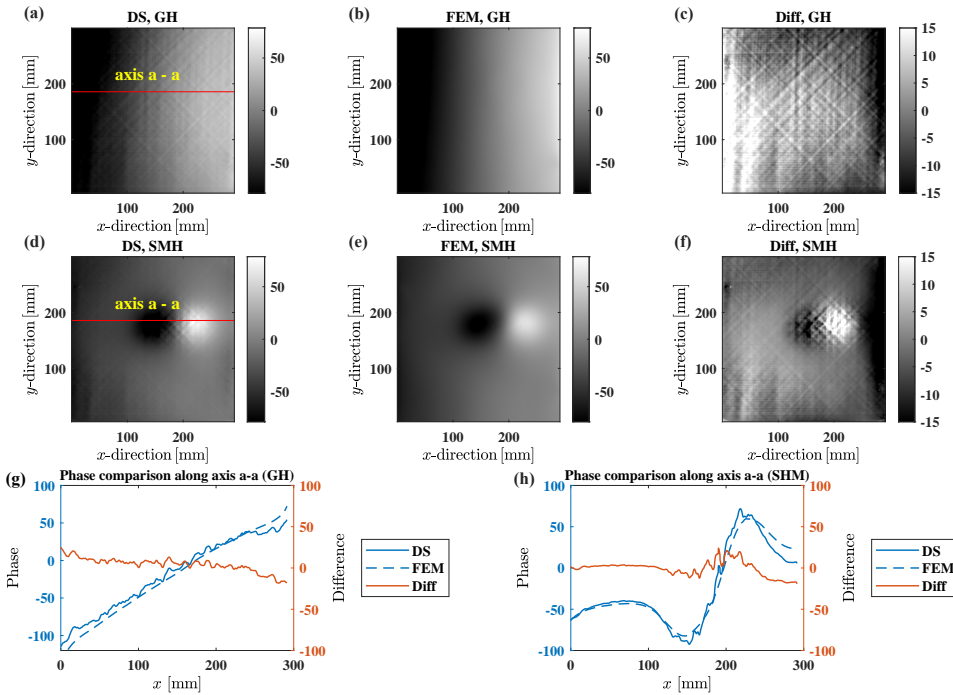
Figure 5.6: Comparison of total phase maps between experiments (DS) and simulations (FEM): (a)-(c) total phase maps measured with DS, simulated by FEM, and the corresponding difference for GH, respectively. (d)-(f) total phase maps measured with DS, simulated by FEM, and the corresponding difference for SMH, respectively. (g)-(h) the comparison of phase along axis a-a for GH and SMH, respectively. [Phase unit in rad, 1 rad ≈ 5.4 $\mu\varepsilon$]

Figures 5.6(g) and 5.6(h) show the phase comparison along axis a-a for GH and SMH, respectively. The blue lines in Figures 5.6(g) and 5.6(h) represent the phases by shearography (solid lines) and by FEM (dotted lines), respectively. The corresponding difference is shown by an orange line. It is shown that the phase curves obtained by experiments have a variation of about 3 rad standard deviation (Figure 5.6(g)). This variation, which appears as lines with angles of 0°, ±45°, 90° in Figure 5.6(c), is assumed to rise from the fibre deformation (e.g. related to fibre layup) which can be considered here as background noise. In the FEM, the fibre and resin were homogenised per equivalent layer, therefore the phase curves by simulation are smooth.

5.4.2. ANALYSIS OF DEFECT-INDUCED PHASE
This section reports on the analysis of defect-induced phase for GH and SMH, respectively. This part is an extension of the compensation method which was previously proposed in Section 3.3.3 and used in Section 4.4.2. The process for obtaining defect-induced phase from original phase maps is shown in Figure 5.7. For clarity, take global heating as an example. First the phase fringe maps (Figure 5.7(a), wrapped phases) are obtained by comparison of two deformation states of the specimen. After phase unwrapping, phase maps are obtained that are related to surface deformation. The original phase maps ($\delta\phi_{total}$, Figure 5.7(b)) contain information about both defect-induced deformation (defect signal) and overall deformation (background signal). In order to extract defect-induced deformation or defect-induced phase $\delta\phi_{DIP}$, a phase compensation process is needed (See Section 3.3.3), which can be done by the subtraction between the original phase map ($\delta\phi_{total}$) and the fitting surface created by a polynomial fitting of the original phase that represented overall deformation ($\delta\phi_{OD}$):

$$\delta\phi_{DIP} = \delta\phi_{total} - \delta\phi_{OD} \tag{5.2}$$

For the SMH scenario, the fitting plane created by the polynomial fitting is no longer useful due to the spatial modulation in heat flux. In order to overcome this problem, the shearography experiments were repeated (the same heating scenario, the same boundary condition) by replacing the defective plate (D60-Z25) with an intact plate (defect-free). The subtraction gives $\delta\phi_{sub}$ (Figure 5.7(h)),

$$\delta\phi_{sub} = \delta\phi_{defect} - \delta\phi_{intact} \tag{5.3}$$

where $\delta\phi_{defect}$ represents the phase with the defective plate, and $\delta\phi_{intact}$ represents the phase with the intact plate. Their subtraction ($\delta\phi_{sub}$) can help to remove overall deformation. Then a similar phase compensation process (similar to GH scenario, first creating a fitting surface from $\delta\phi_{sub}$ by using polynomial fitting and then subtracting it) can be performed to further remove overall deformation and therefore the defect-induced phase ($\delta\phi_{DIP}$, Figure 5.7(i)) for SMH can be obtained.

The above data processing method was performed for experimental data as well as for FEM data. It should be acknowledged that a limitation of the method is needing a reference undamaged panel for extracting defect-induced deformation by SMH, during which extra errors can also be introduced. The issue of extracting defect deformation by other methods will be the objective of future work. To reduce the extra errors in

this method as much as possible, it is suggested that the test panel and the reference undamaged panel need to be cut with the same dimensions from the same larger GFRP plate. Besides, the white painting on the surfaces of the panels (Figure 5.1(a)) needs to be sprayed in the same manner. It can be noted that after the phase compensation process, the obtained defect-induced phase from FEM data can be seen as a pure defect signal, while that from experimental data may still contain noise resulting from fibre-related deformation and speckle-related errors. These types of noise were not considered in modelling due to their complexity.
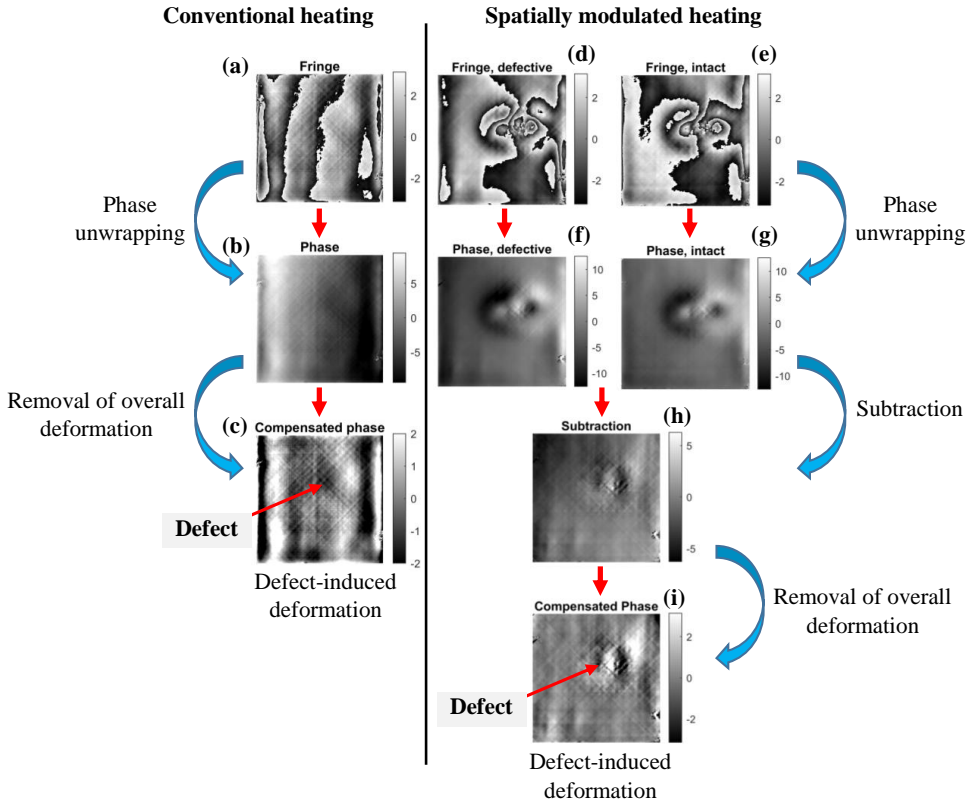
Figure 5.7: Data processing for obtaining defect-induced phase maps from original phase maps [Phase unit in rad]

The influence of reference states (Figure 5.4(a)) on deep defect detection with shearography was investigated by analysis of defect-induced phase. Figure 5.8 shows defect-induced phase maps corresponding to three representative reference states by GH, where the final states were at the same time instant during cooling. The three reference states include the 0th cycle of heating (representing status before loading), the 4th cycle of heating (representing status after 240 s of loading), and the 10th cycle of heating (representing status right after loading). Figures 5.8(a)-5.8(c) are defect-induced phase maps measured with shearography for the three reference states, and Figures 5.8(d)-5.8(f) are the ones

predicted by FEM. It is shown that as the reference status differs, the defect-induced phase map may change and therefore the efficacy of defect detection may vary. The defect (D60-Z25) is detectable from all the three simulated phase maps by FEM (Figures 5.8(d)-5.8(f)). However in experiments, it is detectable only from the reference status at the 4th cycle of heating (Figure 5.8(b)), which has a relatively good agreement with Figure 5.8(e) from FEM. While for the other two reference states, the defect is barely detected (Figure 5.8(a)) or partially detected (Figure 5.8(c)) possibly due to the influence of the fibre-related deformation. Figures 5.8(g)-5.8(i) show the defect-induced phase changes over cooling time for the three different reference states. An average defect-induced phase value of a 3×3 pixel region near the edge of the artificial defect was selected where the maximum defect signal was expected to occur. It should be noted that this selected region should also avoid the influence of fibre deformation as much as possible. The blue lines are from experimental data and the orange ones are from FEM data. It is shown that despite the influence of fibre deformation, the comparison of the maximum defect signal between shearography and FEM still shows a good agreement. Although the defect can be detected from the modelling point of view, nevertheless, in real experiments, the actual detection results may vary a lot due to choosing different reference sets of images. From the point of reducing the noise from fibre-related deformation, choosing the reference status during heating is favorable in comparison with the other two reference states, This is further explained in Section 5.4.3.

Figure 5.8: Defect-induced phase (DIP) maps by GH: (a)-(c) defect-induced phase maps by shearography (DS) for the three reference status, respectively. (d)-(f) defect-induced phase maps by FEM for the three reference status, respectively. (g)-(i) the defect-induced phase changes over cooling time for the three reference status, respectively. [Phase unit in rad, 1 rad ≈ 5.4 $\mu\varepsilon$]

The defect-induced phase maps by SMH are given in Figure 5.9. The final states were at the same cooling time instant, and similar to Figure 5.8, the same three different reference states (0th, 4th, 10th cycles of heating) were selected for comparison. Figures 5.9(a)-5.9(c) are defect-induced phase maps obtained by shearography data for the three different reference states, and Figures 5.9(d)-5.9(f) are the ones obtained by FEM data. It is also shown that as the reference status is different, the efficacy of defect detection may vary from the experimental results by shearography. This phenomenon is similar to the GH scenario, and a possible explanation can be found in Section 5.4.3. The comparison between shearography and FEM has a good agreement when selecting reference status as the 4th cycle of heating (Figures 5.9(b) and 5.9(e)). While for the other two reference status cases, the similarity between shearography and FEM is not ideal. This will also be discussed in Section 5.4.3 as well. Figures 5.9(g)-5.9(i) show the defect-induced phase changes over cooling time, where an average defect-induced phase value of a 3×3 pixels region near the defect edge was selected to indicate the defect signal. The blue lines are from experimental data and the orange ones are from FEM data. There is a larger difference in defect signal by SMH (Figure 5.9(g)) than that by GH. This is because for the SMH studied in this chapter, the heat flux is more concentrated than for GH, and the maximum heat flux by SMH is higher (around 3 to 4 times as that by GH), therefore the fibre deformation by SMH has a greater impact on the defect-induced phase maps compared with that by GH. It can be seen in Figures 5.9(g)-5.9(i), that the defect-induced phase curves by experiments and by simulations still show a good similarity.

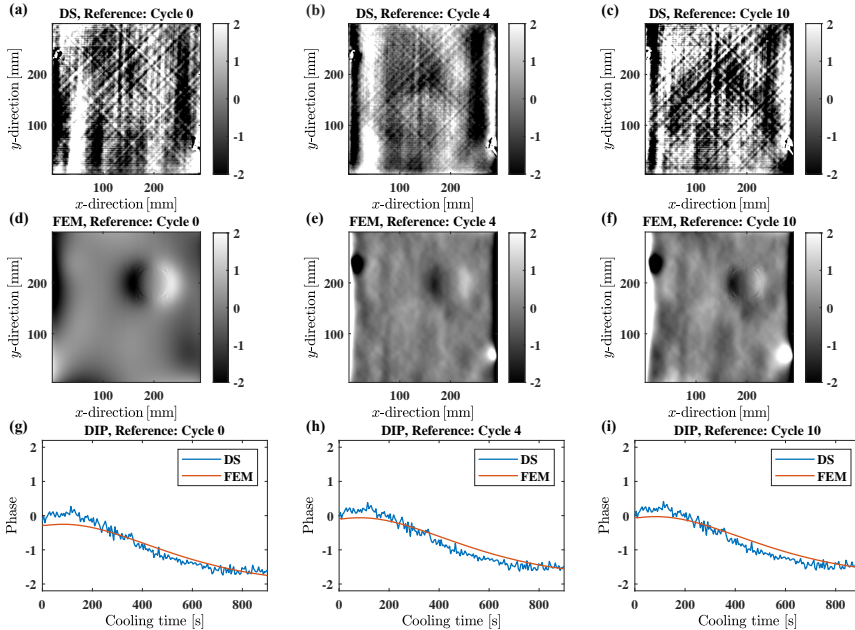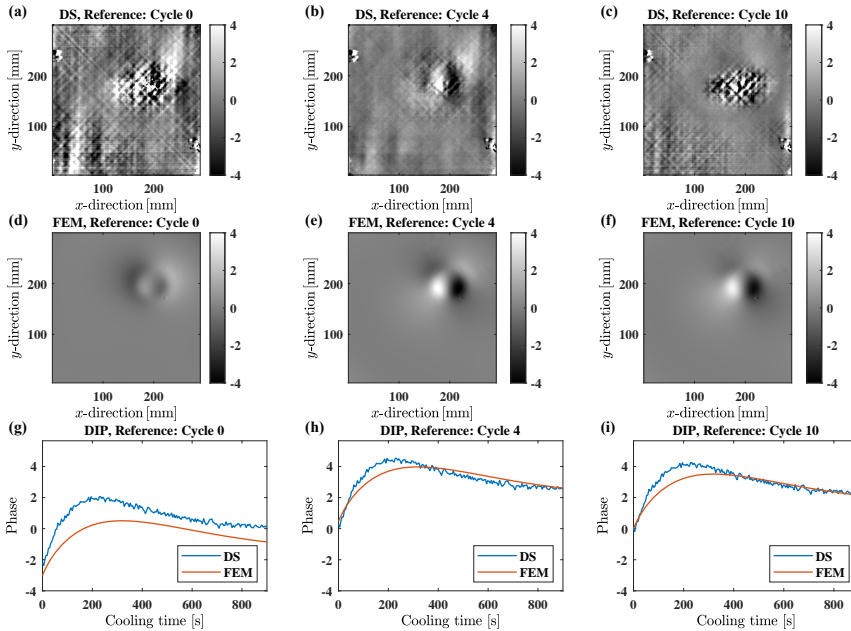Figure 5.9: Defect-induced phase (DIP) map by SMH: (a)-(c) defect-induced phase maps by shearography (DS) for the three reference status, respectively. (d)-(f) defect-induced phase maps by FEM for the three reference status, respectively. (g)-(i) the defect-induced phase changes over cooling time for the three reference status, respectively. [Phase unit in rad, 1 rad $\approx$ 5.4 $\mu\varepsilon$]

The experimental and numerical results for GH (Figure 5.8) and SMH (Figure 5.9) are summarized in Table 5.1. The maximum defect signal value is obtained from the results of reference status at the 4th cycle of heating since it shows a better performance in defect detection than the results from the other two reference status cases.

Table 5.1: Summary of maximum defect signal by SMH and GH, respectively

		SMH	GH
Average heat flux W/m^2		∼ 90	∼ 220
Maximum defect signal in phase (rad)	DS	∼ 4.5	∼ 1.5
	FEM	∼ 4.0	∼ 1.5

As shown in this table, the average heat flux by SMH is only about 40% of that by GH, but the maximum defect signal by SMH is around 2 to 3 times as large as that by GH, which is a significant improvement in defect detection. The defect-induced phase maps by SMH [Figures 5.9(b) and 5.9(e)] also show a better performance in defect detection than those by GH (Figures 5.8(b) and 5.8(e)).

5.4.3. ANALYSIS OF REFERENCE STATUS ON DEEP DEFECT DETECTION

It has been shown that the efficacy of shearography NDT of the deep defect in thick composite varies when selecting a different reference status (e.g. Figures 5.8(d)-5.8(f)). This could be due to their difference in temperature at the three reference states, indicating that the defect responses at the three reference states can vary. Hence, although the final states are the same, the comparison between the two states can be different, resulting in a variation in defect detection efficacy.

For both GH and SMH, it was also shown that the defect-induced phase map by shearography has a good agreement with that by FEM when selecting the reference state as the 4th cycle of heating. Nevertheless, the similarity between shearography and FEM results is not good when selecting the other two reference states for comparison. This could be because for these two reference status cases from shearography, the influence of fibre deformation is significant in the defect-induced phase maps, while as mentioned before, the fibre deformation was not considered in the modelling. Below, it will be discussed in more detail.

The average fibre deformation over time during the inspection is shown in Figure 5.10. The reference status is before loading. This figure was plotted by averaging the defect-induced phase maps of a selected region at each time instant. Since the defect-induced phase contains positive as well as negative values, their absolute values were averaged to represent the average fibre-related deformation during the inspection. The origin of time was right after the 10th cycle of heating, so the time with negative sign represents the cycling heating duration, and the time with positive sign represents the cooling duration.

It is shown that the maximum fibre-related optical phases are around 2.0 rad (GH) and 3.0 rad (SMH), respectively, which are comparable to the corresponding defect signal. In Figure 5.10, point R4 represents the status of fibre deformation at the end of the 4th cycle of heating and point S represents the final status selected in Section 5.4.2. It can be assumed that the fibre-related optical phases have no apparent difference for these two deformation states (R4 and S), therefore selecting the reference status as right after the 4th
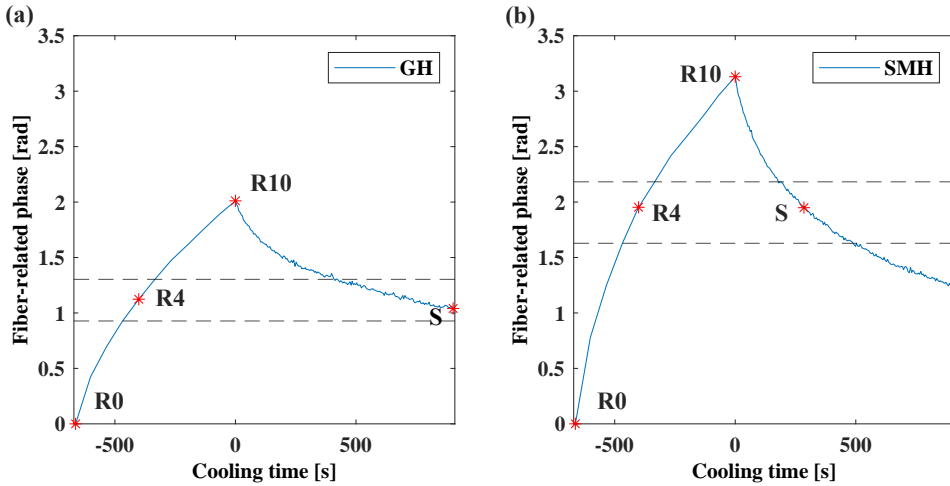
Figure 5.10: The average fibre deformation with time during the inspection (a) by GH, (b) by SMH.

cycle of heating (R4) yields relatively good results in defect detection as the influence of fibre deformation is reduced significantly. While selecting another reference status such as the 0th cycle of heating (R0) or the 10th cycle of heating (R10), the fibre-related phase will still have a great impact on the defect-induced phase maps, therefore it may affect significantly the efficacy of shearography inspection. A suggested rule for selecting the suitable reference and final states for shearography NDT of thick composites will be, to try to reduce the fibre-related phase as much as possible while keeping the defect signal as high as possible. For this panel, this can be done by a reference status of 40% of the overall heating time.

5.4.4. DISCUSSIONS ON SPATIALLY MODULATED HEATING

Some discussions on the spatially modulated heating for thick composite inspection with shearography are as follows:

1. With spatially modulated heating it is possible to improve the detection of the deeply buried defect in the thick composite laminate. As shown in this chapter, the maximum defect signal by SMH can be 2 to 3 times that from global heating with about 40% of the average heat flux (Table 5.1). This result is promising for improving deep defect detection even with low-power heating sources. Nevertheless, it should be addressed that due to non-uniform heating and the complex global deformation with SMH, additional measurements of a similar and defect-free reference sample are currently necessary to compare with those of a defective plate. To ensure that the test specimen and the reference undamaged one have identical thermal loading, the two specimens were cut with the same dimensions from the same larger GFRP plate. In practical applications, the composite structure to be inspected is often large-scale in dimensions (e.g., a ship hull) and the healthy regions of the structure can be used for the reference measurements. In order to use the presented method as a reference-free one, some advanced algorithms, e.g. phase compensation by combining analytical solutions of thermal deformation or

prediction by FEM may be useful to overcome this problem.

2. The efficacy of shearography NDT of the deeply buried defect in the thick composite laminate can vary when selecting different reference states, in which the issue of fibre-related deformation on deep defect detection should be treated carefully when applying thermal loading. A suggested rule for selecting the suitable reference states (as well as signal states) is, to reduce the background phase (e.g. fibre-related) as much as possible while keeping the defect signal high. In this chapter, this was achieved by selecting the reference status as 40% of the total heating time.

3. The current FEM model has the drawback of not considering fibre-related deformation and speckle-related errors. However it is acceptable for the sake of saving computational time.

Determining the heating position is important for spatially modulated heating. It is necessary to know the defects in advance because the efficacy of defect detection by the proposed SMH may vary greatly depending on the heating positions and the detection is expected to be more efficient as the heating position is close to the defect. Nevertheless, in a practical industrial inspection, the location of a defect usually remains unknown beforehand. To cope with this problem, a combination of GH and SMH for shearography NDT can be a reasonable solution for the detection of deep defects, that is, first applying GH for overall searching of suspicious areas, and then applying SMH for detailed characterisation of deep defects.

5.5. CONCLUSIONS

IN this chapter, RQ2 is fully answered. FEM-assisted shearography with spatially modulated heating has been proposed and applied for improving the detection of deep defects in thick composite laminates. Both global heating and spatially modulated heating were performed experimentally and modelled numerically for shearography NDT. The heat flux distribution on the specimen surface was taken into consideration in this study, which is rarely reported in defect detection with shearography. The influence of different reference states on shearography NDT of thick composites was studied in this chapter. Current results showed that SMH has one or a combination of the following advantages:

- Energy concentration

- High defect signal

- Deeper defect detection

- Improved edge detection of a defect

- Potentially fast inspection

In this study, an elliptical shape pattern was used with the proposed SMH method, as a rational result of the illumination setup with the Fresnel lens and heating at an angle. Other shapes or other types of SMH, e.g. by using multiple Fresnel lenses, can be investigated in the future.

REFERENCES

[1] N. Tao, A. G. Anisimov, and R. M. Groves, *FEM-assisted shearography with spatially modulated heating for non-destructive testing of thick composites with deep defects,* Composite Structures **297**, 115980 (2022).

[2] Y. Hung, *Shearography for non-destructive evaluation of composite structures,* Optics and Lasers in Engineering **24**, 161 (1996).

[3] Y. Hung, *Applications of digital shearography for testing of composite structures,* Composites Part B: Engineering **30**, 765 (1999).

[4] Y. Hung, L. Yang, and Y. Huang, *Non-destructive evaluation (NDE) of composites: digital shearography,* in *Non-Destructive Evaluation (NDE) of Polymer Matrix Composites*, Woodhead Publishing Series in Composites Science and Engineering, edited by V. M. Karbhari (Woodhead Publishing, 2013) pp. 84–115.

[5] J. W. Newman, *Shearography nondestructive testing of composites,* in *Comprehensive Composite Materials II*, edited by P. W. Beaumont and C. H. Zweben (Elsevier, Oxford, 2018) pp. 270–290.

[6] D. Akbari, N. Soltani, and M. Farahani, *Numerical and experimental investigation of defect detection in polymer materials by means of digital shearography with thermal loading,* Proceedings of the Institution of Mechanical Engineers, Part B: Journal of Engineering Manufacture **227**, 430 (2013).

[7] E. C. Krutul and R. M. Groves, *Opto-mechanical modelling and experimental approach to the measurement of aerospace materials using shearography and thermal loading,* in *Modeling Aspects in Optical Metrology III*, Vol. 8083, edited by B. Bodermann, International Society for Optics and Photonics (SPIE, 2011) p. 80831C.

[8] D. Buchta, C. Heinemann, G. Pedrini, C. Krekel, and W. Osten, *Combination of FEM simulations and shearography for defect detection on artwork,* Strain **54**, e12269 (2018).

[9] J.-F. Vandenrijt, H. Xiong, C. Lequesne, P. Blain, and M. Georges, *Shearography inspection of monolithic CFRP composites: finite element modeling approach for assessing an adequate strategy of artificial defects representing delamination,* in *Optical Measurement Systems for Industrial Inspection XI*, Vol. 11056, edited by P. Lehmann, W. Osten, and A. A. G. Jr., International Society for Optics and Photonics (SPIE, 2019) p. 110560I.

[10] N. Tao, A. G. Anisimov, and R. M. Groves, *Shearography non-destructive testing of thick GFRP laminates: Numerical and experimental study on defect detection with thermal loading,* Composite Structures **282**, 115008 (2022).

[11] G. De Angelis, M. Meo, D. Almond, S. Pickering, and S. Angioni, *A new technique to detect defect size and depth in composite structures using digital shearography and unconstrained optimization,* NDT & E International **45**, 91 (2012).

5

[12] Z. Liu, J. Gao, H. Xie, and P. Wallace, *NDT capability of digital shearography for different materials,* Optics and Lasers in Engineering **49**, 1462 (2011).

[13] D. Francis, R. P. Tatam, and R. M. Groves, *Shearography technology and applications: a review,* Measurement Science and Technology **21**, 102001 (2010).

[14] D. T. Goto and R. M. Groves, *Error analysis of 3D shearography using finite-element modelling,* in *Optical Micro- and Nanometrology III*, Vol. 7718, edited by C. Gorecki, A. K. Asundi, and W. Osten, International Society for Optics and Photonics (SPIE, 2010) p. 771816.

[15] A. G. Anisimov, M. G. Serikova, and R. M. Groves, *3D shape shearography technique for surface strain measurement of free-form objects,* Applied Optics **58**, 498 (2019).

[16] Y. Li, W. Zhang, Z. Yang, J. Zhang, and S. Tao, *Low-velocity impact damage characterization of carbon fiber reinforced polymer (CFRP) using infrared thermography,* Infrared Physics & Technology **76**, 91 (2016).

[17] H. Cheng, J. Gao, O. L. Kafka, K. Zhang, B. Luo, and W. K. Liu, *A micro-scale cutting model for UD CFRP composites with thermo-mechanical coupling,* Composites Science and Technology **153**, 18 (2017).

[18] T. L. Bergman, F. P. Incropera, D. P. Dewitt, and A. S. Lavine, *Fundamentals of heat and mass transfer* (John Wiley & Sons, 2017).

5

6

TEMPORALLY MODULATED HEATING FOR SHEAROGRAPHY NDT

This chapter aims at improving shearography NDT of deep defects in thick composites by using temporally modulated heating, which addresses RQ3 - 'How can temporally modulated heating be developed for improving thick composite inspection with shearography'. For that, a novel shearography method with controlled surface temperature (CST) heating has been proposed for deep defect detection (i.e., 15-25 mm depth and more) in thick GFRP laminates. The proposed CST heating method is developed based on the analytical solution of the constant surface temperature case to control the maximum surface temperature of a test object during inspection. Numerical and experimental studies have been performed to analyse the influence of various heating scenarios on defect behavior and defect detection. Compared with conventional shearography, the CST shearography method maximises heating energy input with a controlled and stable maximum surface temperature for deep defect detection. Results indicate an enhancement of about 27% in defect signal for the defect at 15 mm depth in comparison to conventional heating. The results also provide insight for implementing an efficient inspection in terms of the inspection duration and the number of datasets.

6.1. INTRODUCTION

ONE major concerning issue related to shearography with thermal loading is that thermal damage may occur if the maximum surface temperature exceeds a safe level, e.g. 80 °C for the material of the composite hull section in the RAMSSES project [2]. In conventional shearography methods such as flash shearography, high energy pulses can lead to over 100 °C for a fraction of a second, which may irreversibly damage a test object [3]. While in the cases of thick composites and deep defects, the shearography signal with a normal excitation level is usually low. To increase the signal, the heating can be increased and can reach kW power for minutes and dozens of minutes [4]. This amount of heating can be dangerous. Hence the maximum surface temperature of the test object needs to be controlled and thus a new modulated heating method is needed for safe shearography inspection. The focus needs to be placed on controlling the maximum surface temperature, meanwhile, the heating needs to be applied in an efficient way to save inspection time.

In the previous two chapters, shearography experiments were combined with the finite element method (FEM) to study the defect detection capability of shearography in the thick GFRP laminate (Chapter 4). Later spatially modulated heating was developed for shearography, where a reference undamaged panel is needed to compare with a defective one (Chapter 5). Nevertheless, temporally modulated heating has not been studied yet. Besides, defect detection and defect behaviour (especially for deep defects) under various heating scenarios have not been fully characterised.

In this chapter, a controlled surface temperature (CST) heating shearography method is proposed for deep defect detection in thick composites. The proposed CST heating enables the control and selection of the maximum surface temperature of a 51 mm thick GFRP laminate during the inspection. A combination of numerical modelling and experimental study was performed to investigate defect behaviour and defect detection in the thick composite under various heating scenarios including a new controlled surface temperature heating case and two conventional heating cases. The chapter is organized as follows. Section 6.2 introduces the test GFRP specimen, the CST shearography system and the principles for achieving controlled surface temperature heating, Section 6.3 presents the modelling approach. The results and discussion are presented in Section 6.4. First a model validation for the transient temperature and the surface strain of the thick GFRP laminate with experimental data is given in Section 6.4.1. Afterward, the analysis of various heating scenarios on defect behaviour and defect detection is addressed in Section 6.4.2.

6.2. SPECIMEN DESCRIPTION AND CST SHEAROGRAPHY SYSTEM

6.2.1. SPECIMEN FOR THE STUDY

The GFRP laminate from Chapter 4 was reused with some of the flat bottom holes re-manufactured for this study. It can be noted that when drilling flat bottom holes, manufacturing errors exist between the designed remaining thickness values and the actual ones. The holes were measured with a digital caliper (one standard deviation of 0.3 mm for 5 measurements). Experimentally measured thickness values (in brackets in Figure

6.1) were used for the FEM model in Section 6.3. The artificial defects are labelled with design values for convenience. The thermal and mechanical properties (e.g., thermal expansion coefficients, specific heat, elastic modulus) of the material can be found in Section 3.2.
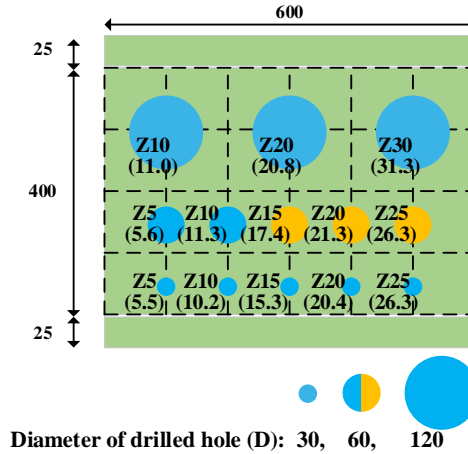
Figure 6.1: Diagram of the GFRP specimen with design value prefixed by Z and experimentally measured hole thickness in brackets. [Dimensions in mm]

In this chapter the focus is on defects Z15, Z20 and Z25 with a diameter of 60 mm (in orange color in Figure 6.1) for the objective of deep defect detection and due to a limitation of the field of view of the shearography system used (about 380×320 mm^2). The results from the three defects will be presented in Section 6.3.

6.2.2. SHEAROGRAPHY SYSTEM WITH TEMPORALLY MODULATED HEATING

A schematic of the out-of-plane (i.e., $\partial w/\partial x$) shearography setup with temporally modulated heating and the experimental shearography system are shown in Figure 6.2. During the experiments, three halogen lamps (Figure 6.2(b)) were used for applying CST heating, of which the electrical power was controlled in the range of 0 to 1000 W each by specific hardware and LabVIEW. The actual heat flux from the lamps on the specimen surface with heating power was calibrated in the lab before performing the controlled surface temperature heating. The calibration was done in the full range of the lamps heating power with the surface temperature measured by the IR camera. Then the actual heat flux was calculated by solving an inverse problem from the thermal response (measured surface temperature) [5]. The 7th-degree polynomial was used to fit in the experimental data points and further used for a direct control of the heat flux on the surface for the controlled surface temperature heating. The actual heat flux range from the lamps on the specimen surface is up to 1400 W/m^2. In this study, three heating scenarios (Figure 6.3) were designed based on the idea of controlling maximum surface temperature and were applied in the shearography experiments. It can be noted that due to non-uniform heating, the maximum temperature on the specimen surface was monitored and manually determined with an IR camera (FLIR A655):

(1) CST780s (solid red line): new controlled surface temperature heating method for 780 s, the maximum surface temperature increases and then remains at 60 °C during heating.

(2) CH780s (blue line): conventional constant heat flux heating with the same heating time as the CST780s case. The maximum surface temperature was the same as the CST780s case with reduced heating power.

(3) CH278s (black line): conventional constant heat flux heating with full maximum available power. The maximum surface temperature was the same as the CST780s case with a reduced heating time of 278 s.
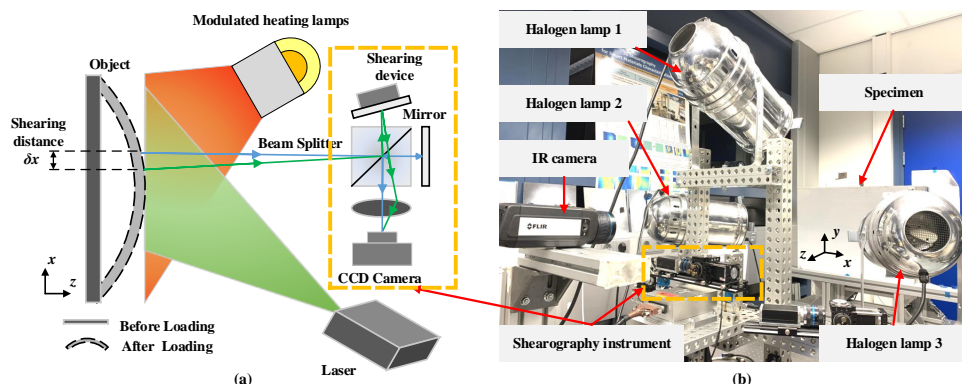
Figure 6.2: Schematic of shearography (a) and the experimental system (b). The specimen is placed at a distance of approx. 1.2 m from the shearography instrument.

As shown in Figure 6.3, the maximum surface temperature in the CST heating can remain around 60 °C for 20 mins and more (CST1380s in dotted red line). This indicates that the proposed CST heating can control the surface temperature for a long period of heating. In other words, it allows high heating energy input with a controlled and stable maximum surface temperature for deep defect detection.
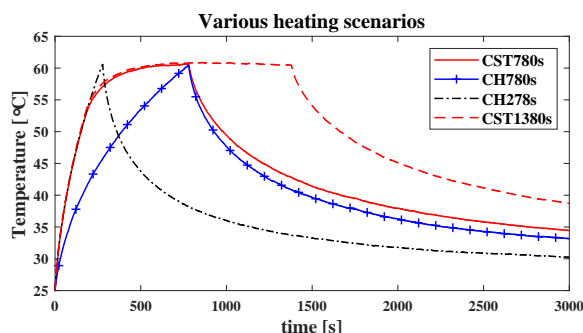
Figure 6.3: Various heating scenarios used in the investigation (surface temperature). CST780s, CH780s and CH278s were applied in shearography experiments; CST1380s as a reference to validate that the proposed CST heating can control the surface temperature for a long period of heating.

6.2.3. CONTROLLED SURFACE TEMPERATURE HEATING

This section presents the principles of controlled surface temperature heating during the thermal excitation of the object.

For thick composite inspection and deep defect detection with shearography, the defect signal with a normal thermal excitation level is usually low. To increase the defect signal, the heating intensity and time need to be significant [4]. This heating amount may be dangerous when the surface temperature of the test object exceeds a certain value, e.g. 80 °C for the used specimen [2]. Hence the maximum surface temperature needs to be controlled for safe shearography inspection.

Here the problem is simplified as a 1D heat transfer problem where heat propagates in the through-thickness direction z, therefore the thermal properties of conductivity in the through-thickness direction (k_z) and the corresponding thermal diffusivity ($\alpha_z = k_z / \rho c_p$) are considered. Under the heating scenario of constant surface temperature, the surface temperature of the specimen $T(0, t)$ is controlled to be a constant value T_s over time t:

$$T(0, t) = T_s \tag{6.1}$$

As the specimen is thick (~ 51 mm) and its thermal diffusivity in the through-thickness direction is small ($\alpha_z \approx 0.23 \times 10^{-6}$ m^2/s for the used specimen), the analytical solution of a semi-infinite solid was applied to obtain the transient temperature of the specimen $T(z, t)$ through-thickness direction (z) [5]:

$$\frac{T(z, t) - T_s}{T_i - T_s} = \mathrm{erf}\left(\frac{z}{2\sqrt{\alpha_z t}}\right) \tag{6.2}$$

where T_s is the controlled surface temperature, T_i is the initial temperature of the specimen before heating, erf is the error function, α_z is thermal diffusivity in the through-thickness direction, and t is the heating time. So the calculated heat flux q_s on the specimen surface ($z = 0$) is [5]:

$$q_s = -k_z \left.\frac{\partial T}{\partial x}\right|_{z=0} = \frac{k_z (T_s - T_i)}{\sqrt{\pi \alpha_z t}} \tag{6.3}$$

where k_z is the laminate conductivity in the through-thickness direction.

Eq. 6.3 shows that in order to achieve controlled constant surface temperature heating, the applied heat flux should be proportional to the reciprocal of the root of heating time t.

In this study, the initial temperature of the specimen is about 25 °C and the controlled surface temperature is set to $55 - 60$ °C to obtain a safe and reasonable temperature increase for defect detection. The theoretically calculated heat flux over time is shown in Figure 6.4 (black line). It can be seen that heat flux goes to infinity when the heating time t is close to 0 s, so this case is not practical in experiments. As a compromise, first the specimen is heated with the full maximum available power to get the desired temperature as fast as possible (about 30 °C increase in 180 s) and then modulated heating is applied following Eq. 6.3 to maintain a controlled constant surface temperature. The calculated heat flux is shown as the red line in Figure 6.4. It should be acknowledged that Eq. 6.3 does not take heat loss into account. So to compensate for heat loss in experiments, the heat flux is further modified by a factor of approx. 1.1 (blue line in Figure 6.4). This factor was experimentally determined by testing different scaling factors for better fit.

6

In shearography applications with thermal loading, the selection of heating time often highly depends on experience or practice, which may affect the effectiveness of the inspection. Here heating time is determined based on thermal penetration depth ($\delta_p = 2.3\sqrt{\alpha_z t}$) [5], which is related to the thermal diffusivity in the thickness direction (α_z) of the material and time t. The thermal penetration depth of the test GFRP specimen is shown in Figure 6.5.

For defects at about 15, 20 and 25 mm depth (Z15, Z20, Z25) in this GFRP specimen, it takes 160-220, 290-390 and 450-610 s, respectively, for heat to propagate. Therefore, the heating time was chosen to be 180 s of full power heating plus 600 s of modulated heating, resulting in a total heating time of 780 s for the CST780s case. These should be reasonable parameters for the investigation. It is also seen that it takes 1800-2500 s for heat to propagate to the back surface of the specimen (51 mm), which is much longer than the selected heating time. So Eq. 6.3 is expected to be valid in the chosen heating duration. In experiments, the temperature profiles of the front surface were measured for different modulated heating times, and they showed a stable constant surface temperature heating with a variation of one standard deviation of 0.64 °C from the desired 60 °C within 1380 s heating (red dotted line in Figure 6.3).
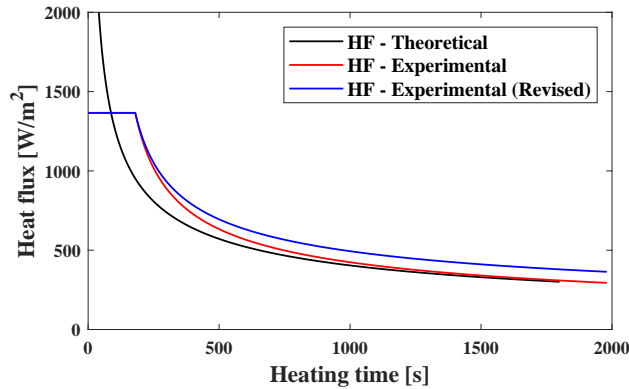
Figure 6.4: Calculated heat flux for controlled surface temperature heating

6.3. NUMERICAL MODELLING

THREE heating scenarios, namely the CST780s, CH780s, and CH278s cases (Figure 6.3), were modelled. The established FEM model (Figure 6.6) enables a more comprehensive understanding of the influence of various heating scenarios on defect behaviour and defect detection in thick composites with shearography.

The required equivalent properties including effective elastic moduli for modelling can be found in Section 3.2. For this study, effective laminate conductivities were measured 10 times with a Hot disk TSP2200 instrument and averaged axial (through-thickness direction) and radial (in-plane) conductivities of about 0.38 and 0.59 W/ (m·° C), respectively, were obtained. These values were included in the model.

The heat flux distributions of the three heating scenarios on the specimen surface were experimentally characterised by combining transient temperature measured with
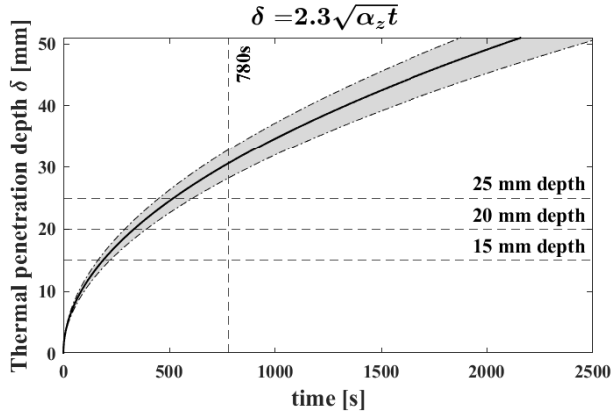
Figure 6.5: Thermal penetration depth of the GFRP laminate, a 15% variation in thermal diffusivity in the through-thickness direction α_z is indicated by the grey region.

an IR camera and a 1D analytical solution of heat conduction in the semi-infinite solid [5], as in Chapter 5. Other methods may also be used to measure energy density [6, 7] on the specimen, here the adopted method was used due to its ease of application for constant heat flux heating. The experimentally-estimated heat flux distributions were used as an input of thermal loading in the modelling.

For the modelling of heat loss from the composite laminate to the environment. Small heat transfer coefficients (front surface of 2-3 W/(m$^2 \cdot$K) and back surface of 8-12 W/(m$^2 \cdot$K)) were selected for the model. The heat loss of the front and back surfaces was set differently due to the remaining heat of the lamps when they were turned off after heating. This approach showed a reasonable accuracy in the temperature comparison between the FEM and experiments (Figure 6.7 in Section 6.4.1). The element type of the model is C3D8RT which is commonly used for coupled temperature-displacement analysis [8, 9]. The model consists of about 700000 elements, which takes about 30 hours of computational time using a high-performance computing (HPC) cluster.

Simulated phase maps were computed from the FEM displacement data to compare with experimental ones. The experimentally-determined shear calibration according to [10, 11] was taken into account to correct the simulated phase maps. The calibrated area for the shearography experiment is marked in red in Figure 6.6. The shear distance was found to be 8.1 ± 0.32 mm (mean ± std) over the calibrated area.

6.4. RESULTS AND DISCUSSION

THIS section reports the numerical and experimental results of CST shearography for the detection of deep defects in the thick composite laminate (Figure 6.1). Three heating cases including CST780s, CH780s and CH278s were modelled in Abaqus (FEM) and applied in shearography experiments (DS). The influence of the three heating scenarios on defect behaviour and defect detection was investigated. In FEM, both heating and cooling durations were simulated and analysed, while in the shearography experiments, measurements were taken only during cooling because during heating the light from the

Figure 6.6: The established model with mesh. The shear distance calibration area in shearography (DS) experiments is marked in the red line.

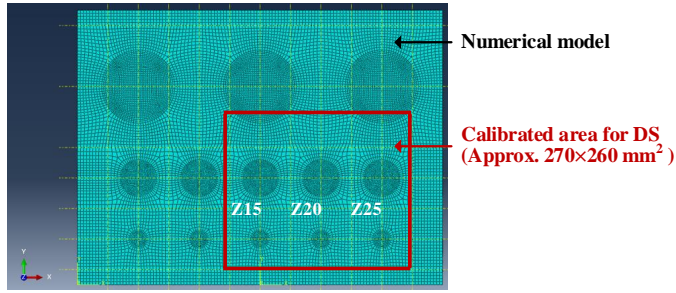lamps can saturate the shearography camera sensor. A Thorlabs bandpass filter (FLH532-4, transmission > 90%) with a center wavelength of 532 nm and bandwidth of 4 nm was used for optical filtering, however, this optical filtering was found to be not efficient enough for measurements during heating. As mentioned in Section 6.2.1, the focus is on defects Z15, Z20 and Z25 of diameter 60 mm in this study. The raw data (phase-shifted speckle interferograms) is available at [12] with the metadata to reproduce the experimental results. The unit of phase in shearography is radian, and in this instrument-specimen geometry, 1 rad corresponds to 5.2 $\mu\varepsilon$ (out-of-plane displacement derivative $\partial w/\partial x$).

6.4.1. THE VALIDATION OF THE THERMAL-MECHANICAL MODEL

As seen from the heating profile in time (Figure 6.3), the CST780s heating is the most complicated scenario in this investigation, therefore here a comparison of experimental and numerical results of the CST780s heating case is presented for model validation. To validate the model, the temperature and strain behaviours were modelled and measured for a direct comparison (Figures 6.7 and 6.8).

First, the model validation of temperature behaviour is done. Figures 6.7(a)-6.7(b) and 6.7(d)-6.7(e) show 2D plots of the transient temperature of the specimen surface by experiment and by FEM at two instants of time, namely 780 s (right after heating, the start of shearography measurements) and 2490 s (after 1710 s cooling, the end of shearography measurements), respectively. The difference between measured and predicted temperatures is about ±2 °C (Figures 6.7(c) and 6.7(f)) when the total range is about 35 °C. It shows a good agreement between experiment and simulation. The difference mainly occurs at the top region. This can be related to the estimated heat flux distribution which is calculated based on 1D heat conduction [5].

Figures 6.7(g) and 6.7(h) show transient temperature over time at the front and back of the hole centers of defects Z15, Z20 and Z25, respectively. During the first tens of seconds of heating, the temperature from FEM is 2-3 °C higher than that from experiments, this can be because of an overestimated heat flux at the early stage of heating. The maximum temperature difference between the experiment and simulation during cooling is about 2 °C. Possible reasons include a mismatch of estimated heat loss with the actual values during experiments and measurement errors in the conductivity of the through-thickness direction. Based on Figure 6.7, the FEM model can predict the transient temperature of
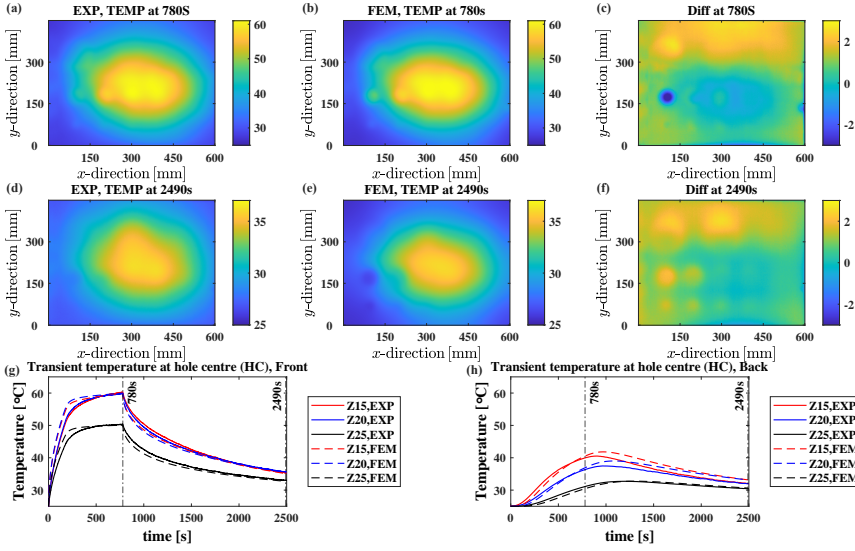
Figure 6.7: Model validation for transient temperature: (a)-(c) transient temperature at 780 s (right after heating) measured by experiments (EXP), predicted by FEM and the corresponding difference. (d)-(f) transient temperature at 2490 s (after 1710 s cooling) by EXP, by FEM and the corresponding difference. (g)-(h) transient temperature at the front and the back of the hole centers over time (front measured with the IR camera, back measured with thermocouples).

the $[0/45/90/-45]_{60}$ GFRP laminate with reasonable accuracy.

Second, the model validation of the simulated phase with the experimental phase (proportional to strain) is given here. Figures 6.8(a)-6.8(c) are original phase maps measured with DS, predicted by FEM, and the corresponding difference, respectively. The initial state is right after heating and the final state is after 1710 s cooling (the end of the shearography measurements). The difference between DS and FEM is about -20 to +20 rad for a total phase range of 370 rad. The main contributors are the local fibre-induced deformation (vertical and diagonal lines in Figure 6.8(c)), and the top-left and bottom-right corners which may be caused by a difference in the effective boundary conditions and the effectiveness of the shear calibration. A comparison of the original phase along the a-a axis is shown in Figure 6.8(g), it indicates a good agreement between the experiment and the simulation.

As no defects are visible in Figures 6.8(a) and 6.8(b), a compensation process (see Section 3.3.3) was further performed to extract defect-induced phase maps. The defect-induced phase (DIP) maps measured with DS, predicted by FEM, and the corresponding difference are shown in Figures 6.8(d)-6.8(f). The initial and final states were selected to obtain the highest defect signal during cooling. The experimental DIP map and the simulated one show a reasonable agreement; their corresponding difference is about -8 to +8 rad. It can be noted that the total range of the original phase map is about 370 rad. The main contributor to this difference is local fibre-induced deformation. As will be seen later in Figure 6.11 in Section 6.4.2, the standard deviation of fibre-related deformation is about 5 rad. Besides, the temperature mismatch between FEM and experiment during cooling

(Figure 6.7), the effect of local stiffness (e.g., due to manufacturing defects, Figure 3.2(b)), and the errors from the compensation process may also contribute to this difference. From both simulated and experimental DIP maps (Figures 6.8(d)-6.8(e)), the defects Z15 and Z20 are clearly detected, while defect Z25 is close to the detection sensitivity.

Based on both temperature and phase comparisons, the established FEM model can predict the thermal-mechanical response with reasonable accuracy.
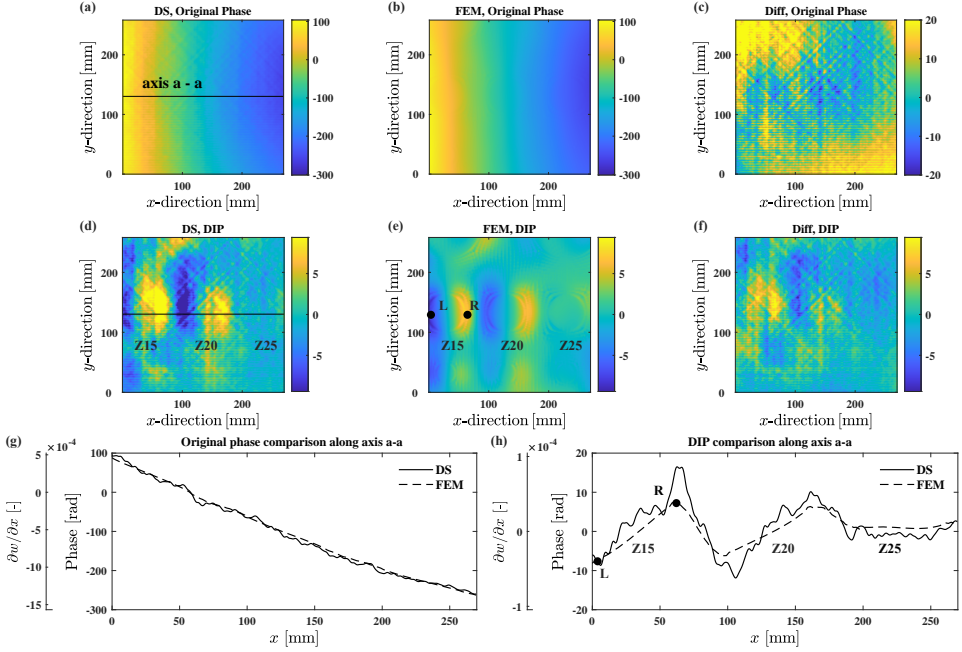
Figure 6.8: Model validation for shearography phase: (a)-(c) original phase maps measured with shearography (DS), simulated by FEM and the corresponding difference, respectively. (d)-(f) defect-induced phase (DIP) maps by DS, by FEM and the corresponding difference, respectively. (g)-(h) a comparison of phase along the a-a axis for the original phase and defect-induced phase, respectively, (g)-(h) supported with the strain axis. [1 rad corresponds to 5.2 $\mu\varepsilon$]

6.4.2. ANALYSIS OF VARIOUS HEATING SCENARIOS ON DEFECT BEHAVIOUR AND DEFECT DETECTION

As the thermal-mechanical model is of reasonable accuracy, shearography experiments were combined with the FEM model to obtain a more comprehensive understanding of various heating scenarios on defect behaviour and defect detection in thick composites. This section reports experimental and numerical results to prove the efficacy of the proposed CST heating and the shearography.

First, the temperatures of the three heating scenarios were compared. Figure 6.9 shows the transient temperatures at defect depths Z15, Z20 and Z25 (i.e., hole centers at the back surface) for the three heating scenarios.

Both experimental and FEM results show that the maximum temperature at the

three defect depths occurs later after the heating stops (e.g., for CST780s, the maximum temperature occurs at around 1100 s while the heating time is 780 s). It indicates a delay between the thermal excitation and the transient temperature response at the defect region. Moreover, the maximum temperature at those defect depths by CST780s is higher than the other two heating cases; this is straightforward to explain as CST780s uses more energy to excite the object than the other two conventional heating cases. Normally in inspection practice heating energy is not a limiting factor, however, the way the higher energy is applied has to be controlled to ensure safe inspection, which is realised with the proposed CST method.
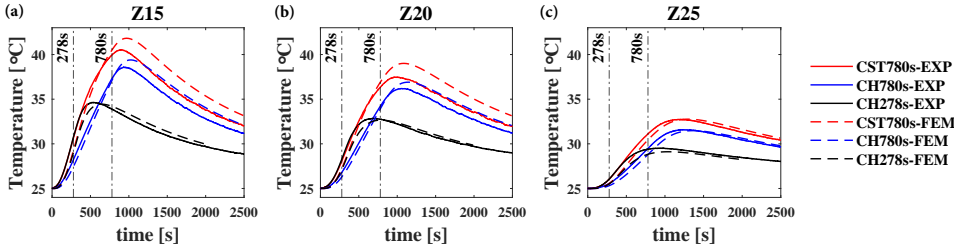
Figure 6.9: Transient temperatures at defect depths of (a) 15 mm, (b) 20 mm, and (c) 25 mm for the three heating scenarios. [the solid lines: measured with thermocouples (EXP); the dotted lines: from simulations (FEM)]

Second, the shearography phase of the three cases. Figure 6.10 shows the comparison of the experimental and simulated DIP maps for the three thermal loading schemes. As seen from the obtained DIP maps, the defect signal with CST780s (Figures 6.10(a) and 6.10(d)) is higher than that with CH278s (Figures 6.10(c) and 6.10(f)) and it is slightly higher than that with CH780s (Figures 6.10(b) and 6.10(e)).

For defect Z15, the defect signal from CST780s is higher than that from CH780s, while for defect Z20, the defect signals from the CST780s and CH780s heating scenarios are close to each other (Figures 6.10(g) and 6.10(h)). This may indicate that although there is a benefit of a higher temperature rise at the various defect depths with CST780s, the influence on defect deformation or defect signal is limited as defect depth increases. As shown in Figure 6.10, defects Z15 and Z20 are detectable for the three heating scenarios from both experimental (Figures 6.10(a)-6.10(c)) and simulated (Figures 6.10(d)-6.10(f)) DIP maps. However, defect Z25 appears to be close to the detection sensitivity for all the three cases.

To further investigate the variation of defect deformation during cooling for the three heating scenarios, the evolution of defect deformation corresponding to the reference state right after heating over the inspection time was made, as shown in Figures 6.11(a)-6.11(c). Signals from the defects at depths of Z15, Z20, and Z25 and the heating scenarios of CST780s, CH780s, and CH278s were obtained by averaging defect-induced phases at the left and right edges of each defect (e.g., (-L+R)/2 in Figures 6.8 and 6.10), as the defect signal is the highest there. Considering that DS measurements were taken only during the cooling of the specimen, here the origin of time was right after heating (t=0 s).

The dotted lines are from the FEM results and the solid lines are from the experimental (DS) results. During the heating (t = [-780 0]), defect deformation was not available by DS

as the light from the lamps can saturate the shearography camera sensor. Therefore it was only derived from FEM data. During the cooling ($t = [0\ 1710]$), defect deformation was derived from both FEM and DS data. In Figure 6.11(a), shaded error bars were made for the three thermal loading schemes in experiments by calculating one standard deviation of the DIPs from a 10×200 pixel area (corresponding to 1.6×33.0 mm^2 area) at the defect edges. The error sources are expected to mainly come from fibre-related deformation that commonly exists in fibre-reinforced composites under thermal loadings (as discussed in Section 5.4 in Chapter 5). In Figures 6.11(b) and 6.11(c), only the shaded error bars of the CST780s case were plotted to make it concise. Figure 6.11(d) shows the background deformation of an intact area for the three heating scenarios. The solid (DS) and dotted (FEM) lines were made by averaging the DIPs of an intact region, shaded error regions were also made for the three thermal loading schemes in experiments by calculating one standard deviation of the DIPs from the intact area. The background deformation mainly comes from complex fibre-related deformation and the compensation process. It can serve as a baseline for defect detection in thick composites.
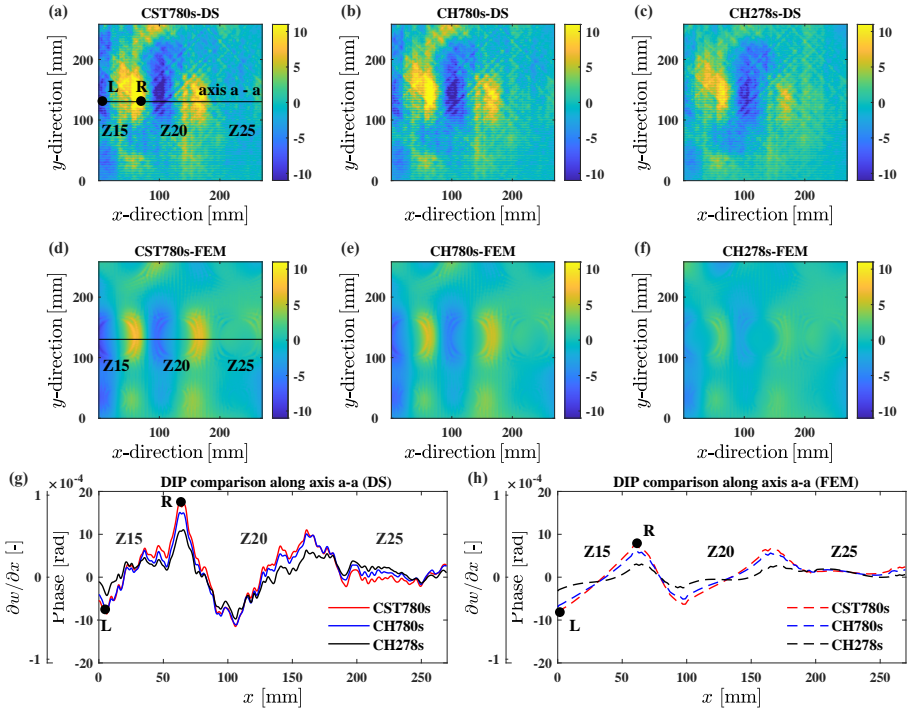
Figure 6.10: The defect-induced phase (DIP) maps for the three heating scenarios: (a)-(c) CST780s, CH780s, CH278s from experiments (DS); (d)-(f) CST780s, CH780s, CH278s from simulations (FEM); (g)-(h) the comparison of DIP along the a-a axis for the three heating scenarios, supported with the strain axis. The solid lines are from experiments (DS); the dotted lines are from simulations (FEM). [1 rad corresponds to $5.2\ \mu\varepsilon$]

Table 6.1 summarises the variation range of DIP during the cooling time for the three defects (data from Figures 6.11(a)-6.11(c)). Both modelling and experimental results show

that the DIP range with the CST heating for the defects at 15 and 20 mm depth is higher than with both conventional heating scenarios. The ranges OB and BC (Figure 6.11(a)) can both represent the variation range of DIP during the cooling time. In this paper, the range BC was used as the fibre-related noise is lower. The effect of the CST heating decreases as the defect depth increases, while the defect Z25 (Figure 6.11(c)) is close to the detection sensitivity as its defect signal is comparable to the fibre deformation from the intact area (Figure 6.11(d)). The defect Z25 is rather deep, so more time can be needed for heat to propagate and interact with the defect. From the FEM results, it is seen that during heating the defects Z15 and Z20 have high defect signals (Figures 6.11(a)-6.11(b), up to -8 rad). While the defect Z25 has a rather low defect signal (Figure 6.11(c), up to 2 rad), and the signal of the defect Z25 during cooling is also close to the detection sensitivity, which is similar to experimental results. There are two supplementary videos [12], from which readers can make their own decision about the influence of the reference state on the detectability of defect Z25.
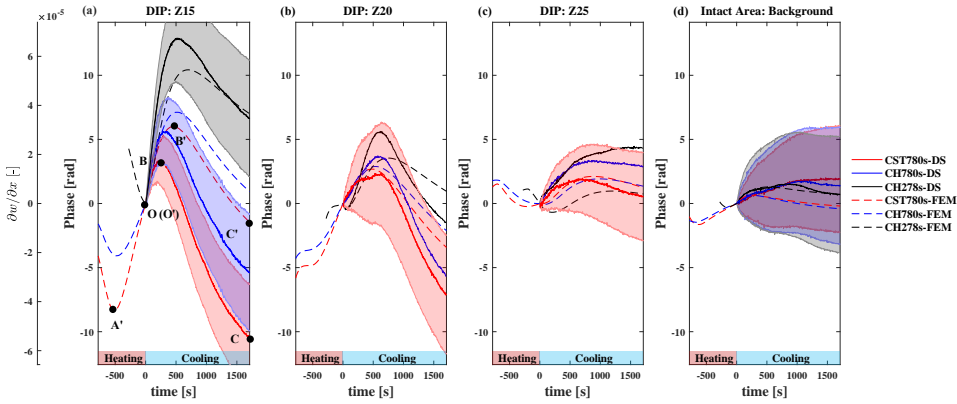
Figure 6.11: The defect-induced phases (DIPs) of the three artificial defects over time for the three heating scenarios: (a) Z15, (b) Z20, (c) Z25, (d) background phase of an intact area [the solid lines: from experimental results (DS); the dotted lines: from simulated results (FEM), 1 rad ≈ 5.2 $\mu\varepsilon$]

Figure 6.11(a) and 6.11(b) also show that there can be an extreme DIP occurring during heating as well as during cooling. For example for the defect Z15, extreme DIP values occur at the time moments of around -500 and 500 s, where only two sets of interferograms need to be taken and further processed (Figure 6.12). These time moments provide the highest value of DIP of up to 14.3 rad. Therefore it can be a benefit for implementing an efficient inspection in terms of the inspection duration and the amount of data.

Table 6.1: Variation range of DIP during the cooling time, phase unit in rad

	Z15		Z20		Z25	
	FEM	DS	FEM	DS	FEM	DS
CST780s	7.2	13.6	5.7	9.3	0.5	1.3
CH780s	6	10.7	4.9	9	0.3	0.4
CH278s	3	6.3	2.6	7	0.3	0.9

As explained before, the focus is on improving deep defect detection with the defect size of 60 mm because of its interest for the marine sector. For comparison, the size of realistic defects and damage for marine composites is usually 100 mm and more [2, 13]. As the presented results were achieved with the test GFRP panel and in the lab environment, the capability of shearography technique in the presence of realistic defects and in-situ tests on large-scale marine structures will be investigated in Chapter 7.

Figure 6.12: The DIP maps (for full specimen): (a) choosing reference states during cooling (dotted red area was compared with experiments) and (b) during heating, respectively. The ranges C'B' and A'B' can refer to Figure 6.11(a).

6.5. CONCLUSIONS

IN this chapter, RQ3 is fully answered. The novel CST shearography method was proposed and adopted for thick composite inspection. For the first time, defects at 15-25 mm depth have been detected in thick GFRP panel 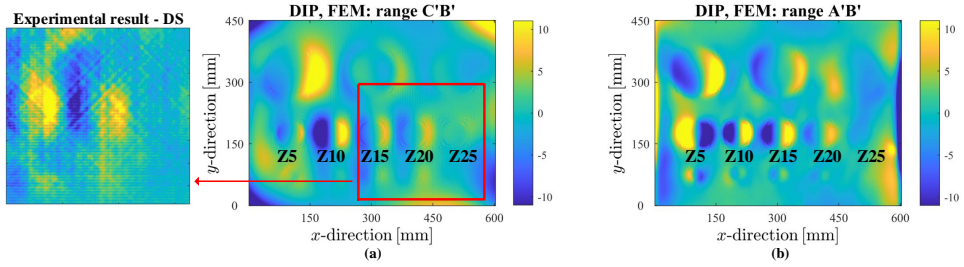with controlled maximum surface temperature. To the best of our knowledge, no literature has reported on temporally modulated heating that enables the control and selection of maximum surface temperature for thick composite inspection. Moreover, few studies are available on defect behaviour and deep defect detection under various heating scenarios with shearography. This work makes a step forward in safe shearography inspection for deep defect detection where overheating may cause thermal damage. A numerical and experimental study was conducted to analyse defect behaviour and defect detection under three heating scenarios including a new CST heating and two conventional heating scenarios. The main conclusions are summarized as follows:

1. The advantage of CST heating is that it maximises heating energy input with a controlled and stable maximum surface temperature, along with a higher temperature rise at the defect depth. The experimental and numerical results indicate that defects at 15 and 20 mm depths can be reliably detected with CST heating. The defect-induced phase range with CST heating for these two defects is higher than with both conventional heating methods. For defect Z15, the defect signal with CST780s is about 27% higher than with CH780s and 116% higher than with CH278s. However, the effect of CST decreases as the defect depth increases, with the defect at 25 mm depth close to the detection sensitivity. More time (e.g., a dozen to dozens of minutes of heating) is needed for heat to propagate and interact with defects of 25 mm depth or more.

2. The established FEM model can serve as a predictive model for investigating

and determining the behaviour of the thick composite for defect detection. Practical industrial inspection is usually difficult because experiments have problems including global deformation, non-uniform heating and vibration. Therefore reliable FEM guidance is needed. This FEM guidance saves time during experiments. Besides, FEM during heating shows the benefit of reference states and highlights the value of measurements during heating to be done.

3. This study also provides insight for implementing an efficient inspection in terms of the inspection duration and the number of datasets, e.g., only two sets of interferograms during heating and cooling need to be recorded, producing the highest defect-induced phase value for defect detection.

The conclusions were achieved with the test GFRP panel and in the lab environment, the capability of the shearography technique in the presence of realistic defects and in-situ tests on large-scale marine structures will be investigated in Chapter 7.

REFERENCES

[1] N. Tao, A. G. Anisimov, and R. M. Groves, *Towards safe shearography inspection of thick composites with controlled surface temperature heating,* NDT & E International **139**, 102907 (2023).

[2] S. Paboeuf, A. de Bruijn, F. Evegren, M. Krause, and M. Elenbaas, *A "fast track to approval" process for innovative maritime solutions,* in *Practical Design of Ships and Other Floating Structures,* edited by T. Okada, K. Suzuki, and Y. Kawamura (Springer Singapore, Singapore, 2021) pp. 51–63.

[3] P. Pfeffer, L. Wachter, D. Hoffmann, M. Bastian, and G. Schober, *Multiple-flash shearography–a new NDT method for reducing thermal stresses during the inspection process,* in *10th International Symposium on NDT in Aerospace, Oct 2018, Dresden, Germany.*

[4] N. Tao, A. G. Anisimov, and R. M. Groves, *Spatially modulated thermal excitations for shearography non-destructive inspection of thick composites,* in *Optical Measurement Systems for Industrial Inspection XII,* Vol. 11782, edited by P. Lehmann, W. Osten, and A. A. G. Jr., International Society for Optics and Photonics (SPIE, 2021) p. 117820V.

[5] T. L. Bergman, F. P. Incropera, D. P. Dewitt, and A. S. Lavine, *Fundamentals of heat and mass transfer* (John Wiley & Sons, 2017).

[6] R. Krankenhagen, T. Worzewski, and C. Maierhofer, *Cooling-down of thermal thick probes after flash excitation – a measure for the real energy density?* Infrared Physics & Technology **72**, 258 (2015).

[7] J. P. Müller, G. Dell'Avvocato, and R. Krankenhagen, *Assessing overload-induced delaminations in glass fiber reinforced polymers by its geometry and thermal resistance,* NDT & E International **116**, 102309 (2020).

6

[8]   Y. Li, W. Zhang, Z. Yang, J. Zhang, and S. Tao, *Low-velocity impact damage characterization of carbon fiber reinforced polymer (CFRP) using infrared thermography,* Infrared Physics & Technology **76**, 91 (2016).

[9]   H. Cheng, J. Gao, O. L. Kafka, K. Zhang, B. Luo, and W. K. Liu, *A micro-scale cutting model for UD CFRP composites with thermo-mechanical coupling,* Composites Science and Technology **153**, 18 (2017).

[10] D. T. Goto and R. M. Groves, *Error analysis of 3D shearography using finite-element modelling,* in *Optical Micro- and Nanometrology III*, Vol. 7718, edited by C. Gorecki, A. K. Asundi, and W. Osten, International Society for Optics and Photonics (SPIE, 2010) p. 771816.

[11] A. G. Anisimov, M. G. Serikova, and R. M. Groves, *3D shape shearography technique for surface strain measurement of free-form objects,* Applied Optics **58**, 498 (2019).

[12] N. Tao, A. G. Anisimov, and R. M. Groves, *Shearography data for deep defect detection and characterization in thick GFRP laminates,* (2022).

[13] M. Krause, F. Roland, and C. Cau, *Ramsses–realisation and demonstration of advanced material solutions for sustainable and efficient ships,* in *Proceedings of 7th Transport Research Arena TRA* (2018) pp. 44–48.

6

7

SHEAROGRAPHY NDT OF A COMPOSITE SHIP HULL SECTION

This chapter presents an experimental study about performance validation of shearography NDT on full-scale structures and for realistic defects and damage. The main aim of the research in this chapter is to bring the shearography technique out of the laboratory and to inspect a composite ship hull section (6 m tall, 2.5 m wide) in a shipyard, which addresses RQ4 - 'What is the efficacy of the shearography inspection system for full-scale structures in the in-service environment'.

The composite ship hull section has been subjected to multiple impacts in the RAMSSES project to mimic a realistic heavy crash. For the on-site shearography inspection at Damen Shipyards, most of the results are achieved with thermal loadings, a mechanical loading is also evaluated for shearography NDT when inspecting the main impact location. Thermal loadings are performed by using three halogen lamps, each operating at full electrical power. The mechanical loading is applied by a 7-ton metal block on the top deck of the structure, representing the landing of a medium helicopter. Before the on-site inspection, a preliminary study has been performed in the lab on a representative sandwich panel with similar impact damage using thermal loading. In this chapter, experimental results on the inspection of the large-scale composite ship hull and the test sandwich panel are reported.

7.1. INTRODUCTION

THE objective of this study is to validate the performance of shearography NDT on full-scale structures and for realistic defects in the in-service environment, specifically a large-scale composite ship hull section that had been subjected to multiple impacts. Different loading scenarios including thermal loadings as well as a mechanical loading were performed for shearography NDT to evaluate their corresponding efficacies in defect detection. Before the on-site inspection, a preliminary study was performed on a representative sandwich panel with similar impact damage using thermal loading. Section 7.2 presents the preliminary analysis on the test sandwich panel. Section 7.3 reports the on-site inspection of the composite ship hull. These experiments were performed over a period time of 1 week in 07/2021. The tested composite hull section and the testing campaign are introduced in Section 7.3.1. The shearography system for this on-site inspection is presented in Section 7.3.2. The inspection results with thermal loadings and a mechanical loading are reported in Sections 7.3.3. A comparison between thermal loading and mechanical loading on thick composite inspection with shearography is given in Section 7.3.4.

7.2. PRELIMINARY STUDY ON A TEST SANDWICH PANEL

7.2.1. TEST SANDWICH PANEL

Prior to the on-site inspection of the composite ship hull section at Damen Shipyards, a representative sandwich panel with a similar structure, material composition, and impact damage was inspected in the lab environment. This sandwich panel (Figure 7.1) is 1.5 m tall and 1.0 m wide and the thickness of the panel is about 66 mm (glass-fibre laminate skins: each 3 mm thick; foam core: 60 mm thick). It was impacted on the center of the front side (Figure 7.1(a)). The impact damage is visible from the front but non-visible from the back (Figures 7.1(a) and 7.1(b)) with the naked eye. The diameter of the impact area was measured and found to be 100 mm. However, the specifics on the impact test and the material properties of the panel are no longer available.

This test sandwich panel was used to verify the efficacy of the out-of-plane shearog-
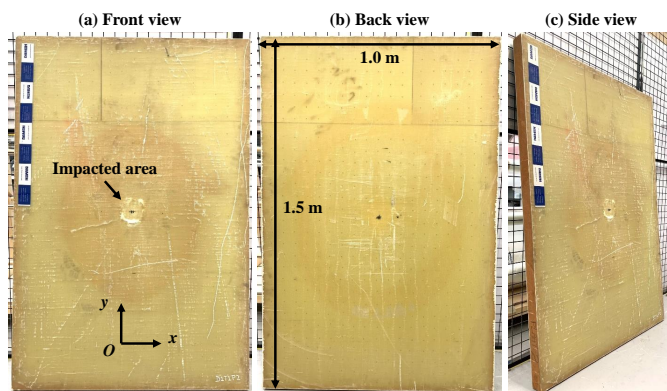

Figure 7.1: Test sandwich panel with GFRP skins and foam core. (a) Front (b) Back (c) Side

raphy instrument for the detection of realistic defects and damage in thick composites, and also to determine suitable parameters including heating intensity, heating time and shearing distance for the following on-site inspection. For that, both the front and back surfaces of the sandwich panel were inspected for evaluation. Two halogen lamps were used to apply thermal loading to the test specimen.

7.2.2. INSPECTION RESULTS WITH THERMAL LOADING

During the experiments, the Torus 532 laser source was operating at 200 mW for illumination. The distance between the panel and the shearography instrument was 1.6 m. Different thermal loading schemes including continuous and periodic heating scenarios(5-10 min) were tested on this panel. Shearing distances varied in the range 6-12 mm in the x-direction. The five-step phase-shifting method was adopted for its accuracy. Phase compensation by using polynomial fitting was performed to improve defect detection.

Figure 7.2 shows the inspection results of the test sandwich panel. The photographs showing the fields of view (FOVs) of the shearography camera for the front and back surfaces of the test panel are shown in Figures 7.2(a) and 7.2(b), respectively. Figure 7.2(c) shows the compensated defect-induced phase map (DIP) with the front surface, which was obtained with a shearing distance of 11.63 mm and continuous heating of 300 s. Figure 7.2(d) shows the compensated map with the back surface, which was obtained with a shearing distance of 6.51 mm and periodic heating of 10 cycles of 60 s. These results were achieved from the measurements during cooling.
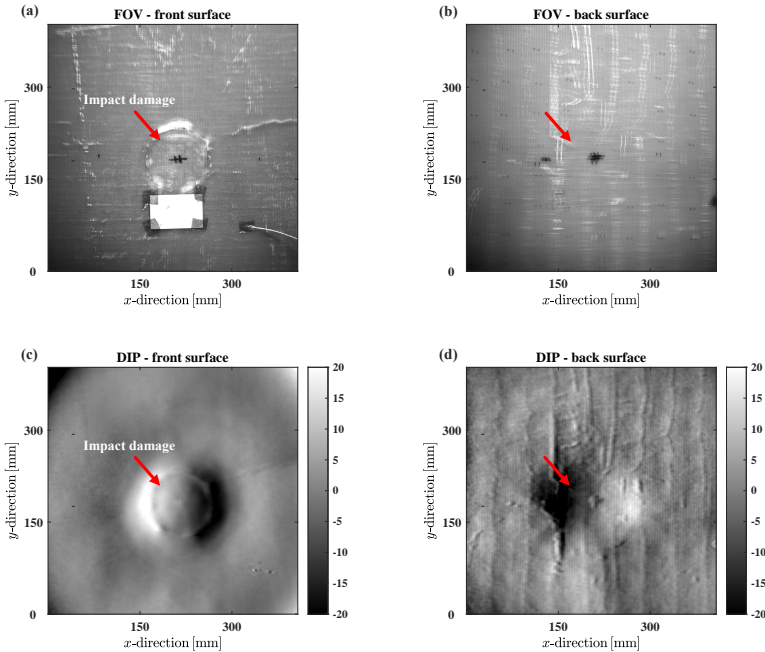

Figure 7.2: Inspection results for the front and back surfaces: (a) The photography shows the FOV of the front surface. (b) The photography shows the FOV of the back surface. (c) Compensated phase map (DIP) with the front surface. (d) Compensated phase map (DIP) with the back surface.

Impact damage can be clearly detected from both surfaces (Figures 7.2(c)-7.2(d)). For the inspection from the front surface. The visible damage area in Figure 7.2(a) is 100 mm in diameter, while in the compensated DIP map in Figure 7.2(c) the damaged area is larger (about 150 mm). This could indicate more defects and damage (e.g., delaminations and debonding) exist beneath the impacted region in the front skin. For the inspection from the back surface. The impact area is non-visible from the back with the naked eye (Figure 7.2(b)), but there is also damage that is detected in the compensated phase map (Figure 7.2(d)). This damage could be located in the back skin due to the impact. The size of the damage is measured to be about 125 mm, which is also larger than the impact area on the front. In addition, a number of short vertical lines are also shown in the compensated phase map (Figure 7.2(d)). Those vertical lines could be related to surface stratches on the panel, which can be also seen in the photography in Figure 7.2(b).

Figure 7.3 shows a comparison of inspection results between during heating and during cooling. The inspection was from the back surface, where the results were achieved with a shearing distance of 6.51 mm and periodic heating of 15 cycles of 30 s. Figure 7.3(a) is the compensated phase map obtained during cyclic heating and Figure 7.3(b) is the compensated phase map during cooling.
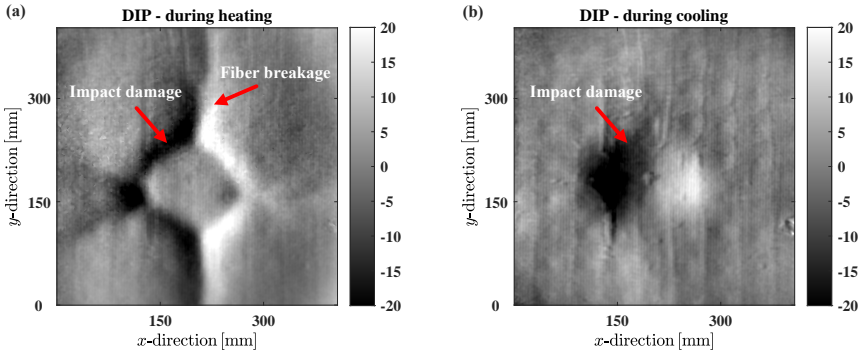
Figure 7.3: Inspection results from measurements (a) during cyclic heating and (b) during cooling, respectively. Inspection from the back surface. [Phase unit in radian]

It shows that the result obtained during heating (Figure 7.3(a)) can reveal more signatures of defects and damage. Apart from the impact damage that is clearly detected, additional fibre breakages of 50-100 mm in length are also revealed in the compensated phase map. While only the impact damage is revealed in the compensated phase map obtained during cooling (Figure 7.3(b)). This highlights the value of performing measurements during heating.

In short, this preliminary study shows that impact damage in this thick sandwich panel can be reliably detected with minutes of heating (temperature rise of about several to a dozen degrees Celsius) and with a 6-12 mm shearing distance. These results provide valuable guidance regarding the selection of suitable experimental parameters including heating time and shearing distance for the followed on-site inspection.

7.3. ON-SITE INSPECTION FOR THE COMPOSITE SHIP HULL

7.3.1. COMPOSITE SHIP HULL DEMONSTRATOR AND TESTING CAMPAIGN

An overview of the composite ship hull section is shown in Figure 7.4. The ship hull section is the RAMSSES demonstrator [3, 4] at Damen Shipyards. The structure is made from FRP laminate skins and foam cores. The dimensions are about 6 m in height and 2.5 m in width. The thickness of the hull shell varies from about 100 mm at the top to about 270 mm at the bottom. This RAMSSES demonstrator shows the material and structural complexity of real-scale ship structures, which poses great challenge to the inspection. It should be noted that only limited technical specifications for the demonstrator can be provided for company confidentiality reasons.
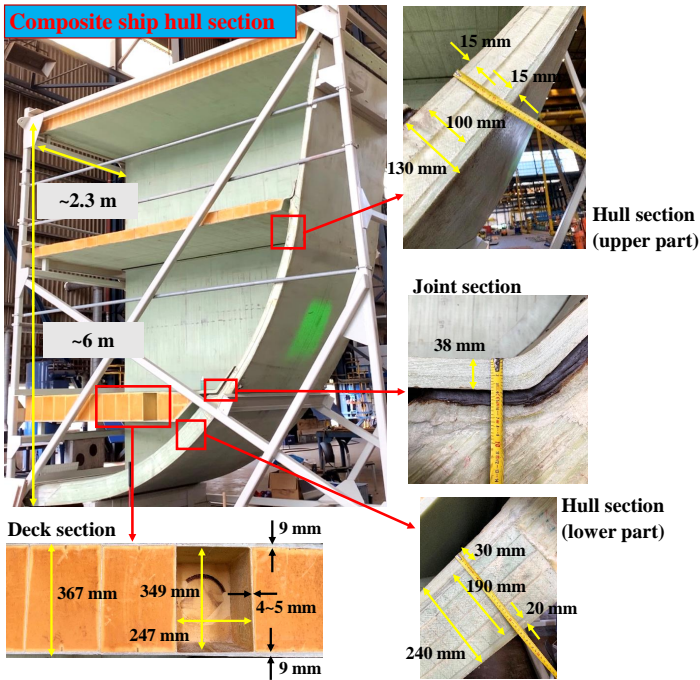
Figure 7.4: The composite ship hull section

Before shearography inspection, multiple impact tests (video available at [5]) surpassing helicopter emergency landing loads have been performed on the hull shell and its composite helicopter deck for proving the resilience of composites to harsh marine environments. The impacted area on the hull shell can be seen in Figure 7.5(b).

The region of interest of the composite ship hull section at Damen Shipyards is shown in Figure 7.5. First, a whole-field inspection on the hull shell was performed (Figure 7.5(a)) for an overall evaluation. A total area of about 1500×900 mm^2 was inspected by stitching the inspection of six fields of view (FOVs) of 600×600 mm^2 (Figure 7.5(a), two in the vertical direction by three in the horizontal with about 20% overlap for stitching). The stitching was done manually by aligning the same features in the overlap area. Each FOV was inspected by repeating the same thermal loading. Second, a detailed inspection

of the impacted area was performed for a more in-depth study on impact damage in the thick composite structure. Both thermal and mechanical loadings were adopted for shearography NDT to evaluate their corresponding efficacy in defect detection. It can be noted that for thermal loading, the measurements during heating failed to produce reliable phase maps due to hot airflow and speckle decorrelation, so only measurements during cooling are presented in the next section.
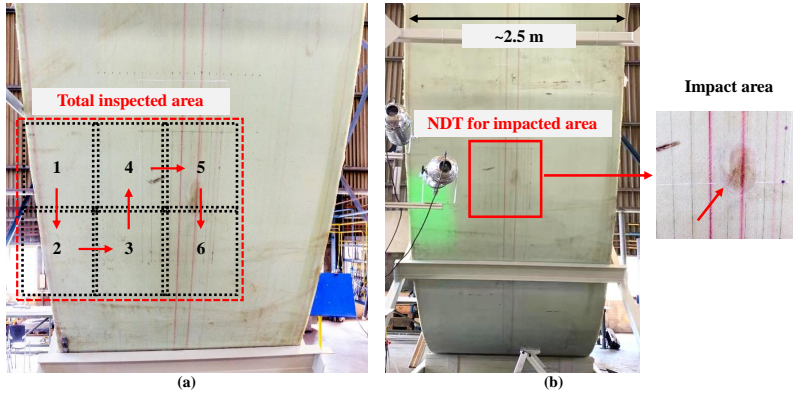

Figure 7.5: Testing campaign at Damen Shipyards. (a) Total inspected area of about 1500 by 900 mm by stitching 6 adjacent fields of view. (b) Detailed inspection for the impacted area

7.3.2. Shearography system for the on-site inspection

The experimental shearography inspection system with a focus on out-of-plane deformation is shown in Figure 7.6. The FOV of the shearography camera sensor is about 600×600 mm^2. A Thorlabs bandpass filter (FLH532-4, center wavelength of 532 nm and bandwidth of 4 nm, transmission > 90%) was used to transmit laser light while blocking other unwanted wavelength bands of light (e.g., sunlight). The bandwidth of 4 nm was chosen to maximise the amount of laser light into the camera. During the inspection, the shearography instrument (Figure 7.6(a)) was fixed on a motorized rigid platform. By adjusting the rigid platform, scanning in both horizontal (x-direction) and vertical (y-direction) directions could be achieved, enabling a large-area inspection.

Various thermal loadings and a mechanical loading were implemented for the shearography inspection. Thermal loading (Figure 7.6(b)) was performed by three halogen lamps, each operating at full electrical power 1000 W. The effective surface temperature during heating was monitored with a FLIR A655 thermal infrared (IR) camera. Mechanical loading (Figure 7.6(c)) was applied by a 7-ton metal block on the top deck of the structure, lifted by a gantry crane, which represented the landing of a medium helicopter.

A three-step phase-shifting algorithm was selected for thermal loading scenarios due to its fast speed (2.8 s per phase-shifting cycle) and a five-step phase-shifting algorithm was chosen for the mechanical loading scenario due to its resulting accuracy [6, 7]. The shearing distance of about 9 mm was determined experimentally to produce reliable phase maps for defect detection, which corresponded to the preliminary results from the representative sandwich panel with similar impact damage.
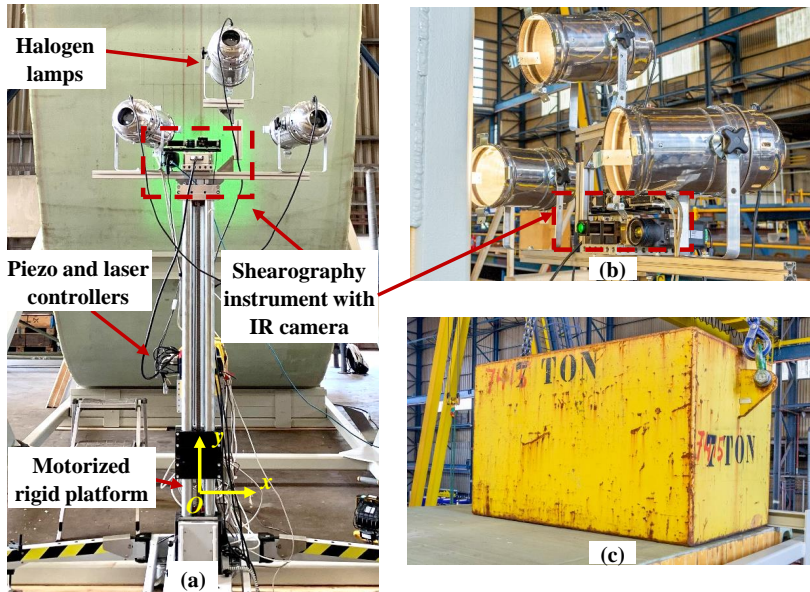
Figure 7.6: Experimental out-of-plane shearography inspection system: (a) Shearography instrument mounted on a motorised rigid platform; (b) Thermal loading with three halogen lamps; (c) Mechanical loading with a 7-ton metal block on top deck.

7.3.3. SHEAROGRAPHY INSPECTION RESULTS

WHOLE-FIELD INSPECTION OF THE HULL SHELL WITH THERMAL LOADING

For the whole-field inspection of the hull shell. The six FOVs (Figure 7.5(a)) were inspected one by one by repeating the same thermal loading of 240 s heating. The selection of the heating time was based on the preliminary analysis in Section 7.2. The y-shearing direction was determined experimentally due to its efficacy in defect detection. During the inspection, the surface temperature increase varied 8-15 °C depending on the setup configuration, which did not pose any risk of degradation of the polymeric matrix in the ship hull wall. During the cooling of the structure, sets of phase-shifted speckle interferograms were continuously recorded, later processed and manually stitched together. Their total build-up results in phase maps of the whole area that indicate the evolution of the out-of-plane displacement derivative with the shearing direction.

The resultant phase map that was stitched for the six FOVs is shown in Figure 7.7. The stitching process could be further improved by considering the shape of the surface, the positions of the camera and the laser [7]. There is a suspicious area identified on the top left of the resultant phase map in Figure 7.7 (marked by a red ellipse), however, the presence of other defects and damage is not clear because global deformation is large (±80 rad). To extract defect-induced deformation from global deformation, a phase compensation by using polynomial fitting was performed for each FOV. Then a manual stitching was done to obtain the stitched compensated phase map for defect detection. This stitched compensated phase map (Figure 7.8) reports the presence of damage in the structure. Three suspicious areas are identified, which can be related to skin-to-

core debonding (A1), surface damage due to bouncing of the impactor head on the hull wall (A2) and the main impact location (A3). The damage in the impacted region is not obvious, this can be because its position is close to the edge of the FOVs no.5 and no.6 (Figure 7.5(a)), which makes it difficult to extract actual defect deformation.
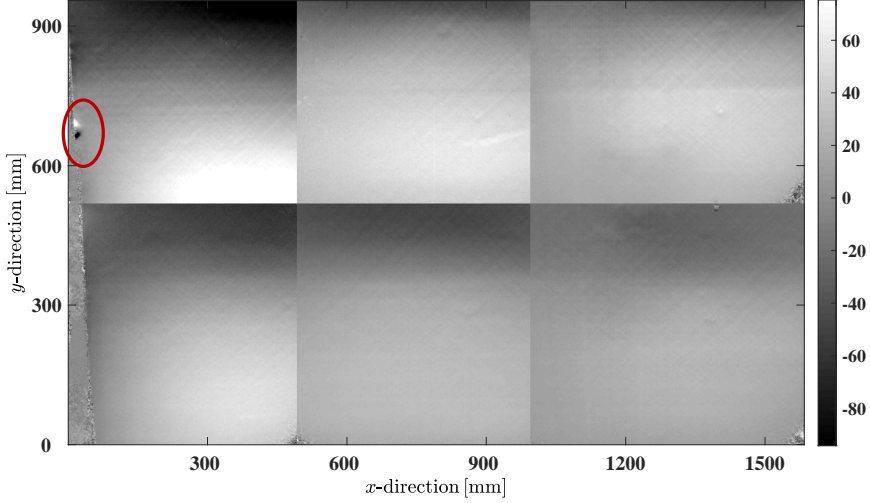
Figure 7.7: Resultant phase map of the whole area by shearography with thermal loading (stitched for six FOVs), a suspicious area marked by a red ellipse. [Phase unit in radian, 1 rad ≈ 4.7 $\mu\varepsilon$]
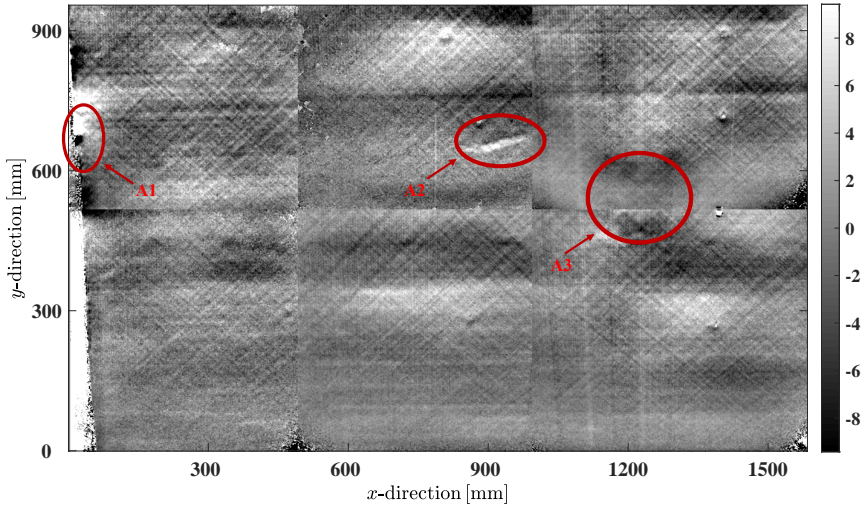
Figure 7.8: Stitched compensated phase map of the whole area by shearography with thermal loading. A1 - skin-to-core debonding, A2 - The scratch left by the impactor on the hull wall due to bouncing, A3 - impact damage of interest. [Unit of phase is radian, 1 rad ≈ 4.7 $\mu\varepsilon$]

For the detailed inspection of the impacted area. A thermal loading and a mechanical loading were evaluated for shearography NDT. For thermal loading, the recording and processing of the speckle interferograms were the same as in the whole-field inspection. For mechanical loading, as explained in Section 7.3.2, it was applied by lifting and placing a 7-ton metal block on the top deck of the hull section, resulting in bending outwards in the vertical direction (y-direction in Figure 7.6). Sets of phase-shifted interferograms were recorded at the end of each loading step. The y-shearing direction was adopted as the vertical compression was expected to be dominant. The processing of the recorded phase-shifted interferograms yields the overall mechanical response of the structure.

The results of the detailed inspection of the impacted area are shown in Figure 7.9. The compensated phase map for thermal loading (Figure 7.9(b)) reveals the presence of the strain anomalies due to the impact damage caused directly under the impactor head (indicated by the red arrow in Figure 7.9(b)). The result for mechanical loading (Figure 7.9(c)) also reveals the presence of impact damage in the same region. The strain anomalies found are likely to include delaminations and possible skin-to-core debonding, indicating true local stress concentrations that may lead to failure at this location.
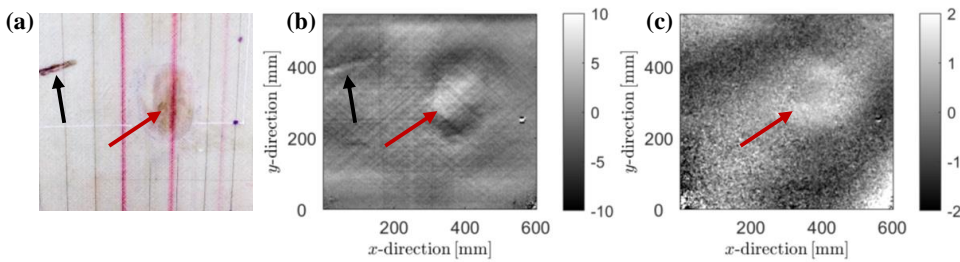
Figure 7.9: Detailed inspection of the impact region. (a) The inspection area with multiple impacts. (b) The compensated phase map with thermal loading. (c) The compensated phase map with mechanical loading. [Unit of phase is radian, 1 rad ≈ 4.7 $\mu\varepsilon$]

7.3.4. COMPARISON OF THERMAL AND MECHANICAL LOADINGS FOR NDT

A comparison of thermal and mechanical loadings for shearography NDT is given here. As shown in Figure 7.9, the same defect is detected by both thermal and mechanical loadings. This shows the reliability of the shearography inspection. It can be noted that the inspection result from mechanical loading (Figure 7.9(c)) seems to be blurry, which is likely to be due to the rigid body motion of the hull section induced by the loading procedure. In addition, the black arrow in Figure 7.9(b) could indicate some skin matrix damage that may have been caused by the scraping of the impactor against the hull wall during the bouncing of the impactor head after actual impact (see also black arrow in Figure 7.9(a)).

For thermal loading, it is easy to apply, and loading parameters such as intensity and time of heating are easy to control in industrial environments. Uniform heating can be useful to inspect a large structure. Nevertheless when inspecting deep defects, e.g. deeper than 20 mm, more time is required for heat to propagate (tens of minutes). It can be

noted that heating lamps can cause hot airflow during heating and cooling which should be treated carefully in experiments.

For mechanical loading, it is possible to reveal critical defects only and to avoid trivial defects if the test object is loaded in a similar stress state to the actual working load in service [8]. One possible advantage can be fast measurement time as heat propagation is not needed. However, the deformation of the test object is difficult to estimate in experiments. Suitable loading increments need to be determined for shearography. The loading process usually introduces large rigid body movements that may cause unfavorable speckle decorrelation in shearography. This was observed during the inspection. The unloading process is found to be acceptable in experiments for producing reliable phase maps. The challenge is to develop an adequate mechanical loading scenario to obtain the detectable defect-induced strain. For this, prior numerical modelling can be done to give an estimation of the needed load for expected critical defects.

7.4. CONCLUSIONS

THE experimental study in this chapter demonstrates that shearography can be a suitable NDT technique for full-scale structures in an industrial environment and for realistic defects and damage. The strain values obtained from the shearography experiments can be potentially used to determine the remaining useful life of the test object and as a reference for future inspections. For the ship application, representative impact from the RAMSSES project created a 100 mm in diameter impact area, no further information regarding defect depth or surrounding damage was known. It is beneficial to continue the inspection of this composite ship hull section with other NDT techniques to support the interpretation of shearography results. RQ4 is partially answered in this chapter.

For the preliminary study of the representative sandwich panel, impact damage can be reliably detected from both the front and back surfaces of the test sandwich specimen. These inspection results also highlight the value of measurements during heating to be performed. Besides, suitable parameters including heating time and shearing distance were experimentally determined, providing valuable guidance for on-site inspection. Those are important parameters for successful shearography inspection.

For the on-site inspection of the composite ship hull section, the results show that the shearography technique can realise large-area inspection. Both thermal and mechanical loadings were evaluated for shearography NDT of the impacted area on the hull shell. Compensated phase maps from the two loadings both identified the presence of impact damage successfully. Besides, the comparison between thermal and mechanical loadings for NDT indicates that uniform heating can be useful for inspecting a large structure with shearography, however significant time, e.g., 10 to 20 minutes, can be needed for heat to propagate when inspecting deep defects. With mechanical loading it is possible to reveal critical defects directly and fast, nevertheless, it is necessary to prevent excessive rigid body movements to avoid speckle decorrelation.

REFERENCES

[1] N. Tao, A. G. Anisimov, M. Elenbaas, and R. M. Groves, *Shearography non-destructive testing of a composite ship hull section subjected to multiple impacts,* in *Proceedings of the 20th European Conference on Composite Materials: Composites Meet Sustainability*, edited by A. Vassilopoulos and V. Michaud (2022) pp. 469–474.

[2] P. A. Ochôa, H. den Ouden, M. Hagenbeek, N. Tao, A. G. Anisimov, and R. M. Groves, *Towards complete diagnosis of structural damage in a real-scale full-composite ship hull section subjected to high-energy impacts by acoustic emission monitoring and laser shearography inspection,* Under review (2023).

[3] M. Krause, F. Roland, and C. Cau, *Ramsses–realisation and demonstration of advanced material solutions for sustainable and efficient ships,* in *Proceedings of 7th Transport Research Arena TRA* (2018) pp. 44–48.

[4] S. Paboeuf, A. de Bruijn, F. Evegren, M. Krause, and M. Elenbaas, *A "fast track to approval" process for innovative maritime solutions,* in *Practical Design of Ships and Other Floating Structures*, edited by T. Okada, K. Suzuki, and Y. Kawamura (Springer Singapore, Singapore, 2021) pp. 51–63.

[5] Damen, *Impact testing RAMSSES demonstrator, https://vimeo.com/522716506,* (2021).

[6] D. Francis, R. P. Tatam, and R. M. Groves, *Shearography technology and applications: a review,* Measurement Science and Technology **21**, 102001 (2010).

[7] A. G. Anisimov, M. G. Serikova, and R. M. Groves, *3D shape shearography technique for surface strain measurement of free-form objects,* Applied Optics **58**, 498 (2019).

[8] Y. Hung, *Shearography for non-destructive evaluation of composite structures,* Optics and Lasers in Engineering **24**, 161 (1996).

7

8

CONCLUSIONS AND RECOMMENDATIONS

8.1. SUMMARY OF MAIN CONCLUSIONS

WITH the increasing use of thick composites in safety-critical applications in the marine, wind energy and aerospace industries, the inspection of thick composite materials becomes an urgent challenge. The goal of the thesis is to develop shearography method with thermal excitations for the inspection of thick composites (50-60 mm thick and more) and for pushing reliable detection and characterisation towards deep defects. This research also aims to bring the shearography technique out of the laboratory for real industrial applications. Hence, FEM-assisted shearography with spatially and temporally modulated heating methods has been proposed and developed, enabling quantitative, predictable and safe inspection of thick composites. The detectable defect depth can be up to 25 mm by using the developed shearography method. This research makes a step towards the comprehensive understanding of the shearography NDT of composite structures of significant thickness. The main conclusions and findings are summarised as follows:

8.1.1. DETECTION CAPABILITIES AND INSPECTION LIMITATIONS OF SHEAROGRAPHY NDT FOR THICK COMPOSITES

This addresses RQ1 - 'What are the defect detection capabilities, inspection limitations and new possibilities of shearography NDT for thick composites'. RQ 1 is fully answered in Chapter 4.

The first step of this thesis work was to study defect detection capabilities and inspection limitations of thick composite inspection with shearography. To assist this study, a thermal-mechanical model of the thick composite was developed using equivalent thermal and mechanical properties. The model was evaluated by temperature/thermal and strain/mechanical tests and showed a good agreement in transient temperature and in strain maps between simulations and experiments. The established FEM model can serve as a predictive model, e.g., to predict the behaviour of the thick composite and to determine a suitable loading intensity and loading time for reliable defect detection. The thresholds for the defect-induced phase and the corresponding defect-induced deformation, at about three times of the STD of the background signals (defined in Section 4.4.2), are determined for shearography testing. Besides, the effect of mechanical boundary conditions on defect-induced deformation was studied by FEM. The results showed that mechanical boundary conditions have a significant influence on shearography fringe pattern. As for the defect-induced deformation during cooling, their influence on deep defects is limited, which may indicate that for thick composite inspection, the influence of mechanical boundary conditions on defect detection capabilities with shearography is limited in the case that the overall deformation can be predicted and removed properly.

From the conducted numerical and experimental investigation, it is clear that shearography is a promising NDT method for thick composite inspection. It is possible to detect deeper defects than the state of the art and general practice in the industry (in shearography applications) when the excitation and boundary conditions are properly characterised and taken into account, combining with careful compensation of the overall deformation. In general, the complexity in a blind detection lies in the fact that it is unknown what and when (excitation) to apply. FEM guidance gives a clear expected reference while experiments may have multiple uncertainties and influencing factors.

Based on the FEM and experimental results, defects at 5-20 mm depth in the thick GFRP laminate can be detected successfully with shearography. The knowledge achieved by answering RQ1 can provide valuable instruction for the inspection of thick composite structures.

8.1.2. SPATIALLY MODULATED HEATING FOR SHEAROGRAPHY NDT

This addresses RQ2 - 'How can spatially modulated heating be developed for improving thick composite inspection with shearography'. RQ 2 is fully answered in Chapter 5.

The developments of novel thermal excitation methodologies open new possibilities for the inspection of thick composites with shearography. The second step of this thesis work was therefore to study and develop spatially modulated heating for shearography NDT. This research focused on the detection of the defect at 25 mm depth. The heat flux distribution on the specimen surface was also taken into consideration, a factor which is rarely reported in shearography inspection. Both global heating and spatially modulated heating were evaluated experimentally and modelled numerically. Results shows that spatially modulated heating has one or a combination of the following advantages: energy concentration, high defect signal, deeper defect detection, improved edge detection of a defect, and potentially fast inspection.

Nevertheless, due to non-uniform heating and the complex global deformation with spatially modulated heating, additional measurements of a similar and defect-free reference sample are currently necessary to compare that of a defective plate. Besides, the efficacy of shearography NDT of the deeply buried defect (at 25 mm depth) in the thick composite laminate can vary when selecting different reference states, in which the issue of fibre-related deformation on deep defect detection should be treated carefully when applying thermal loading. A suggested rule for selecting the suitable reference states (as well as signal states) is, to reduce the background phase (e.g. fibre-related) as much as possible while keeping the defect signal high. In this research this was achieved by selecting the reference status as 40% of the total heating time.

It can be noted that the efficacy of defect detection by the proposed spatially modulated heating can vary greatly depending on the heating positions. The detection is expected to be more efficient as the heating position is close to the defect. However, in a practical industrial inspection the location of a defect usually remains unknown beforehand. To cope with this problem, a combination of global heating and spatially modulated heating for shearography NDT can be a reasonable solution for the detection of deep defects, that is, first applying global heating for overall searching of suspicious areas, and then applying spatially modulated heating for detailed characterisation of deep defects.

8.1.3. TEMPORALLY MODULATED HEATING FOR SHEAROGRAPHY NDT

This addresses RQ3 - 'How can temporally modulated heating be developed for improving thick composite inspection with shearography'. RQ 3 is fully answered in Chapter 6.

The next step of the thesis work was to develop temporally modulated heating for shearography NDT. The controlled surface temperature (CST) heating method was proposed and adopted for thick composite inspection with shearography, enabling the selection and control of the maximum surface temperature. This work makes a step forward in

safe shearography inspection for deep defect characterisation in thick composites where overheating may cause damage.

The influence of various heating scenarios on defect detection and defect behaviour characterisation was investigated by a numerical and experimental study, including a new CST heating method and two conventional heating methods. The experimental and numerical results indicate that for GFRP laminate materials, defects at 15 and 20 mm depths can be reliably detected with full-field CST heating. However, the effect of the CST decreases as the defect depth increases, while the defect at 25 mm depth is close to the detection sensitivity. More time (e.g., a dozen to dozens of minutes of heating) is needed for heat to propagate and interact with defects deeper in the structure. The background deformation from a healthy region was measured to serve as a baseline for the detection of defects in thick composites. This study also provides insight for implementing an efficient inspection in terms of the inspection duration and the number of datasets, e.g., only two sets of interferograms during heating and cooling are needed to be recorded, producing the highest DIP value for defect detection and characterisation.

8.1.4. EFFICACIES OF SHEAROGRAPHY INSPECTION SYSTEM ON FULL-SCALE COMPOSITE STRUCTURES FOR THE IN-SERVICE ENVIRONMENT

This addresses RQ4 - 'What is the efficacy of the shearography inspection system for full-scale structures in the in-service environment'. RQ 4 is partially answered in Chapter 7.

The final step of this thesis work was for performance validation on real-scale ship structures in industrial environments. The experimental study of the composite hull section demonstrates that shearography can be a suitable NDT technique for the in-service inspection of full-scale structures with realistic defects and damage.

Compensated phase maps from thermal and mechanical loadings both identified the presence of impact damage successfully. Uniform heating can be useful for inspecting a large structure with shearography in the industrial environment, however significant time, e.g., 10 to 20 minutes, can be needed for heat to propagate when inspecting deep defects. With mechanical loading it is possible to reveal critical defects directly and fast, nevertheless, one precaution is to avoid excessive rigid body movements. The unloading process is found to be acceptable in applying mechanical loadings for producing reliable phase maps.

8.2. RECOMMENDATIONS FOR FUTURE WORK

THE present thesis advances shearography inspection for thick composite structures to improve structural safety and integrity. However, long road as it is, more efforts are required to push shearography for NDT of thick composites further for practical industrial applications. The main recommendations regarding future work are as follows:

(1) To assess the performance of a shearography system, a deeper understanding about loading parameters and environmental factors (e.g., in a shipyard environment including vibrations and temperature effects) on its efficacy and accuracy is required. Future work can include optimization of loading parameters for shearography to improve the detection of defects in thick composites and exploring the possibilities of monitoring both in- and out-of-plane deformation for defects such as delaminations and fibre breakage. It can

be noted that the conclusions related to the effect of mechanical boundary conditions on defect-induced deformation were made based on three modelling cases and for a relatively short period of heating (about 3 min). So more boundary conditions (e.g. simply supported and cantilever) and more experiments need to be considered.

(2) In the study of spatially modulated heating on shearography NDT, an elliptical shape pattern was used with the proposed SMH method, as a rational result of the illumination setup with the Fresnel lens and heating at an angle. Other shapes or other types of SMH, e.g. by using multiple Fresnel lenses and by adjusting the distances between the Fresnel lenses, lamps and the test structure, can be investigated in the future. Besides, developing some advanced algorithms to extract defect-induced deformation can be a promising subject for future work. For example, phase compensation by combining analytical solutions of thermal deformation or prediction by FEM. A digital twin of the structure can be useful for extracting the defect signal. Fourier transform analysis and/or principal component analysis may also be helpful in filtering fibre-related deformation and obtaining defect deformation. In addition, the healthy regions of the structure can be used for the reference measurements.

(3) The work of controlled surface temperature heating can also be applied for the inspection of structures such as polymeric coatings and paintings where the control of maximum surface temperature is critical. This experience was gained from the study of the structural inspection of Rembrandt's Night Watch [1, 2]. Future work can be to study the influence of various heating times of CST and amplitudes of the controlled surface temperature on defect detection and characterisation. It is also interesting to adopt the developed modulated thermal loading schemes to inspect composite materials such as carbon fibre-reinforced polymers, hybrid carbon and glass fibre composites, and natural fibre composites. Besides, material characterisation, e.g., by using X-ray CT and scanning electron microscope (SEM) may be helpful to further understand thermal and mechanical responses (i.e., temperatures and strains) from a micro-structure point of view.

(4) Developing other loadings e.g., mechanical or vibration loadings that are alternatives to thermal loading for shearography could also be a promising direction. For example, for mechanical loading, it can be interesting to determine suitable mechanical loading increments for defect detection. This approach could also be explored by applying combined thermal-mechanical loading schemes to improve defect detection with shearography.

REFERENCES

[1] N. Tao, A. G. Anisimov, E. van Duijn, L. Vos, I. Steeman, K. Keune, P. Noble, and R. M. Groves, *Assessment of the structural integrity of the wax-resin lined canvas paintings with 3D shape shearography,* Manuscript in preparation (2023).

[2] N. Tao, A. G. Anisimov, E. van Duijn, L. Vos, I. Steeman, K. Keune, P. Noble, and R. M. Groves, *Application of shearography with thermal loading for the structural inspection of Rembrandt's Night Watch,* in *Optics for Arts, Architecture, and Archaeology (O3A) IX,* International Society for Optics and Photonics (SPIE, 2023).

ACKNOWLEDGEMENTS

Many years ago when I was a child, my parents once asked me what I wanted to do when I grew up. I said simply with innocent confidence: "I want to go to college, get a PhD, and become the most knowledgeable person in the country". I was perhaps six years old or even younger at that time and didn't know what a PhD really means. It has been long years since then. At this moment in my life, after nearly five years of the PhD research, I would say the PhD is more a journey to experience than a degree to obtain. There are all kinds of things keeping popping up during the PhD journey including mixed emotions and feelings in the difficult times. I couldn't complete my PhD without the help and support of many people.

First of all, I would like to thank my daily supervisor and co-promotor, Dr. Andrei Anisimov. Thank you for helping me define my research and for guiding me to make progress step by step throughout my PhD. You are always a very responsible, professional and helpful supervisor. Thank you for believing in me and for pushing me back on my way when I was lost during the difficult times. Thank you also for keeping me informed and helping me get opportunities such as obtaining covid contract extension, participating in the Night Watch inspection and so on. I'd like to recall a few special moments here. The first moment is during the Faculty Christmas Party at SAM|XL when you made a metaphor for my PhD research by striking a long iron nail little by little. This long iron nail is still kept in my office as a reminder of my goal. The second is that time when you brought the 'bible' book of shearography to me and pointed out the page on experiments with a significantly large shearing distance on two objects, you commented that the studies like those (with bold,/amazing/great ideas) were what we should do. The third is the afternoon of the day in the office, you told me that you had just got the promotion to assistant professor. If I may say, it is my honour to be your first PhD, and I wish you more and more great successes to come in the future.

Secondly, I would like to thank my promotor Dr. Roger Groves. Thank you for trusting me and giving me the freedom to explore and take my own decisions during the research. Thank you also for being patient with my progress. I have always liked our discussions in the office and in the lab. Your valuable advice and feedback over the years have helped me a lot. I also learned a lot from the way how you review my papers and thesis, the style how you work on your own rhythms and so on. Moreover, I have really enjoyed working close with you in the practicals in the master course, at Damen Shipyards and in the Rijksmuseum. All these experiences are special to me which will keep me motivated in the future research.

In the meanwhile, I would like to acknowledge my promotor Prof. Rinze Benedictus. Thank you for giving me the opportunity to pursue a PhD in the department. Thank you for providing valuable discussions and insights during our meetings. I really appreciate your support and feedback through the PhD.

Next I'd like to thank our Secretary Gemma van der Windt. Thank you for helping

me with the paperwork on my visa and extension. Thank you for your all-round support during my PhD including scheduling my Go/No-Go meeting and Yearly Progress meetings. You make my PhD life go more smoothly.

Thank you to the OPZuid project partners - Marcel Elenbaas from Damen Shipyards, Jon Huizinga and Peter Troost from TiaT, Alena Belitskaya from DTIS and Luigi Fazzi from TU Delft. Special thanks go to Marcel Elenbaas and Athanasios Droutsas for the materials and the industrial feedback.

Thank you to all the technicians and staffs in the DASML and DEMO. Thank you Berthil, Marlies, Johan, Durga, Alexander, Dave, Chantal, Victor and Fred for their help in material and NDT experiments. Thank you Ed, Rob and Peter for helping me with manufacturing test specimens. Thank you Roy for the SEM training and SEM tests. Thank you Marlies for the help in performing the TMA and MDSC tests. Thank you Durga for the help in performing the density and fiber volume ratio tests. Besides, I would like to thank Sian Jones and Phil Vardon from the CITG Faculty for the help in the measurements of thermal conductivity of composite laminates.

Thanks also goes to the service desk and ICT team for all the support. Thank you Denise, Eric and Fred for the help in solving my computer-related problems.

I would like to thank my committee members for accepting to be part of my doctoral committee and for your valuable comments and feedback on my thesis.

I am glad to be part of such an interdisciplinary and international department with diversity and inclusion. Here I want to thank all the members (former and current) in the ASM department for the nice and enjoyable working environment. To my NB0.34 office mates: Camila, Silvia, Ioannis (Yannos), Nitesh, Vincent, Zhiyuan and Billy, thank you for all the support and all the nice and interesting talks and discussions. Special thanks to my former office mates in my first year in the flexible room: Aravind, Ali and Niels, thank you for the kind help when I just arrived.

To everyone (formerly or currently) working in the NDT group, Michael, Pedro, Ali, Pratik, Dmitrii, Aydin, Xiang, Vincentius, Nakash, Luigi, Sandra, Kasun, Kazi, and of course Roger and Andrei. Thank you for many nice drinks, discussions, meetings and gatherings. Special thanks go to Michael, Pedro, Pratik and Dmitrii for the kind help and support during my Go/No-Go meeting. Thank you also Michael, Pratik and Dmitrii for all the happy time during playing badminton and bowling. To the new NDT-SHM cluster, Nan Yue, Davide Biagini, Silvia, Rose, Sandra, Kasun, Denis Goto, Morteza, Dimitrios, Sergio and Vahid, thank you for all the nice presentations and discussion in the NDT-SHM colloquiums. Thank you Nan Yue for the nice discussions on ultrasonics and lamb waves. Thank you Morteza for the interesting talks on thermography and AI. Special thanks goes to Dimitrios for material feedback on Damen's GFRP panel. Special thanks go to Vahid for the nice talks and discussions on vibration analysis.

To my Chinese friends, Ran, Lubin, Xiang, Xi Li, Yuqian, Nan Yue, Jingjing, Yuzhe, Xiaodong, Hongwei, Zhiyuan, Wenjie, Shichen, Xiaopeng, Muping, Qiuyu, Qianqian, Jurui and everyone I have forgotten to mention, thank you for nice talks, discussions and parties. Special thanks go to Ran for many nice talks, lunches, discussions about my research and NDT/SHM including X-rays, I wish you the best in the future research.

To my colleagues and friends that I have met in the ASM department as well as in the aerospace engineering faculty: Agnes, Andrea Sciacchitano, Baris, Bram, Boyang, Calvin,

Curriculum Vitæ

Basic information

Name	Nan Tao
Date of birth	10 June 1994
Nationality	Chinese
ResearchGate	researchgate.net/profile/Nan-Tao
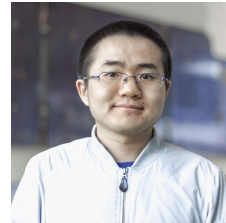
Education

Sept. 2018 - Nov. 2023	**Ph.D**, Faculty of Aerospace Engineering Delft University of Technology, Delft, the Netherlands
Sept. 2015 - Jun. 2018	**MSc**, School of Civil Engineering (Solid Mechanics) Southeast University, Nanjing, China
Sept. 2011 - Jun. 2015	**BSc**, School of Civil Engineering (Engineering Mechanics) Southeast University, Nanjing, China

LIST OF PUBLICATIONS

JOURNAL PAPERS

5. **Nan Tao**, Andrei G. Anisimov, Esther van Duijn, Lisette Vos, Ilse Steeman, Katrien Keune, Petria Noble, Roger M. Groves, *Assessment of the structural integrity of the wax-resin lined canvas paintings with 3D shape shearography*, Manuscript in preparation.

4. Pedro A. Ochôa, H.J. den Ouden, Michiel Hagenbeek, **Nan Tao**, Andrei G. Anisimov, Roger M. Groves, *Towards complete diagnosis of structural damage in a real-scale full-composite ship hull section subjected to high-energy impacts by acoustic emission monitoring and laser shearography inspection*, Under review.

3. **Nan Tao**, Andrei G. Anisimov, Roger M. Groves, *Towards safe shearography inspection of thick composites with controlled surface temperature heating*, NDT & E International **139**, 102907 (2023).

2. **Nan Tao**, Andrei G. Anisimov, Roger M. Groves, *FEM-assisted shearography with spatially modulated heating for non-destructive testing of thick composites with deep defects*, Composite Structures **297**, 115980 (2022).

1. **Nan Tao**, Andrei G. Anisimov, Roger M. Groves, *Shearography non-destructive testing of thick GFRP laminates: Numerical and experimental study on defect detection with thermal loading*, Composite Structures **282**, 115008 (2022).

CONFERENCE PAPERS

3. **Nan Tao**, Andrei G. Anisimov, Esther van Duijn, Lisette Vos, Ilse Steeman, Katrien Keune, Petria Noble, Roger M. Groves, *Application of shearography with thermal loading for the structural inspection of Rembrandt's Night Watch*, in Optics for Arts, Architecture, and Archaeology (O3A) IX, International Society for Optics and Photonics (SPIE, 2023).

2. **Nan Tao**, Andrei G. Anisimov, Roger M. Groves, *Shearography non-destructive testing of a composite ship hull section subjected to multiple impacts*, in Proceedings of the 20th European Conference on Composite Materials: Composites Meet Sustainability (ECCM20, 2022).

1. **Nan Tao**, Andrei G. Anisimov, Roger M. Groves, *Spatially modulated thermal excitations for shearography non-destructive inspection of thick composites*, International Society for Optics and Photonics (SPIE, 2021).